

UNIVERSITA' DELLA CALABRIA

Dipartimento di Fisica

**Dottorato di Ricerca in
Scienze e Tecnologie Fisiche, Chimiche e dei Materiali**

**CICLO
XXIX**

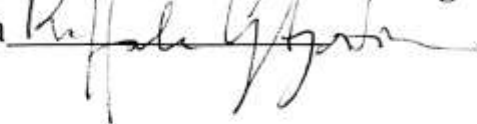
**CONTROL SYSTEM FOR THE IMPROVEMENT OF CMOS-
TECHNOLOGY FOR X-RAY CONTRAST PHASE IMAGING**

**Settore Scientifico Disciplinare:
Facilities e strumentazione innovativa**

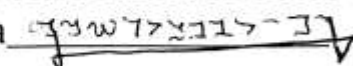
Coordinatore: Ch.mo Prof. Vincenzo Carbone

Firma 

Supervisore/Tutor: Ch.mo Prof. Raffaele Agostino

Firma 

Dottorando: Dott. Francisco Brito del Pino

Firma 

A. 2018

Sommario

Il presente lavoro di tesi descrive i risultati del progetto di ricerca sviluppato presso il Laboratorio μ Tomo della sorgente di luce STAR, parte della Progetto PON Materia presso l'Università della Calabria e presso altre facilities internazionali di luce di sincrotrone.

Il progetto ha riguardato lo sviluppo degli strumenti di acquisizione e trattamento dati e in particolare la realizzazione di un pacchetto software completo in linguaggio LabView per il controllo remoto del sistema di microtomografia μ Tomo. La programmazione è consistita nel controllo dell'insieme stazione sperimentale ovvero dei cinque motori passo-passo e del rilevatore a *flat panel* necessari per l'allineamento del campione e l'acquisizione delle immagini. La prima indagine tomografica eseguita dalla *beamline* μ Tomo è quindi riportata e discussa.

Inoltre, il pacchetto software è stato evoluto per essere integrato nel sistema di controllo di STAR cioè per espletare la funzione di server EPICS e consentire il controllo remoto su piattaforma EPICS allo stesso livello di controllo della sorgente dell'intera sorgente STAR. Sono quindi state eseguite una serie di test di funzionamento della stazione sperimentale che hanno portato a risultati nel campo della scienza dei materiali ed in particolare in quella dei dispositivi a semiconduttore.

Come parte del progetto di ricerca, nel quadro di una collaborazione scientifica con il gruppo di lavoro della linea di luce ID17 dedicata all'*imaging* biomedico, la biologia e la radioterapia, del Sincrotrone ESRF di Grenoble (F), è stata sviluppata una interfaccia utente grafica per rendere disponibile la tecnica di *imaging* a contrasto di fase in modalità di propagazione – PBI. Il software sviluppato è stato testato effettuando due esperimenti micro-tomografia a raggi X.

Al fine di una migliore esposizione, questo lavoro di tesi è stato diviso in quattro parti:

Capitolo I: Fondamenti teorici, descrizione dei fondamentali sulla microtomografia a raggi X.

Capitolo II: Implementazione hardware, descrizione dettagliata del sistema di acquisizione.

Capitolo III: Sviluppo e sperimentazione del pacchetto software di controllo della stazione ed acquisizione dati

Capitolo IV: Risultati e discussione su esperimenti effettuati per verificare le prestazioni dei sistemi di micro-tomografia.

Abstract

The present dissertation is intended describing the results of the research project developed at the μ Tomo Laboratory of the STAR light source, as part of the PON MaTeRiA Project at the University of Calabria.

The project involved making the data acquisition and treatment tools by developing a complete software package in LabView language for remote control of the μ Tomo microtomography system. The programming consisted of control of the whole experimental station including five stepper motors and a flat panel detector necessary for the sample alignment and image acquisition. The first tomographic investigation performed by the μ Tomo beamline are reported and discussed.

Furthermore, the software was evolved to be integrated into the STAR control system i.e. to run as an EPICS server in LabView language and permit the remote control on a EPICS platform at the same control level as the STAR source.

As part of the research project, in the framework of a scientific collaboration with the ID17 beamline dedicated to biomedical imaging, radiation biology and radiation therapy, of the ESRF Synchrotron in Grenoble (F), a Graphic User Interface was developed for the implementation of the Propagation-based phase-contrast imaging technique, the software was tested by carrying out two micro-CT experiments.

For the sake of a clear description this dissertation was divided into four parts:

Chapter I: Theoretical foundation, description of fundamentals on X-ray microtomography.

Chapter II: Hardware Implementation, detailed description of acquisition system.

Chapter III: Development and testing of Data Acquisition Software

Chapter IV: Results and Discussion on benchmark experiments carried out to verify the micro-tomography systems performance.

DEDICATION

I dedicate this work to my parents Fernando and Cecilia.

INDEX

| | |
|---|----|
| 1. Theoretical Foundation | 15 |
| 1.1. Evolution of X-ray Microtomography..... | 15 |
| 1.2. Introduction to Microtomography | 16 |
| 1.3. Phase Contrast in Microtomography | 21 |
| 1.4. The noise in microtomography..... | 23 |
| 1.5. The artefacts in microtomography..... | 24 |
| 1.6. Cone Beam in microtomography..... | 26 |
| 1.7. Physical factors which affect the performance of CBCT | 26 |
| 1.8. Reconstruction in microtomography | 28 |
| 2. Hardware System | 34 |
| 2.1. Microtomography System | 34 |
| 2.2. Acquisition in Microtomography | 36 |
| 2.3. Syrmep Beamline - Elettra Sincrotrone Trieste..... | 36 |
| 2.4. ID17 – Beamline - ESRF Grenoble..... | 39 |
| 2.5. STAR Facility..... | 39 |
| 2.6. μ Tomo Laboratory at STAR | 40 |
| 2.7. Hardware Beamline Syrmep for acquisition | 46 |
| 3. Software Development | 49 |
| 3.1. The Main Program..... | 49 |
| 3.1.1. Control Motors | 50 |
| 3.1.2. TCP/IP Acquisition..... | 55 |
| 3.1.3. Subprograms Link..... | 57 |
| 3.2. Upgraded to EPICS I/O Server..... | 58 |
| 3.3. Alternative Software for image acquisition – SYRMEP beamline @ Elettra..... | 60 |
| 3.4. Development of Graphic User Interface (GUI) in Python Language – ID17 beamline @ ESRF..... | 61 |
| 3.5. Flowchart..... | 65 |

| | |
|--|-----|
| 4. Results and Discussion | 67 |
| 4.1. Experiment 1: Non-destructive Measurements of Single Events Induced on Power MOSFETs by Terrestrial Neutrons..... | 67 |
| 4.1.1. Introduction..... | 67 |
| 4.1.2. Materials and methods | 68 |
| 4.1.3. Discussion | 102 |
| 4.2. Additional Experiments..... | 104 |
| 4.2.1. Experiment 2: μ -CT Phase contrast and phase retrieval on organic matter..... | 104 |
| 4.2.2. Experiment 3: μ -CT Contrast analysis using a phantom | 110 |
| 4.2.3. Experiment 4: μ -CT on a plasticized rat | 118 |
| 4.2.3.1. Introduction..... | 118 |
| 4.2.3.2. Results: 3D Rendering and Segmentation | 120 |
| 5. Conclusions | 124 |
| 6. Annexes | 126 |
| 6.1. Annex 1..... | 126 |
| 6.2. Annex 2..... | 127 |
| 7. References | 131 |

List of Figures

| | |
|---|----|
| Figure 1: Microtomography - Timeline | 15 |
| Figure 2: Projection and scanning of the object in plane (t, s)..... | 18 |
| Figure 3: Scanning of a single layer in the plane (x, y) | 18 |
| Figure 4: Attenuation mechanism | 19 |
| Figure 5: Lambert–Beer Law in homogeneous object | 19 |
| Figure 6: Lambert–Beer Law in non-homogeneous object..... | 20 |
| Figure 7: Projection of sphere phantom in phase-contrast imaging..... | 22 |
| Figure 8: Typical Poisson noise | 23 |
| Figure 9: The artefacts in of sinogram. | 24 |
| Figure 10: Central slice of a perfect phantom. | 25 |
| Figure 11: Cone beam CT geometry. | 26 |
| Figure 12: Cone beam - microtomography system | 27 |
| Figure 13: Cone beam magnification | 27 |
| Figure 14: Projection of a slice under parallel object beams | 29 |
| Figure 15: Generation of a sinogram..... | 29 |
| Figure 16: Propagation through of object with different levels of intensity | 30 |
| Figure 17: Basic back-projected and reconstructed volume | 30 |
| Figure 18: Typical cone beam micro-CT machine..... | 34 |
| Figure 19: Difference between microfocus-CT systems and synchrotron system..... | 35 |
| Figure 20: Position of detector respect of magnification ratio..... | 36 |
| Figure 21: Schematic illustration of X-ray CT acquisition and reconstruction processes. | 36 |
| Figure 22: Syrmep Beamline | 38 |
| Figure 23: ID 17- Schematic description of the imaging setup..... | 39 |
| Figure 24: STAR Facility | 40 |
| Figure 25: Reference of motors..... | 41 |
| Figure 26: Experimental Station - μ Tomo | 44 |
| Figure 27: Connection diagram..... | 45 |
| Figure 28: Alignment of experimental station | 46 |

| | |
|--|----|
| Figure 29: EPICS - Connection Diagram..... | 46 |
| Figure 30: SYRMEP setup for acquisition..... | 47 |
| Figure 31: Front Panel..... | 50 |
| Figure 32: Block Diagram..... | 50 |
| Figure 33: Absolute movement - Axis 1 | 51 |
| Figure 34: Absolute movement - Axis 3..... | 51 |
| Figure 35: Relative movement | 52 |
| Figure 36: Control rotation, x and y movements | 53 |
| Figure 37: Hydra – View file | 54 |
| Figure 38: Absolute movement for rotator..... | 55 |
| Figure 39: Front Panel - TCP/IP Acquisition..... | 56 |
| Figure 40: File Parameters | 56 |
| Figure 41: Block diagram – Acquisition..... | 57 |
| Figure 42: Block diagram. Link between Subprograms and Main Program | 57 |
| Figure 43: Front Panel – Epics Server | 58 |
| Figure 44: Part of block diagram – Epics Server | 59 |
| Figure 45: Epics Server – LabVIEW Project..... | 59 |
| Figure 46: Monitoring Epics Process Variables with Distributed System Manager..... | 60 |
| Figure 47: Alternative Software for acquisition image..... | 61 |
| Figure 48: Template of Basic Parameters | 62 |
| Figure 49: Template of Expert Parameters | 62 |
| Figure 50: Template of Range Parameters..... | 63 |
| Figure 51: a) Model for SEB (92); b) and for SEGR (93). | 68 |
| Figure 52: Detail of neutron irradiate Power MOSFET..... | 69 |
| Figure 53: SEM single device – Power MOSFET..... | 70 |
| Figure 54: SEM of metal heatsink..... | 71 |
| Figure 55: SEM of Si substrate | 71 |
| Figure 56: SEM of external package..... | 71 |
| Figure 57: Overall schematic representation of the SEM analysis | 72 |

| | |
|--|----|
| Figure 58: 3D Power MOSFET result of horizontal position | 74 |
| Figure 59: Vertical scan – Power MOSFET | 75 |
| Figure 60: Orthogonal cut of the reconstructed MOSFET 3D image by means of a “Vertical scan” | 75 |
| Figure 61: MDmesh Power MOSFET Structure..... | 77 |
| Figure 62: Power MOSFET volume rendering | 78 |
| Figure 63: Histogram of the voids area in the Pb layer for the sample MOSFET #1. | 78 |
| Figure 64: Zoom - Orthogonal View..... | 79 |
| Figure 65: Zoom - Orthogonal View and 3D of ROI of interest..... | 80 |
| Figure 66: MOSFET #3 - XZ plane cut along the Pb layer | 80 |
| Figure 67: Zoom on the ROI (Orthogonal View) | 81 |
| Figure 68: ROI Rendering 3D – Side view | 81 |
| Figure 69: 2D Projection | 82 |
| Figure 70: 2D Projection | 82 |
| Figure 71: 2D Projection | 82 |
| Figure 72: Side View and zoom view to 150%..... | 83 |
| Figure 73: 2D Projection | 84 |
| Figure 74: ROI Rendering 3D – Top view | 84 |
| Figure 75: 3D - Side View and 300% 3D Zoom..... | 85 |
| Figure 76: 2D Projection | 86 |
| Figure 77: Zoom XZ view..... | 86 |
| Figure 78: 3D – Side -view | 87 |
| Figure 79: 3D - Side view and 1200% zoom view. | 87 |
| Figure 80: 2D μ CT cut of MOSFET #1 after n-irradiation..... | 88 |
| Figure 81: ROI Rendering 3D – Top view..... | 89 |
| Figure 82: 3D Rendering: (a) side view | 90 |
| Figure 83: 2D μ CT cut of MOSFET #2 after n-irradiation..... | 91 |
| Figure 84: Orthogonal View and located of damage single device MOSFET #2..... | 91 |
| Figure 85: (a) ROI Rendering 3D – Top view; (b) Perspective view | 92 |
| Figure 86: ROI Rendering 3D – Side view | 92 |

| | |
|---|-----|
| Figure 87: 2D μ CT cut of MOSFET #3 after n-irradiation..... | 93 |
| Figure 88: 3D Single Device ROI – Top view and Side view | 93 |
| Figure 89: 2D μ CT cut of MOSFET #4 after n-irradiation..... | 94 |
| Figure 90: Orthogonal View across the ROI where the defects is located in MOSFET#4 .. | 94 |
| Figure 91: MOSFET #4 - 3D Rendering of the ROI: | 95 |
| Figure 92: 2D μ CT cut of MOSFET #5 after n-irradiation..... | 95 |
| Figure 93: n-irradiated MOSFET #5 - Zoom XZ view of the ROI..... | 96 |
| Figure 94: n-irradiated MOSFET #5 - 3D..... | 96 |
| Figure 95: Orthogonal cuts of the 3D μ CT reconstruction.. .. | 97 |
| Figure 96: Zoom on the ROI- Orthogonal View and 3D of the Pb tab..... | 98 |
| Figure 97: ROI 3D Rendering– Side view. Length 1: 83 μ m - length 2: 62 μ m. | 98 |
| Figure 98: 2D μ CT cut of MOSFET #7 after n-irradiation..... | 99 |
| Figure 99: n-irradiated MOSFET #7 Zoom on the ROI - Orthogonal View and 3D..... | 99 |
| Figure 100: ROI Rendering 3D – Side view. Length 1: 54 μ m – length 2: 135 μ m..... | 100 |
| Figure 101: Typical reconstructed volume slab of the Power MOSFET | 100 |
| Figure 102: Cross section for $^{28}\text{Si}(n,p) ^{28}\text{Al}$ reaction (left) and for $^{28}\text{Si}(n, \alpha) ^{25}\text{Mg}$ reaction (right - from ENDF/B-VII.1 database)..... | 103 |
| Figure 103: Setup of onion specimen..... | 105 |
| Figure 104: Cropping normalized projection | 106 |
| Figure 105: Sinogram of the Onion Bulb, Projection 91. Left: Sinogram. Right: Profile | 106 |
| Figure 106: Slice 91 reconstruction without phase retrieval..... | 107 |
| Figure 107: Slice 91 reconstruction with phase retrieval | 108 |
| Figure 108: Comparison of the central part of slice 91 reconstructed images. | 108 |
| Figure 109: 3D Rendering - Filaments..... | 109 |
| Figure 110: Phantom placed on the Computed Tomographic stage during the acquisition. . | 111 |
| Figure 111: Slice 1000 reconstructed..... | 113 |
| Figure 112: CNR values for phantom materials (above).. .. | 116 |
| Figure 113: Plot of CTF | 117 |
| Figure 114: Plastirat sample on the Computed Tomographic stage..... | 119 |
| Figure 115: Detector couple with the 1:3.6 optic..... | 120 |

| | |
|--|-----|
| Figure 116: Segmentation images | 121 |
| Figure 117: 3D - Transversal view..... | 122 |
| Figure 118: Brain - Top View | 122 |
| Figure 119: Brain - Side View | 123 |
| Figure 120: Brain - Bottom View | 123 |

Acronyms and Abbreviations

| | |
|-------------|---|
| μ Tomo | Micro-Tomography |
| CBCT | Cone beam computed tomography |
| CNR | Contrast to noise ratio |
| COR | Center of rotation |
| CT | Computed Tomography |
| EPICS | Experimental Physics and Industrial Control System |
| ESRF | European Synchrotron Radiation Facility |
| FOD | Focus Object Distance |
| FOV | Field of view |
| GUI | Graphic Interface User |
| LabVIEW | Laboratory Virtual Instrument Engineering Workbench |
| MaTeRiA | Materiali, Tecnologie e Ricerca Avanzata |
| MOSFET | Metal-oxide-semiconductor field-effect transistor |
| micro-CT | micro Computed Tomography |
| NIST | National Institute of Standards and Technology |
| PBI | Propagation-based phase-contrast imaging |
| PON | National Operational Program |
| ROI | Region of interest |
| SDD | Source to detector distance |
| SEEs | Single Events |
| SEB | Single Event Burnout |
| SEGR | Single Event Gate Rupture |
| SOD | Source to object distance |
| SR μ CT | Synchrotron radiation micro-computed tomography |
| STAR | South Europe Thomson source for Applied Research |
| STP | SYRMEP Tomo Project |
| SYRMEP | Synchrotron Radiation for MEDical Physics |
| TCP/IP | Transmission Control Protocol/Internet Protocol |

Chapter I

Theoretical Foundation

1. Theoretical Foundation

1.1. Evolution of X-ray Microtomography

The theoretical basis of microtomography has its origins in the year 1917, only few years after that Roentgen discovered X-ray in 1895, when the Austrian mathematician Johan Radon proved that an n-dimensional object can be reconstructed from its n-1 dimensional projections. However, only in the second half of the past century, the mathematical basis for the actual CT image reconstruction was presented in two scientific articles by Allan M. Cormack (See Figure 1).

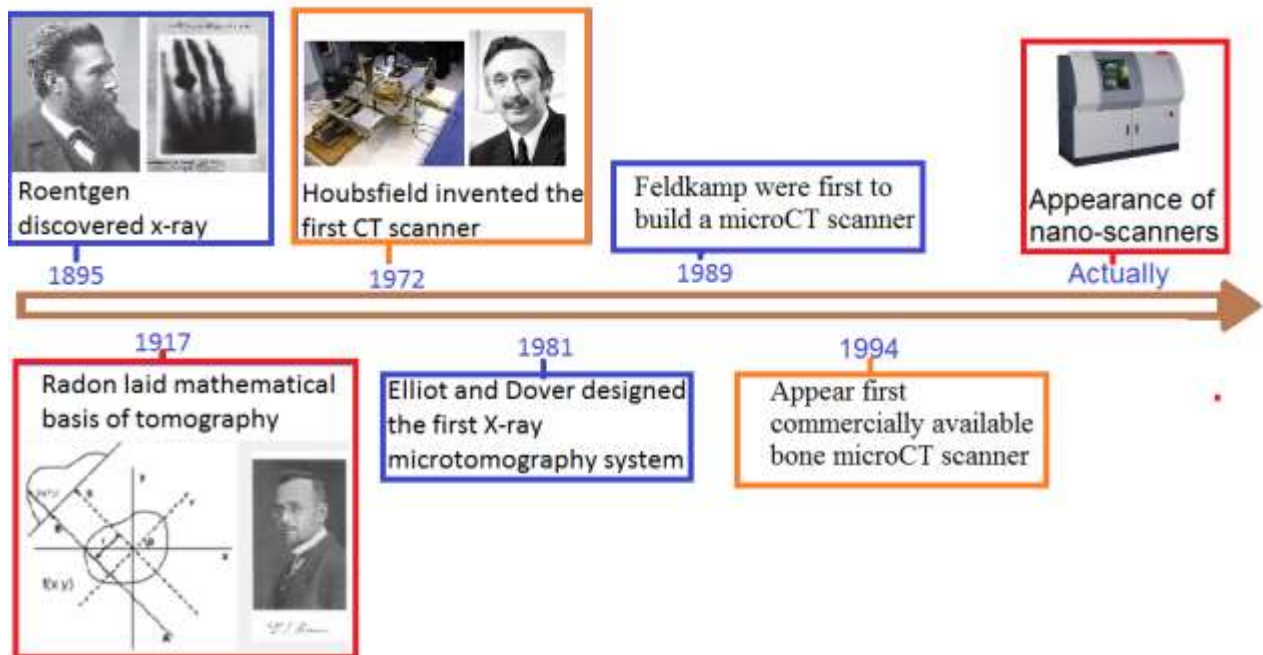


Figure 1: Microtomography - Timeline

The development of microtomography laboratories emerged in the mid-1960s, creating images by exploiting the X-ray refraction in addition to their absorption. (1)

Nowadays, the X-ray microtomography or micro-computed tomography (micro-CT) is a technique of radiographic imaging able to produce 3D images of the inner structure of a material with a spatial resolution in the order of the micrometers (2).

The first microtomography system was produced by Jim Elliott in the early 1980s. The first microtomographic images were slices of a small snail, with an effective pixel size of

approximately 50 micrometers (3).

The first conical scanner was constructed by Feldkamp for the reconstruction of the three-dimensional microstructure of trabecular bone (4).

In 1992, by using the high quality of the radiation emitted by the third-generation synchrotron a resolution of 1- μm was achieved (5). In 1994, with the first commercially available micro-CT scanner, the microtomography technique started to become a standard in bone research. Currently, in-vivo and in-vitro micro-CT scanners are available from several manufacturers (6). The phase contrast imaging, a new technique based on the interfering paths of coherent X-ray beams, will surely continue to expand the applications for micro-CT in small animal models (7).

Laboratory-based micro-CT and nano-CT scanners as well as integrated micro-CT/SPECT and micro-CT/PET scanners are marketed nowadays (8).

1.2. Introduction to Microtomography

Microtomography is a non-destructive technique tool that obtains tri-dimensional images exploiting a set of bi-dimensional images from a sample (9).

The principle of micro-CT is based on the attenuation of X-rays passing through the object or sample being imaged. As an X-ray passes through a homogeneous medium, the intensity of the incident X-ray beam is reduced according to the Lambert-Beer equation, $I_x = I_0 e^{-\mu x}$, where I_0 is the intensity of the incident beam, x is the distance covered by the X-ray in the absorbing medium, I_x is the intensity of the beam in the position x from the surface, and μ is the linear attenuation coefficient (10).

Moving to a more detailed description, the X-ray as an electromagnetic wave is characterized by amplitude, polarization, frequency, wave-vector and phase. As a result of the interaction of the electro-magnetic wave with a given medium, its amplitude attenuated, and its phase shifted. The refraction index of any material can be expressed by a complex number (11) (12):

$$n = 1 - \delta + j\beta \quad \text{Eq. 1}$$

The symbol δ is the refractive index, which determines the phase shift and β absorption index of x-ray wave and is expressed by (13):

$$\delta = \frac{\lambda}{2\pi} \sum_k N_k \phi_k \quad \text{Eq. 2}$$

$$\beta = \frac{\lambda}{4\pi} \sum_k N_k \mu_k \quad \text{Eq. 3}$$

where, for each element k,

ϕ_k : phase shift cross-section.

μ_k : atomic absorption cross-section.

N_k : atomic density.

The form of the X-ray wave through a uniform medium is (11) - (12):

$$\psi(\vec{r}) = A \cdot \exp(jn\vec{k} \cdot \vec{r}) = A \cdot \exp(-\beta(\vec{k} \cdot \vec{r})) \cdot \exp(j\vec{k} \cdot \vec{r}) \cdot \exp(-\delta(j\vec{k} \cdot \vec{r})) \quad \text{Eq. 4}$$

With:

A: initial amplitude

\vec{k} : wave vector

\vec{r} : the position vector

From Eq. 4, β contributes to the attenuation of amplitude and δ to the wave phase shift. Theoretically and experimentally it had been demonstrated that, in the X-ray range, δ is thousands of times larger than β .

Projections acquisition.

In referring to the projection and scanning of an object, as depicted in Figure 2, we consider the rotation about the z-axis in a rotational coordinate system {s, t, z}. The intensity of the

transmitted beam is recorded as a translation function of the position parameter t for each z value. Lambert's Law gives the transmitted intensity by the following expression: (14)

$$I(x, y) = I_o \exp \left(- \int_{path} \mu(x, y) ds \right) \quad \text{Eq. 5}$$

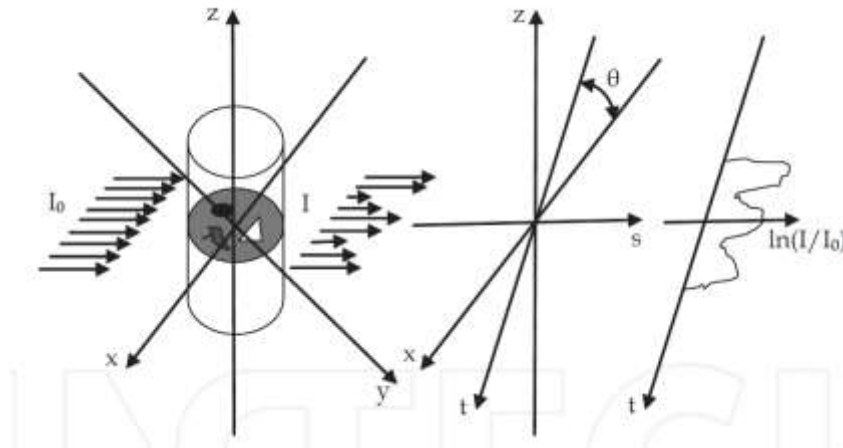


Figure 2: Projection and scanning of the object in plane (t, s)

Figure 3 indicates the scanning of a single layer in the plane (x, y). Such a projection can be defined by: (14)

$$P_{\theta}(t) = \ln \left(\frac{I}{I_0} \right) = \int_{path} \mu(x, y) ds \quad \text{Eq. 6}$$

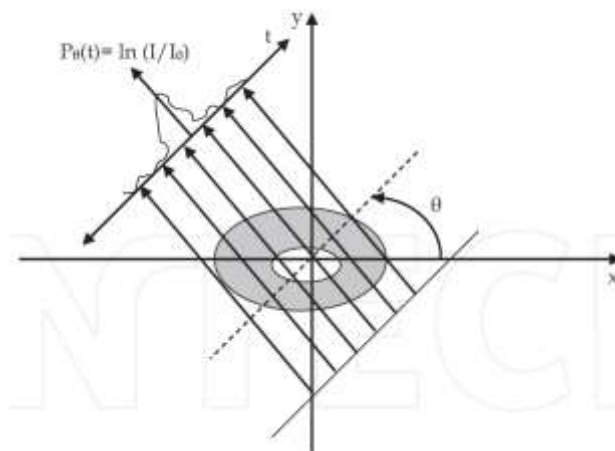


Figure 3: Scanning of a single layer in the plane (x, y)

The attenuation is determined by the sample composition and by the spectral distribution of the X-radiation and can be used to quantify the density of the imaged object. Generally, to obtain such information, the reduced intensity beams are collected by a flat-panel detector (See Figure 4) (9) (15).

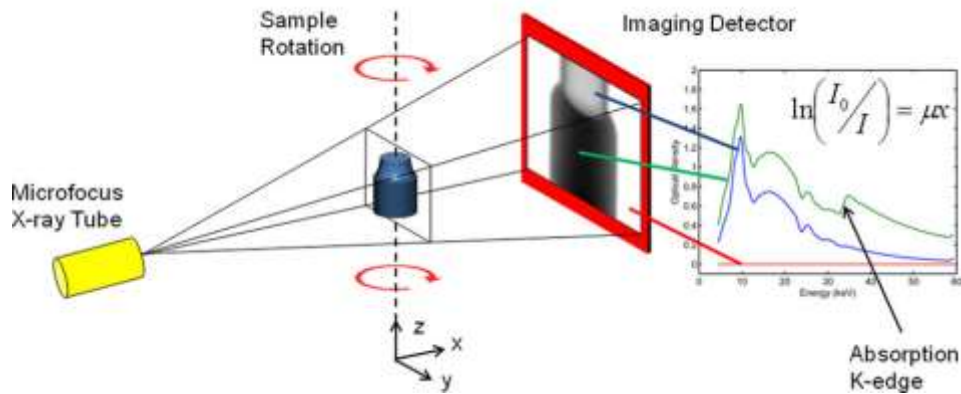


Figure 4: Attenuation mechanism

As an example, if we consider a monochromatic ray penetrating through a homogeneous object, the ray attenuation can be explained by the Lambert–Beer Law and depends only on the object thickness x for each point of the projection (see Figure 5) (16) (17) (18).

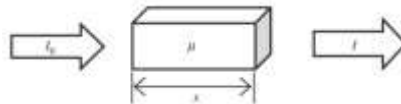


Figure 5: Lambert–Beer Law in homogeneous object

Figure 6 illustrates two projections acquired for an elliptical test object immersed in a medium with different absorption coefficient (non-homogeneous material). The intensity curve will be related to the geometrical shape of the test object. By following its evolution on the projection angle, it will be possible to reconstruct the whole object shape.

On the right of Figure 6, we find a schematic representation of a more complex situation where two projections acquired from an object consisting of a 2×2 matrix of different materials. The intensities of the projections can be expressed in terms of the linear attenuation coefficients by:

(19)

$$I_1 = I_0 e^{-(\mu_1 + \mu_2)x} \quad \text{Eq. 7}$$

$$I_2 = I_0 e^{-(\mu_3 + \mu_4)x} \quad \text{Eq. 8}$$

$$I_3 = I_0 e^{-(\mu_1 + \mu_3)x} \quad \text{Eq. 9}$$

$$I_4 = I_0 e^{-(\mu_2 + \mu_4)x} \quad \text{Eq. 10}$$

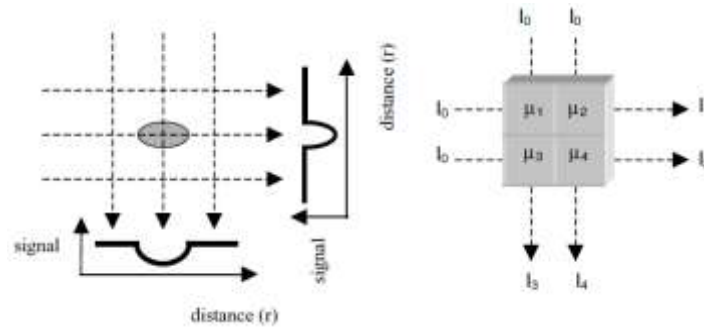


Figure 6: Lambert-Beer Law in non-homogeneous object

As already noted, the mathematical bases for the tomographic images were formulated by Johann Radon. Even though it is applied in computed tomography to obtain cross-sectional images of patients, tomographic reconstruction applies for all types of tomography. Some terms or physical descriptions we will use refer directly to computerized axial tomography.

We already showed how the projections of an object at a certain angle θ they are made up of a series of line integrals. In X-ray computed axial tomography, the line integrals represent the total attenuation of the X-ray beam while they travel in a straight line through the object and the resulting image is a 2D (or 3D) model of the absorption coefficient i.e. the image $\mu(x,y)$. The simplest and easiest way to visualize the method of analysis is the system of parallel projections. For this we consider the information that is collected as a series of parallel rays in the position r , through a projection in the angle θ . This is repeated for several angles. As the attenuation occurs exponentially in the medium the total attenuation p of lightning in position r with a projection on the angle θ , is given by the following integral:

$$p(r, \theta) = \ln(I/I_0) = - \int \mu(x, y) ds \quad \text{Eq. 11}$$

Using the coordinate system of the figure, the value of r , on the point (x, y) , will be projected in the angle θ shown by the following equation: $x \cos\theta + y \sin\theta = r$. With this, we see that the equation shown above can be rewritten as follows:

$$p(r, \theta) = \int_{-\infty}^{\infty} \int_{-\infty}^{\infty} f(x, y) \delta(x \cos \theta + y \sin \theta - r) dx dy$$

Eq. 12

where $f(x, y)$ represents $\mu(x, y)$. This function is known as the Radon transform (or *sinogram*) of the object in 2D resolution. The Fourier section theorem tells us that if we have an infinite number of one-dimensional projections of an object obtained from an infinite number of angles, we can perfectly reconstruct the original object, $f(x, y)$. So, to obtain again $f(x, y)$ from the previous equation we must find the inverse Radon transform. However, the inverse Radon transform has proved to be very unstable with respect to noisy data. In practice, a stabilized and discrete version of the Radon inverse transform is used, which is commonly known as the filtered back-projection algorithm.

Knowing the Radon transform of an object allows it to reconstruct its structure: the projection theorem actually ensures that if we have an infinite number of mono-dimensional projections of an object made from an infinite number of different angles and the reconstruction process is precise when calculating Radon's anti-transformation.

However, Radon's anti-transformation is very unstable if measured data are affected by experimental noise. In practice, a stabilized and discrete version of Radon's anti-transformation, called '*filtered retroprojection algorithm*', is used. A corollary to the projection theorem states that "*Radon's transformation of the two-dimensional convolution of two functions is equal to the one-dimensional convolution of their Radon transformations*". The practical consequence of this is that in order to eliminate the noise that reduces the quality of the reconstruction, it is not necessary to physically eliminate it at source, but it is possible to filter mathematically the experimental results (i.e. the measure of the Radon transform) and then rebuild (i.e. calculate the anti-transform) directly from the *a posteriori* filtered data.

1.3. Phase Contrast in Microtomography

Conventionally computed tomography uses the absorption contrast which does not permit some details to be resolved in samples with a weak absorption contrast. In these cases, phase shift of the X-ray beam induced by the variation of the refractive index can be exploited for obtaining

a better image (20). A significant improvement over conventional attenuation-based X-ray imaging, which lacks contrast in small objects and soft biological tissues, is then obtained by introducing phase-contrast imaging (21).

The in-line phase-contrast X-ray imaging method, sometimes also called the propagation-based imaging or the inline holography, exploits the Fresnel diffraction and dubbed phase-contrast imaging method in microtomography is possible using the third generation of synchrotron radiation sources or micro-focussed X-ray tube (20) (22).

Thus, as absorption-contrast X-ray imaging serves to visualize the variation in X-ray attenuation within the volume of a given sample, the phase contrast allows us to visualize variations in the X-ray refractive index of the probed volumes (23).

Figure 7 shows the principle of in-line phase-contrast imaging: the projected images of the spheres phantom are shown for different positions of the detector along the z-axis. If $z = 0$ we have only absorption contrast. The phase contrast occurs in the Fresnel diffraction region, it means that it is necessary to place the detector at a distance from the object where $z=d^2/\lambda$ with d the object typical dimension and λ the X-ray wavelength (20).

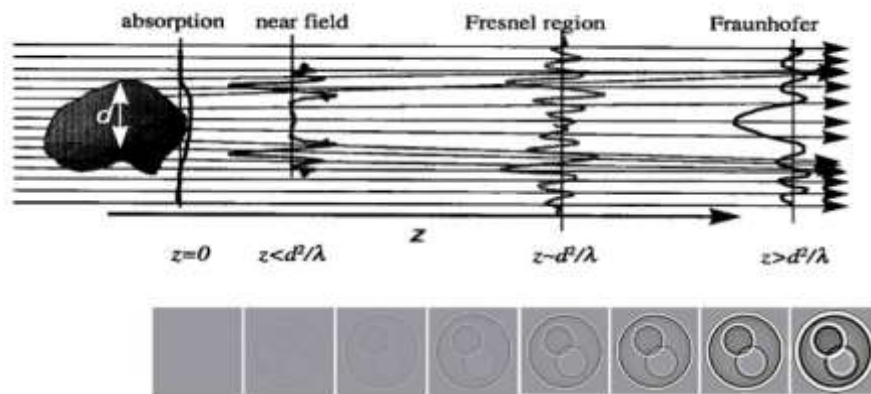


Figure 7: Projection of sphere phantom in phase-contrast imaging

The image is edge-enhanced, and for soft tissues, it is possible to retrieve the phase projection from a single in-line image. The phase contrast technique is used for reconstructing the phase coefficient using the retrieved phase projections (24).

In the propagation-based phase contrast X-ray imaging, the contrast effect increases linearly with the sample to detector distance and are given by the equation (25):

$$I(x, y) = 1 - \frac{\lambda z}{2\pi} \nabla \phi(x, y) \quad \text{Eq. 13}$$

With,

$\phi(x, y)$: phase change due to a small slab of material

λ : wavelength

z : distance from the sample to the detector

1.4. The noise in microtomography

Poisson noise is due to the statistical error of low photon counts, and results in random thin bright and dark streaks that appear preferentially in the direction of greatest attenuation. As the noise increases, high contrast objects such as bone may still be visible, but low contrast soft tissue boundaries may be obscured. Figure 8 illustrates the effect of the increase of the beam intensity on the Poisson noise. Figure 8(A) reproduces an image obtained with a low dose (source current = 60 mA) and shows a series of streaks covering the field of view. Figure 8(B) indicates the image obtained with a higher dose (source current = 440 mA). As the intensity increases by a factor 7.3 the noise is reduced by a factor $\sqrt{7.3} = 2.7$. (28)

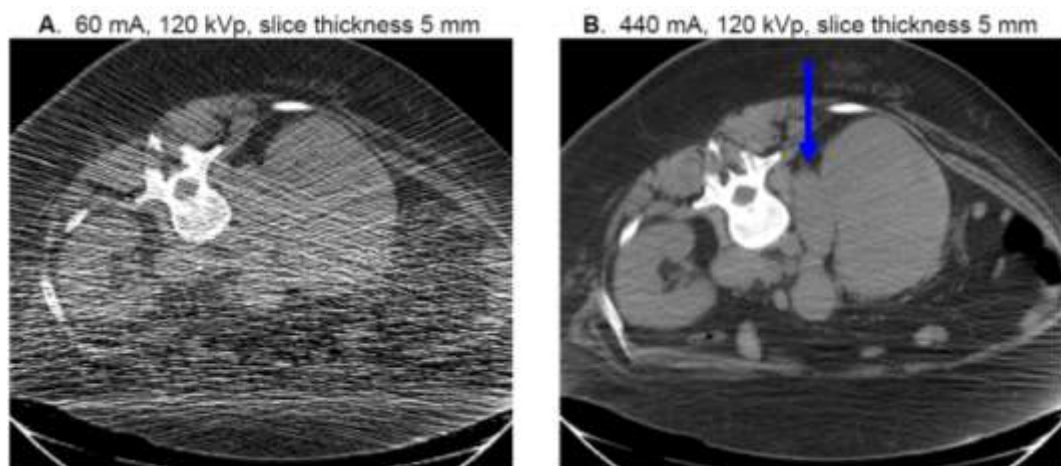


Figure 8: Typical Poisson noise

1.5. The artefacts in microtomography

The image artefact may be defined as a visualized structure in the reconstructed data that is not present in the object under investigation. Artefacts cause general inconsistencies in the reconstructions (29).

The ring artefact is caused by uncorrected variations in detector dark current, gain, linearity, and defects. Because an erroneous signal is coming from a fixed location on the detector, it produces a linear defect in the sinogram and it is reinforced in back projection at a fixed radius in the reconstruction, that is, on a circle (30). Figure 9 (a) illustrates the sinogram of a crane fly knee, taken from 400 projections over 180°. Several vertical artefacts owing to dead pixels in the CCD corrupt the sinogram. Figure 9(b) depicts the same sinogram after filtering with a one-dimensional low-pass filter. The vertical line artefacts are suppressed without significant loss of information in the sinogram. Figure 9(c) depicts the reconstructed cross-section from the sinogram. Figure 9(a) depicts strong degeneration by half-ring artefacts, and Figure 9(d) depicts how the reconstruction from the filtered sinogram improves the image quality significantly (31).

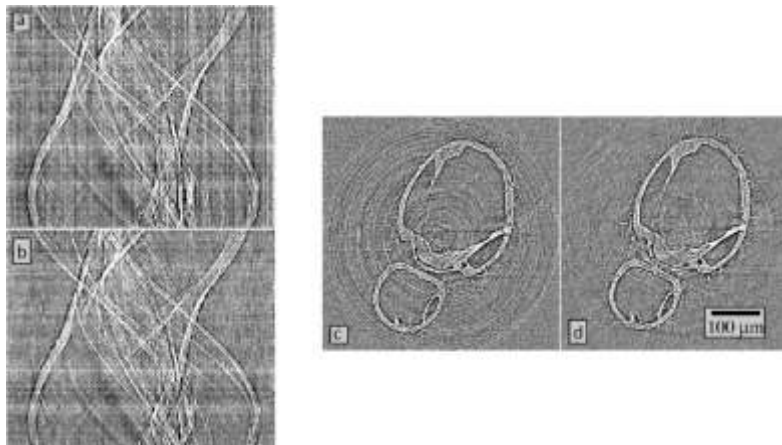


Figure 9: The artefacts in of sinogram.
(a) Without filter. (b) With filter. (c) Artefacts in the reconstructed cross-section without filter (d) with filter

Figure 10(a) illustrates a central slice of a phantom and its reconstruction with 801 projections. Figure 10(b) depicts the ring artefacts due to variation in detector element sensitivities. Streak artefacts in reconstructed CT slices can be caused by asymmetric high-density objects (like bones) when low-dose data acquisition is performed, and we cannot correctly recover the

line integral. Other possible causes are object motion or/and absorbing particles are made worse misalignment in the scanner geometry description, beam hardening and scatter effects. And finally, streaks can be the result of angular under-sampling, aggravated by missing projections (33). Figure 10(c) depicts streak artefacts due to angular under-sampling in line with straight edges with 401 projections.

If the center of rotation is incorrectly determined, a double-edged image may be seen, Figure 10(d) depicts double edges caused by a 5-pixel error in the value for the center of rotation used in the reconstruction. Meanwhile superficially similar in appearance to images with motion artefacts Figure 10(e) depicts double edges and streaking caused by specimen motion of 10-pixels.

An X-ray beam is composed of individual photons with a range of energies. As the beam passes through an object, it becomes “harder,” its mean energy increases because the lower energy photons are absorbed more rapidly than the higher-energy photons (34). Figure 10(f) depicts the beam hardening artefact caused by polychromatic radiation (34).

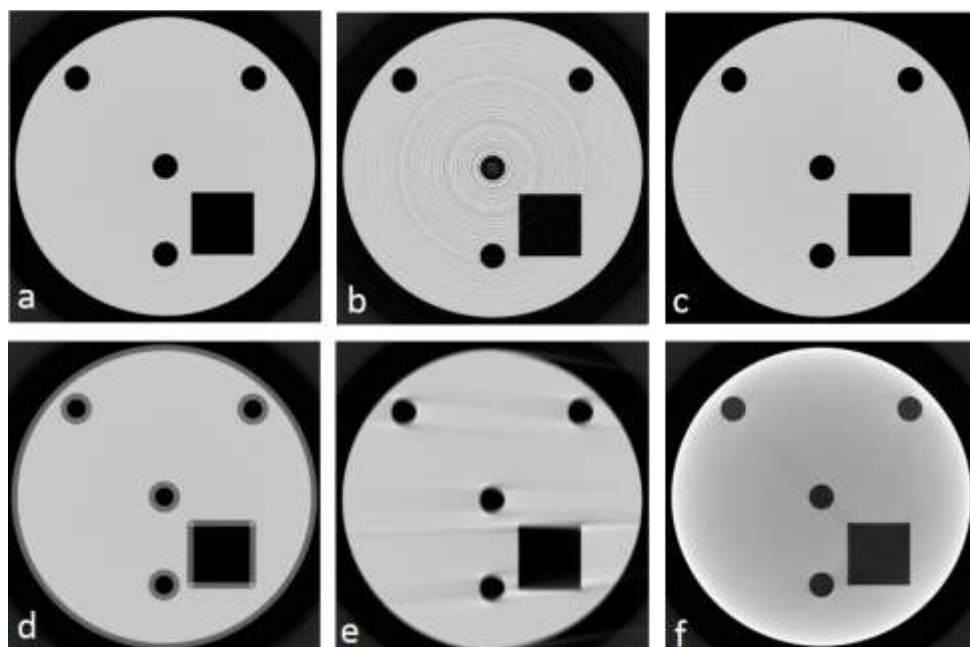


Figure 10: Central slice of a perfect phantom.

- (a) With 801 projections. (b) Artefacts owing to a detector. (c) 401 projections with streak artefacts. (d) Double edges (e) double edges and streaking. (f) Beam hardening artefact

1.6. Cone Beam in microtomography

Micro-focal CT (microtomography) in cone-beam geometry is advantageous for obtaining directly reconstructed 3D images from a set of 2D projection images recorded by the detector (35) (36).

Figure 11 illustrates the cone beam CT geometry, it is convenient to assume that the X-ray source and detector system are stationary and that the object rotates around the rotation center (37). Figure 11(a) depicts the setup for filtered image acquisition. Figure 11(b) depicts a top view of the setup. For filtered image acquisition a collimator permits focusing of the FOV (field of view) in the X-ray beam geometry. The ROI (region of interest) filter permits focusing the region of interest in the phantom (38).

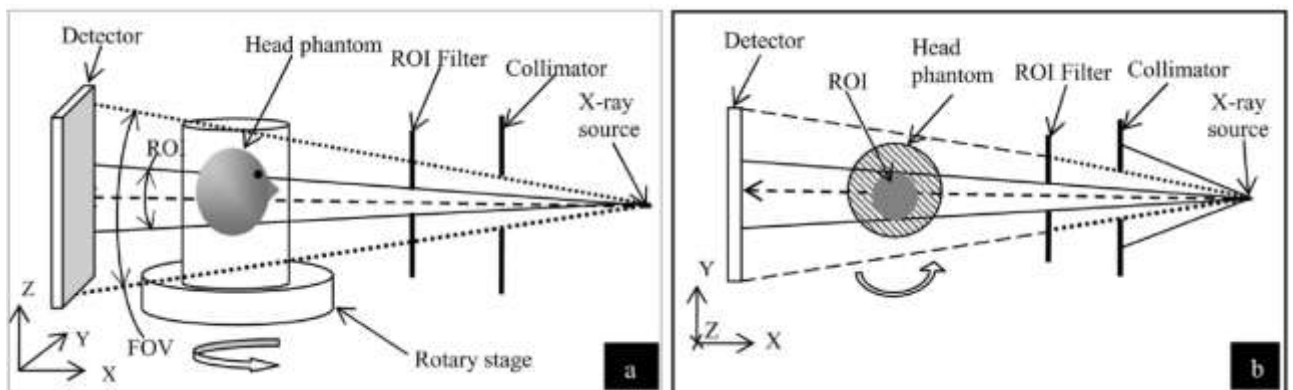


Figure 11: Cone beam CT geometry.
(a) Setup for filtered image acquisition. (b) Top view of the setup

1.7. Physical factors which affect the performance of CBCT

The main physical factors that affect the performance of CBCT (cone beam computed tomography) is system geometry which allows finding the suitable distances, such as SOD (source to object distance) and SDD (source to detector distance), for reducing the scatter artefacts but maintaining high signal-to-noise ratio (see Figure 12) (30) (39).

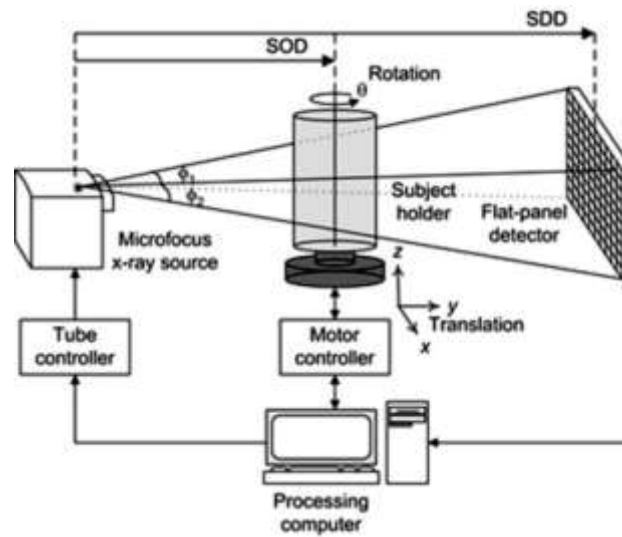


Figure 12: Cone beam - microtomography system

The focal spot size affects the spatial resolution, particularly for systems with higher magnification, a smaller the value of FOD means the object is near to the focal spot allowing the highest magnification (see Figure 13) (30) (40).

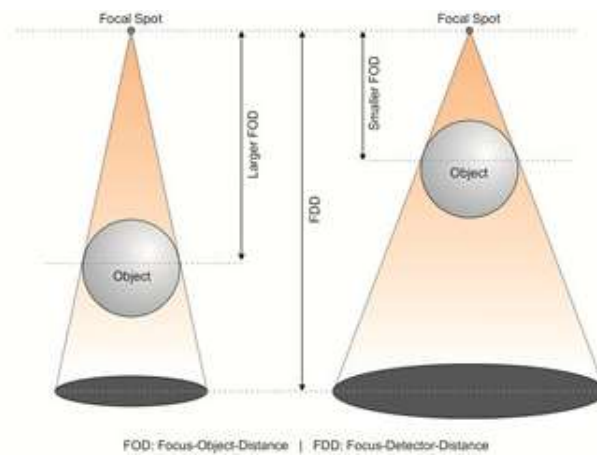


Figure 13: Cone beam magnification

The field of view (FOV) affects a loss in contrast and increases the artefacts (30). There are methods for reducing noise and artefacts that may enable ultra-high resolution limited-field-of-view imaging (28).

The dynamic range we can define simply by the ratio of the maximum and the minimum detectable signal, measured in the gray level or it can also refer to an effective number of bits

in the detector. The dynamic range of the acquisition system is the relevant quantity which determines the maximum material thickness which can be inspected (41). Maintaining fixed the FOV while the size of the object increases then noise, contrast, and artefacts increase (30).

In micro-focussed sources, the polychromatic beams produced by higher electron acceleration reduce the contrast and increases the noise. On the other hand, a softer beam with a broader spectrum increases the artefacts (30).

Microtomography reconstruction from a limited number of projections provides a method to simultaneously reduce the radiation dose and in many cases the acquisition time (42).

1.8. Reconstruction in microtomography

The reconstruction algorithms introduced in paragraph 1.2 can be implemented by using the fast Fourier transform (43).

For a good quality reconstruction, the sample must be rotated through at least 180° (plus the cone angle in CBCT). Datasets are acquired over this angular range with a certain step-size between images (44).

The reconstruction process transforms the raw acquisition data into a stack of 2D cross-sections through the sample, resulting in a 3D data set. Several artefacts and noise reduction algorithms are integrated to reduce ring artefacts, beam hardening artefacts, COR (center of rotation) misalignment, detector or stage tilt, pixel non-linearities, etc (45) .

The parameter of interest in the slice is represented by a 2D function $f(x, y)$, and each projection datum $g(u, \theta)$ is a line integral. The equations correspond to $u = x \cos \theta + y \sin \theta$ and $v = -x \sin \theta + y \cos \theta$ (see Figure 14) (46).

Figure 15 shows (a) schematic arrangement of first generation CT set-up indicating the way projections are built up from a ray-sums. In every projection, a point (P) in the object contributes to one ray-sum along the path from the source (S) to the detector (D). The axes x , and y represent the laboratory frame; x_r , y_r the rotating frame of the specimen/object. (b) The sinogram of a point P in (a) in the 2-D space (x_r, ϕ) (47).

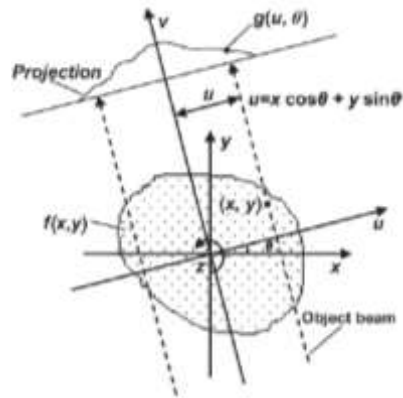


Figure 14: Projection of a slice under parallel object beams

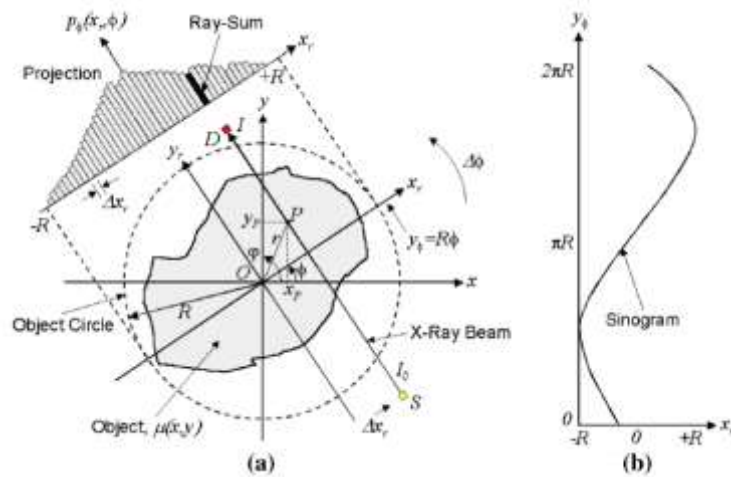


Figure 15: Generation of a sinogram

1.9 . X-ray Phase retrieval in Microtomography

Phase retrieval is a method for reconstructing phase from the measured intensity, in-line phase-contrast X-ray imaging provides images where both absorption and refraction contribute. For quantitative analysis of these images, the phase needs to be retrieved numerically (see Figure 16) (48).

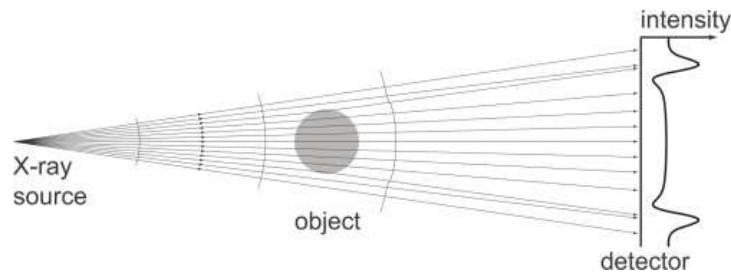


Figure 16: Propagation through of object with different levels of intensity

Figure 17 shows to the left a series of images due to X-ray transmission, the slices are acquired when the sample rotates around the vertical axis. On the right: these 2D views are mathematically back-projected through a 3D reconstruction volume (49).

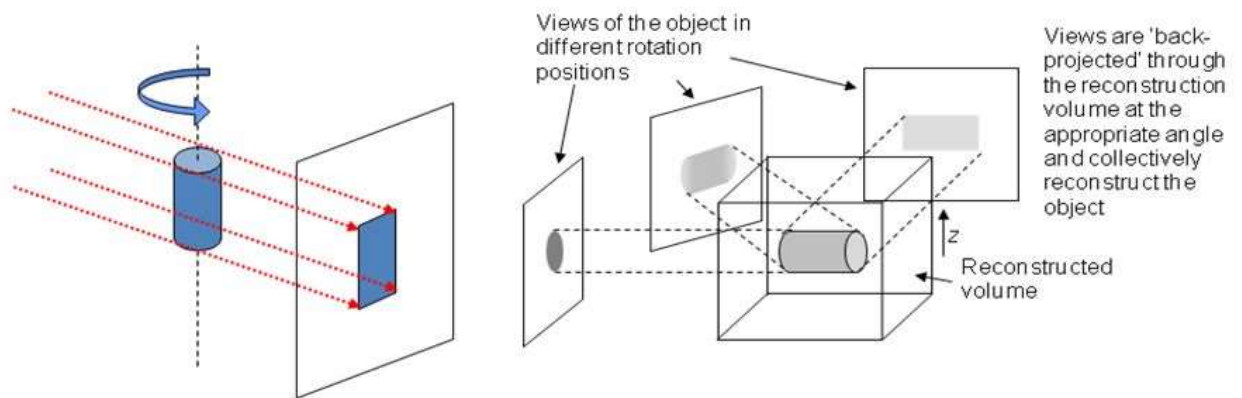


Figure 17: Basic back-projected and reconstructed volume

The phase retrieval methods in general have a general pattern of measured intensity $g(I)$ for the calculated Fourier transform $\mathcal{F}[g(I)]$, after multiplying by a filter in the domain frequency $H_p \cdot \mathcal{F}[g(I)]$, calculate the inverse Fourier transform $\mathcal{F}^{-1}\{H_p \cdot \mathcal{F}[g(I)]\}$ to obtain the filter quantity and take the function f and obtain the phase $\varphi(r_T)$ with respect to the image plane in the transverse position (48).

$$\varphi(r_T) = f(\mathcal{F}^{-1}\{H_p \cdot \mathcal{F}[g(I)]\})$$

Eq. 14

I : Intensity in the image plane in the transverse position $I(r_T)$

r_T : Position on the detector, $r_T = (x, y)$

$\varphi(r_T)$: phase retrieval function

\mathcal{F} : Fourier transform

H_p : filter in the frequency domain $H_p(w)$

\mathcal{F}^{-1} : Inverse Fourier transform

f : function for obtaining the phase

There are various phase retrieval algorithms (50) (51) which produces images analogous to the pure absorption contrast images, also reducing noise significantly, producing a cleaner reconstruction.

Besides it enables us to obtain quantitative information on the samples from phase-contrast images, it works best in the near field or close to it (44).

The algorithm of phase reconstruction used for the beamlines SYRMEP/Elettra and ID-17/ESRF was Paganin algorithm (52) :

$$\varphi(x, y) = \frac{\delta}{2\beta} \ln \left(F^{-1} \left\{ \frac{F[I(x, y)/I_0(x, y)]}{1 + [\lambda z \delta / (4\pi\beta)](u^2 + v^2)} \right\} \right) \quad \text{Eq. 15}$$

With:

- z : distance between object and detector
- d : characteristic size of the smallest discernible features in the object
- λ : X-ray wavelength
- (x, y) : coordinates in the image and/or object plane
- $I_0(x, y)$: incident intensity just upstream of the object
- $I(x, y)$: intensity distribution
- F : direct Fourier transform operator
- F^{-1} : backward Fourier transform operator

- δ : decrement from the unity of the x-ray refractive index of the object and are related to the complex-valued x-ray refractive index n , from Eq. 1.
- u and v : the complex conjugate coordinates of x and y respectively

Equation 15 is valid if:

- the object is a homogeneous material,
- if monochromatic radiation is used
- The distance z between object and detector is a near-field condition.

The ratio δ/β is an input parameter for the phase-retrieval, not the explicit values for β and δ , or in cases where the exact chemical composition of the sample material is unknown.

The sample-to-detector distance can be large enough to enhance the phase-contrast and applied to a Paganin filter (53).

Chapter II

Hardware

2. Hardware System

2.1. Microtomography System

A single source and a detector made up the first scanner generation. It had limitations but can be extremely useful in μ CT. This system has the advantages of relatively low set-up cost and excellent results for different types of measurements (54).

The commercially available components from a typical cone-beam micro-CT machine are an X-ray tube, a rotary stage, and a high-resolution detector (see Figure 18) (55).

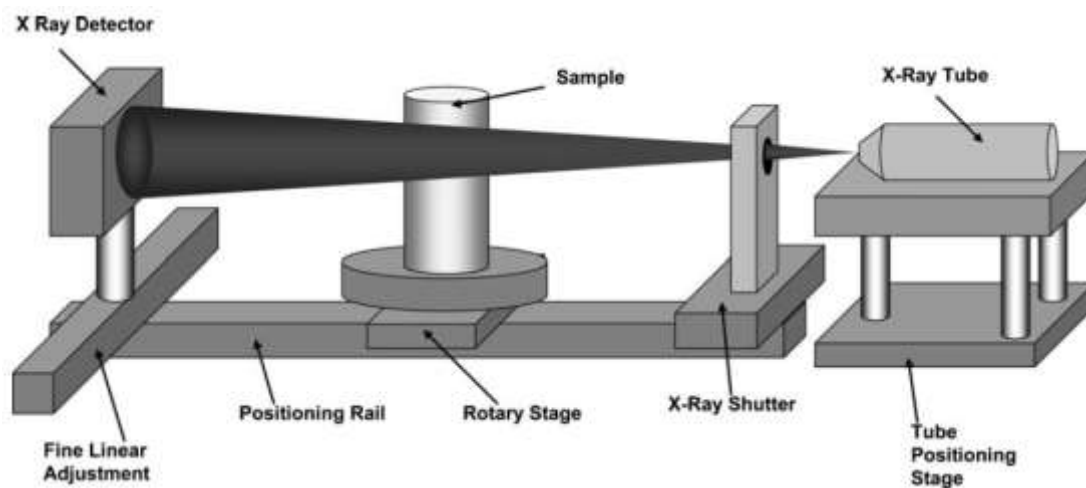


Figure 18: Typical cone beam micro-CT machine

The X-ray flux is an important factor for microtomography operation: an optimal energy source is needed that allows a greater number of photons to uniformly penetrate the material, depending on factors such as signal noise and the diameter of a sample. A further important aspect is that the X-ray power should be maintained constant over the data acquisition time (56). The main difference of micro focus-CT systems in relation to Synchrotron Radiation μ CT is linked to the X-ray source features. Figure 19(a) schematically shows that the synchrotron radiation produces monochromatic parallel beams whose divergence is 10^{-5} rad. Figure 19(b) indicates a micro-focus source with a polychromatic cone beam which diverges on 1 rad (57). The smaller the spot size, the smaller the penumbral blurring, which will help produce a more accurate projected image. A larger spot size means that photons hitting a specific pixel can be traced back through different ray paths through the specimen (2).

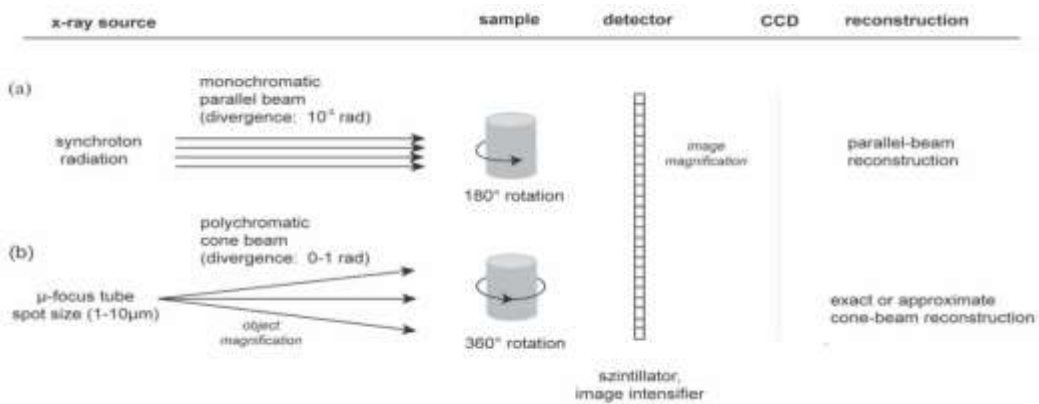


Figure 19: Difference between microfocus-CT systems and synchrotron system

The collimator is a component which permits the X-ray beam geometry to be focused in a fan- or cone-beam projection. A typical detector in microtomography system is a CMOS or CCD detector coupled with a phosphor (scintillator) screen (9). The sCMOS (Scientific CMOS) technology is now able to deliver performances that hybrid CCD/CMOS technology cannot: a unique combination of sensitivity, speed, dynamic range, resolution, and field of view (58). The sample composition and size determine which X-ray spectrum should be used (energy range). Another important parameter is the pixel size of the detector, the spatial resolution is equal to the pixel size divided by the magnification (59). The magnification ratio of the projection data is determined by SDD/SOD where SDD and SOD are the source-to-detector and source-to-object distances, respectively (see Figure 20) (60).

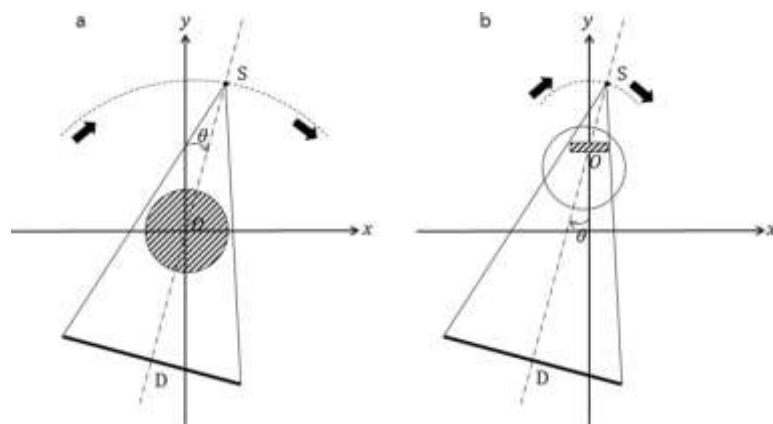


Figure 20: Position of detector respect of magnification ratio.

2.2. Acquisition in Microtomography

As already noted, a series of X-ray projected images is acquired and mathematically reconstructed to produce a 3D map of X-ray absorption in the volume. The 3D map is typically presented as a series of 2D slice images (see Figure 21) (2).

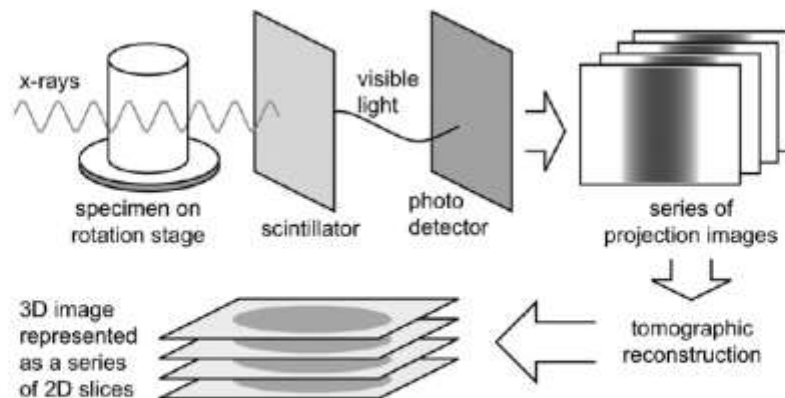


Figure 21: Schematic illustration of X-ray CT acquisition and reconstruction processes.

Acquisition of 2D radiographs require appropriate scintillation, to convert the X-rays to visible light, and detectors to produce a digital image. The application of 2D detectors allowed the acquisition matrix of data which represents 2D projection images, leading to faster scan times (2).

2.3. Syrmep Beamline - Elettra Sincrotrone Trieste

The beamline SYRMEP is part of the Elettra Sincrotrone located in Trieste, Italy. The 6.1 bending magnet source produces a laminar polychromatic beam that is shaped by using a vacuum slit system. A monochromator, based on a double-Si (111)-crystal, allows to obtain a monochromatic beam with an energy between 8 keV and 35 keV. An air slit system delimits the beam before entering the ionization chamber for the measurement of its intensity. At this point, the monochromatic incident beam enters the beamline SYRMEP

with a typical useful area of 210 mm x 5 mm at 20 keV. The sample stage is provided with 6 motors (M1-M6) for a fine positioning of the sample (see Figure 22) (61).

The measurement procedure involves, prior to the scanning, the alignment of the system (motors and slits) and the tuning of the optimal. The following step of the acquisition consists of fixing the number of rotational steps. Normally, before and after the sample scanning, acquisition of flat/dark field images is performed for the normalization in the reconstruction process (processing of the image). The first step of image post-processing is obtained by extracting the sinograms (61). The reconstruction of the of both absorption and contrast phase tomographic images is obtained by the STP (SYRMEP Tomo Project) (62).

The graph indicated simulation using a cubic sample with three white holes for scanning over the rotator plate until 1800 in the pre-processing image step shows the intensity profile in 1800, afterwards the reconstructed image from a sinogram is in the form of a 2D reconstructed image.

In Figure 22 we illustrate, enclosed by an orange dashed line, the part of our interest in the SYRMEP system, which comprises the programming of the apparatus control and data acquisition.

2.4. ID17 - Beamline - ESRF Grenoble

The ID17 is a biomedical beamline, part of ESRF - the European Synchrotron Radiation Facility, located in Grenoble, France, involving both diagnostic imaging and therapeutic irradiation for pre-clinical and potentially clinical application (See Tables 1-3) (63).

| | |
|----------------------------------|--|
| wiggler on a low β section | |
| critical energy | 33.5 keV |
| K_{max} | 19.6 |
| field B_{max} | 1.4 T |
| photon source divergence | $3.3 \times 0.1 \text{ mrad}^2$ (HxV) FWHM (at B_{max} , 33 keV) |
| total power emitted | 14.3 kW (at B_{max}) |

Table 1

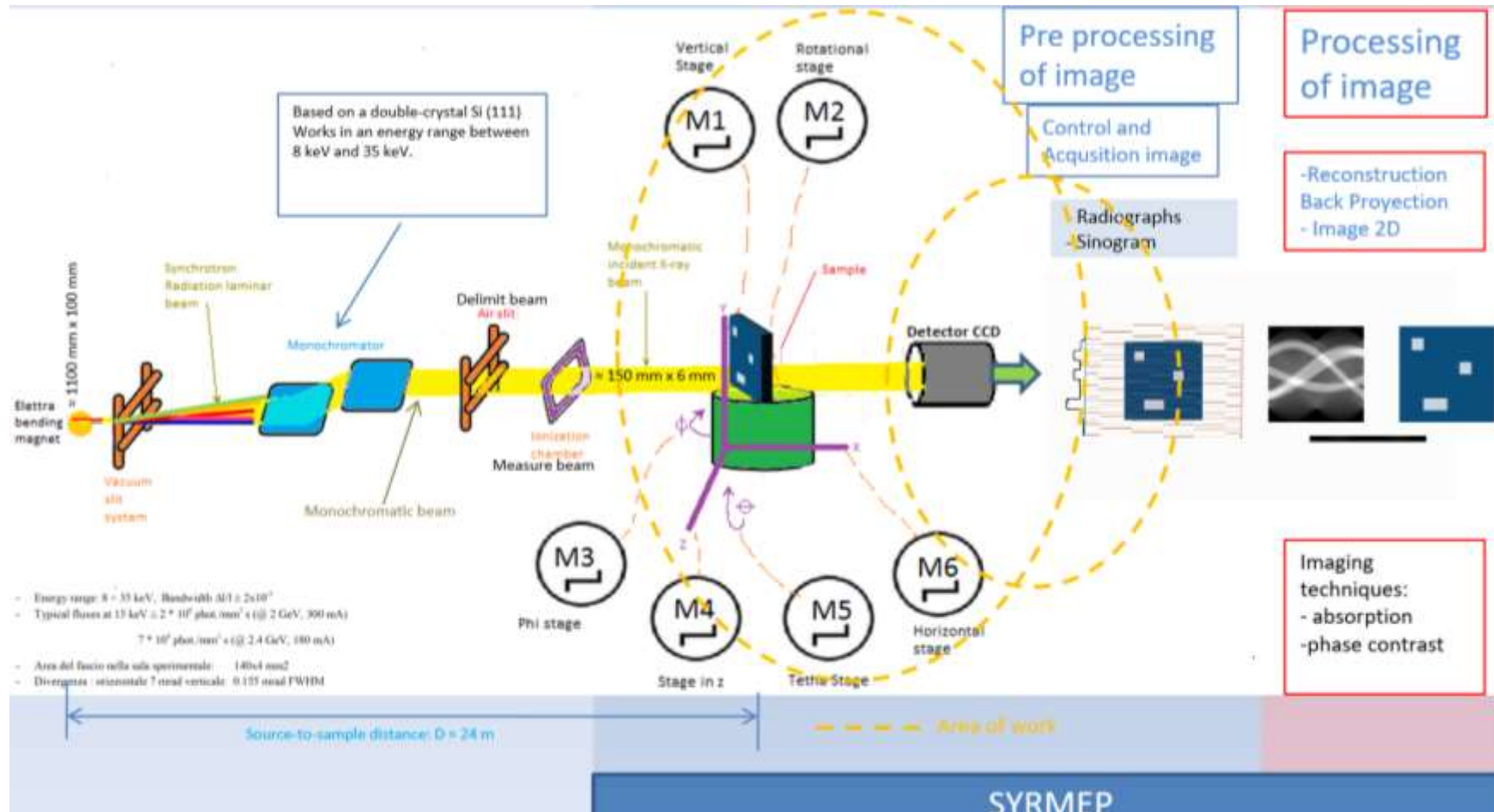


Figure 22: SYRMEP Beamline

| Optics | | |
|--------------------------|--|--------------------------|
| optical elements | Si-bent Laue crystal | fixed-exit monochromator |
| distance from source | 144 m (approx.) | 140 m (approx.) |
| used for | angiography | computed tomography |
| spectral range | 17-80 keV | 15-80 keV |
| max beam size at patient | 150 x 10 mm ² (HxV) (aperture limited) | |
| expected flux | 2.10 ¹⁴ ph/s, 0.1% bw, 0.1 A, mradh, at E _{max} , 33 keV, unfiltered | |

Table 2

| Detectors | |
|---------------------|--|
| angiography | Ge (2mm thick), 2 lines with 432 elements each (pitch 350 μm)-current integration mode |
| computed tomography | FRELON Camera with taper |

Table 3

The X-ray beam is generated by an 11-period wiggler with a maximum magnetic field 1.592 T at a wiggler gap (Figure 23). The probed object is moved vertically through the beam while the CCD camera constantly acquires projection images (64).

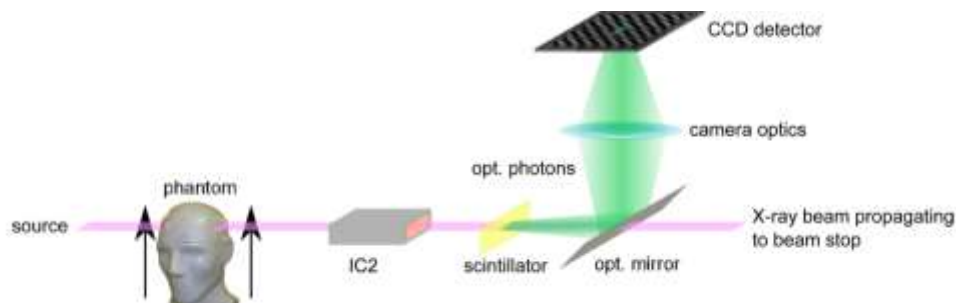


Figure 23: ID 17- Schematic description of the imaging setup.

The ID17 wiggler is a neat way to increase the intensity of synchrotron radiation. It is a periodic arrangement of dipole magnets generating an alternating static magnetic field which deflects the electron beam sinusoidally (65). The filters are also placed as beam attenuators. They are located between the source and the sample to avoid overheating of the optical elements in the optic hutch (66).

2.5. STAR Facility

The STAR facility at the University of Calabria, in Rende (CS, Italy), is currently under commissioning. STAR source is the first user-facility, created for the

material science community based on the Thomson Backscattering (or inverse Compton) effect. The STAR source is formed by a S-band photo-injector producing 5 MeV electron bunches at 100Hz, a S-band LINAC accelerating the electrons up to 60 MeV feed by a dedicated Klystron; an integrated laser system constituted by two lasers (one feeding the photo-cathode of the photo-injector, one driven to the interaction point). X-rays are emitted for the Thomson Scattering mechanism when the accelerated and focussed electron bunches collide with the focussed laser beam. The X-rays collected in the backscattering geometry are polarized, monochromatic, tuneable with continuity between 40 and 140 keV, shaped in pulses of a of few picoseconds duration and with a flux of the order of 10^9 photons/s (67) (68) (See Figure 24).

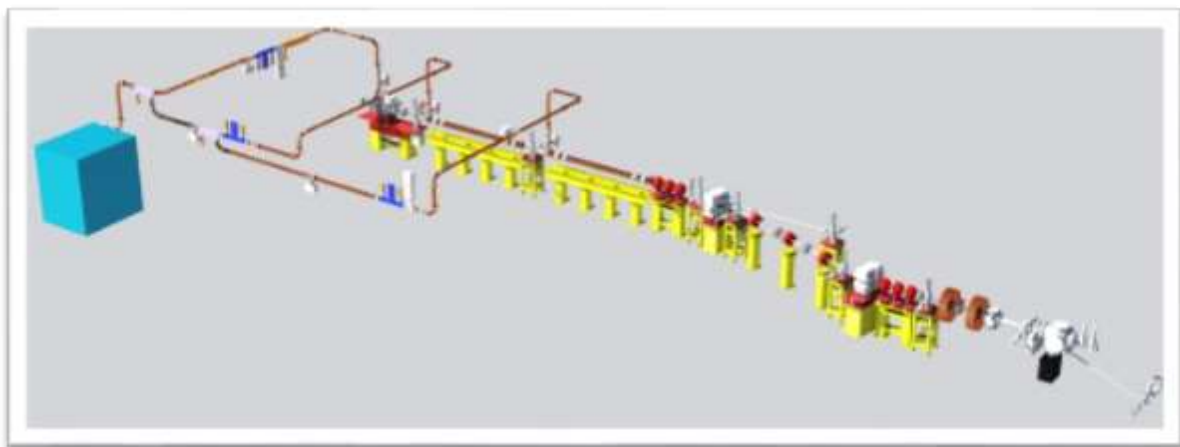


Figure 24: STAR Facility

2.6. μ Tomo Laboratory at STAR

μ Tomo Laboratory is part of the STAR-Lab facility realized under the PON MaTeRiA project. It is located into the University of Calabria campus in Italy. The μ -Tomo Experimental Station consists of three precision optical tables Thorlabs mod. B6090B, equipped with a microfocus X-ray source, five motion cradles, and a flat panel detector.

The sample handling system provides four degrees of freedom, while the fifth degree (ϕ), corresponding to one of the cradles needed for sample alignment, is placed under the detector to reduce the weight to be manipulated. This system allows to position with

the required sample precision up to 80 mm in diameter and 6 kg in weight. The particular arrangement of the actuators enables tomography to be performed both in full beam mode (where all the irradiated sample is always contained in the field of view of the detector during rotation) and in the half-beam one (where the maximum dimensions to be captured exceed the maximum transverse dimension of the detector, but no more than a factor 2). Some features of the system are shown in Table 4 with reference to Figure 25.

| Specifications | | | | | |
|-----------------------------------|--------------------|---------------------|-----------|-----------|----------|
| PI-Micos Model | LS-270 | LS-180 | WT-90 | WT-90 | PRS-110 |
| Load Capacity (Kg) | 150 | 100 | 8 | 8 | 10 |
| Load Capacity (N) | 1500 (Fz) | 200 (Fy) | 80 (Fz) | 80 (Fz) | 100 (Fz) |
| Travel range | 205 mm | 155 mm | 90° (max) | 90° (max) | >360° |
| Bi-direc. Repeatability (down to) | 0.05 μm | 0.05 μm | 0.001 ° | 0.001 ° | 0.0002° |
| Maximum speed (mm/s) | 150 | 200 | 15 | 15 | 200 |
| Type limit switch | Inductive (pnp) NC | mechanical (pnp) NC | npn* | npn* | npn* |
| Location on μ-Tomo Station | X-axis | Y-axis | Phi | Tetha | Omega |

NC: Normal-closed

* : internally by jumper

Table 4: Motors Characteristics

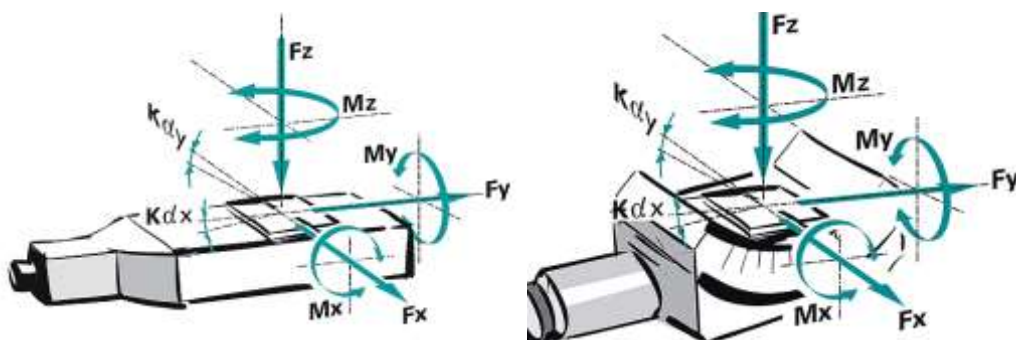


Figure 25: Reference of motors

The μ Tomo station is provided with a user interface that allows its control through a personal computer. In particular, give the possibility of:

- Place the sample (4 degrees of freedom);
- Orient the detector (1 degree of freedom);
- Set the operating parameters of the detector;
- Acquire images from the detector.

The Microfocus X-ray source is the Hamamatsu L12161-07 one whose main characteristics are:

| Parameter | Value | Unit |
|---------------------------------------|----------------------|---------|
| X-ray tube voltage setting range | 0 to 150 | kV |
| X-ray tube current setting range | 0 to 500 | μ A |
| X-ray tube voltage operational range | 40 to 150 | kV |
| X-ray tube current operational range | 10 to 500 | μ A |
| Maximum output | | |
| - Small Focus Mode | 10 | W |
| - Middle Focus Mode | 30 | W |
| - Large Focus Mode | 75 | W |
| X-ray focal spot size (Nominal value) | | |
| - Small Focus Mode | 7 (5 μ m at 4 W) | μ m |
| - Middle Focus Mode | 20 | μ m |
| - Large Focus Mode | 50 | μ m |
| X-ray beam angle | Approx. 43 | degree |
| Focus to object distance (FOD) | Approx. 17 | mm |

Table 5: Microfocus characteristics

The used detector is a Flat panel sensor C7942SK-05 from Hamamatsu – Japan. Its main features are:

| Parameter | Value | Unit |
|--------------------------|-----------------------------------|----------|
| Energy range: | 150 | kVp Max. |
| High quality image: | 5.4 | Mpixels |
| Pixel size: | 50 \times 50 | μ m |
| Digital output (12-bits) | | |
| High-speed imaging: | 2 frames/s (single binning) | |
| | 9 frames/s (4 \times 4 binning) | |

Table 6: Detector characteristics

The whole system allows to control the X-rays test source managing; the sample-under-test (SUD) moving, using five high precision stepper motors; the image acquisition, by means of a flat panel detector, subsequent made the 2D and 3D image reconstruction, thanks to an open-source reconstruction tool.

The micro-tomographic experimental station, named μ Tomo, was set up to exploit the hard X-rays produced by the STAR source. Both, the electronic hardware and mechanical design of the μ Tomo system was realized by Elettra Sincrotrone Trieste SCpA. Currently, the μ Tomo Laboratory is equipped with a micro-focus X-ray tube and a flat panel for μ -CT; these devices are remotely managed from a control room for the images acquisition.

All the electronic hardware components are commercially available and are, in general, provided with software drivers which are LabVIEW compatible (55).

The microtomography system is equipped with reliable components such as the stepper motors: low cost, can work in open loop, excellent holding torque and low speeds, low maintenance (brushless), very rugged in any environment, excellent for precise positioning control and no tuning required (69).

“Figure 26” shows the mechanical assembly of the μ Tomo STAR Experimental Station. There are five motors for each degree freedom in the experimental station:

- A goniometer WT-90, 2SM, MLS model corresponds to the Φ axis.
- A goniometer WT-90, 2SM, MLS model corresponds to the θ axis.
- There is a rotator PRS-110, 2SM, MLS model.
- A translator LS-270 model corresponds to the x-axis.
- A translator LS-180 model corresponds to the y-axis.

The goniometer WT-90 designed for all tasks where conventional rotation stages cannot be used due to limited space conditions (70). The two goniometers are mounted orthogonally under the rotator with a common center of rotation.

The Linear Stage LS-270 was developed for positioning tasks with high loads, up to 150 kg and allows velocities up to 150 mm/s (71).

LS-180 Linear Stage for heavy loads had high travel accuracy and load capacity up to 100 kg and allows velocities up to 200 mm/s (72).

The detector, a C7942SK-05 flat panel sensor, is a digital image sensor newly developed as a key device for non-destructive inspection and for X-ray imaging applications requiring high image quality. Its principal characteristics are 150 KVp max., resolution of 5.4 Mpixels, the pixel size of 50 x 50 μm and high-performance GOS scintillator (73) (See Table 7).

| Parameter | Specification | Unit |
|---|------------------------------|---------------|
| Pixel size | 50 × 50 | μm |
| Photodiode area | 120 × 120 | mm |
| Number of pixels | 2400 × 2400 | pixels |
| Number of active pixels | 2316 × 2316 | pixels |
| Readout | Charge amplifier array | - |
| Video output (Data1 - 12) | RS-422 (differential) 12-bit | - |
| Output data rate | 15.15 | MHz |
| Synchronous signal (Vsync, Hsync, Pclk) | RS-422 (differential) | - |
| bin0/1, ExtTrgGrb, ExtTrgLemo, IntExt | TTL | - |
| Scintillator | GOS | - |

Table 7: C7942SK-05 - Functional Specification

The detector moves manually over a rail in the z-axis. At full performance, it uses an external frame grabber board, in binning or trigger operation.

The microsource is a Hamamatsu model L12161-07 whose features are a minimum focal spot size of 5 μm at 4W, 75 W maximum output, 42° cone aperture and a control via the RS-232C interface (74) It can move manually along the y-axis and z-axis in the alignment process.



Figure 26: Experimental Station - μTomo

The equipment is schematically depicted in Figure 27. Two motors (WT-90 model) are attached to axis-1 and axis-3 connectors, respectively, while a third one (PRS-110 model) is attached to axis-2 one of the Corvus-Eco controller, which in turn is an interpreter of Venus-1 commands. The motors of the linear translation (model LS-270 and model LS-180) are attached to axis-1 and axis-2 connectors of the Hydra controller. The Corvus-Eco controller, the Hydra controller, and the X-ray Control Unit are connected over the serial interface to Moxa Nport. Finally, the Moxa Nport and CMOS flat panel sensor are connected with Cat 5e UTP to the server and room control, respectively.



Figure 27: Connection diagram

An isometric view of the μ Tomo Experimental Station is reported in Figure 28. Here, we show the sample placement into the FOV and the ROI.

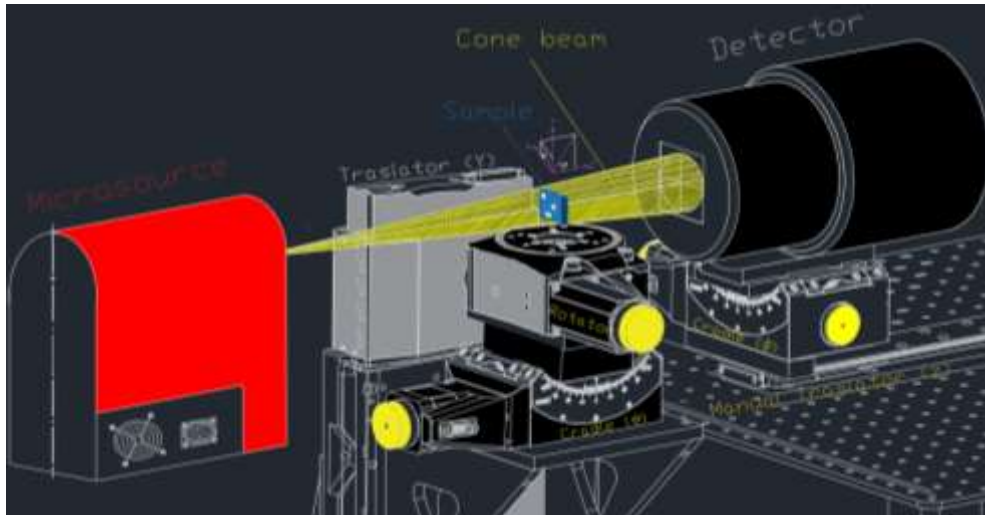


Figure 28: Alignment of experimental station

Regarding the EPICS connection, the upgraded hardware consists of adding a client and EPICS server to the network for μ -CT experiments. The control based on LabView over EPICS platform was developed at the μ -Tomo Laboratory of the STAR facility, sited at the University of Calabria, Italy. The versatility of system permits operated with microfocus (μ Tomo Laboratory) or TBS source over EPICS platform and permit exploit all the characteristics of light (See Figure 29).

2.7. Hardware Beamline Syrmep for acquisition

The μ Tomo beamline is like the SYRMEP one, illustrated in Figure 30, as concern the diagram of connection. The remote control from client to server is given by a UTP line while the server is connected to the sCMOS detector and to the rotator by means of a Moxa and a Mercury Controller.

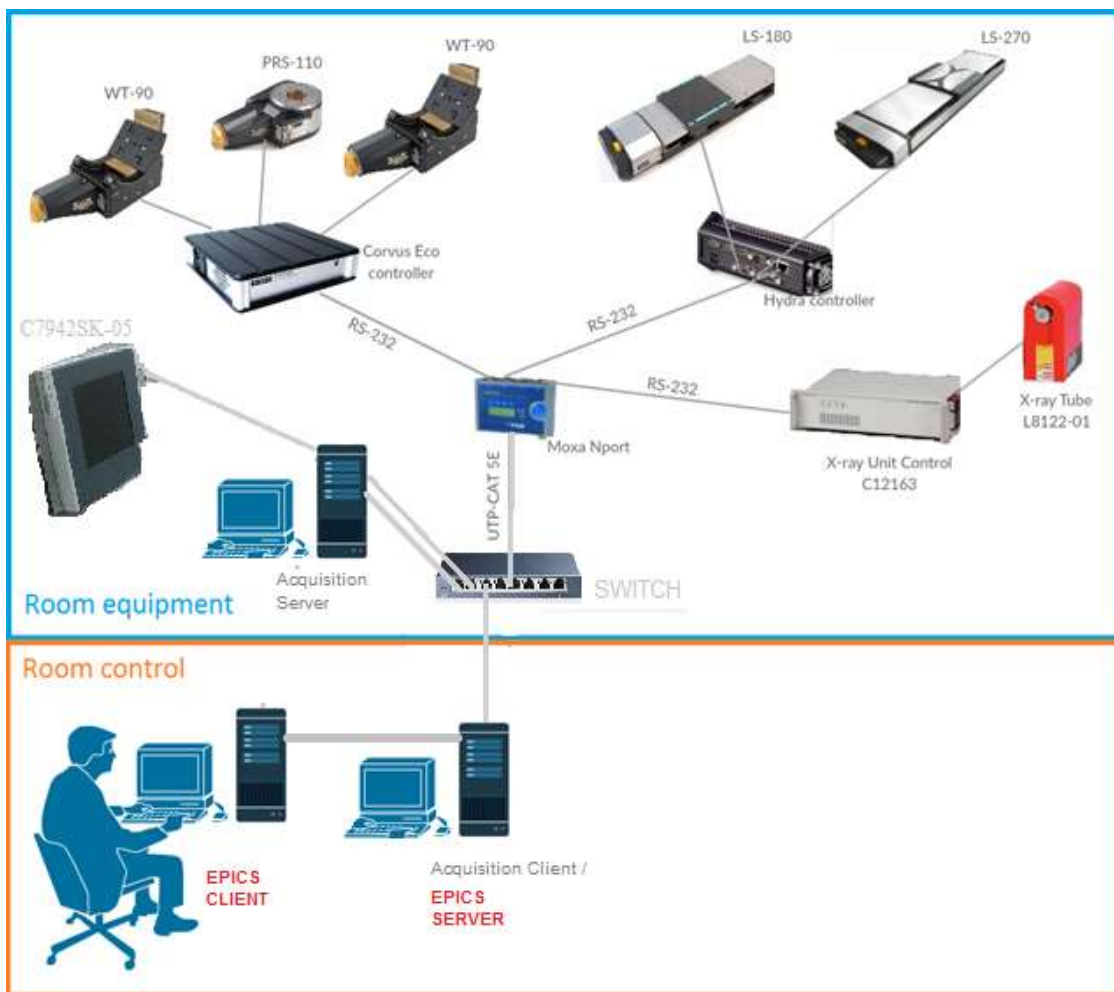


Figure 29: EPICS - Connection Diagram

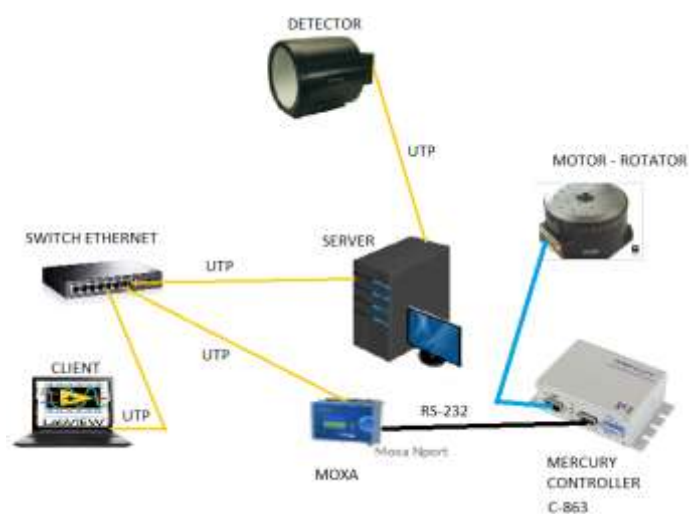


Figure 30: SYRMEP setup for acquisition

Chapter III

Software Development

3. Software Development

The μ Tomo software was developed using LabVIEW to control the hardware by means of a graphical user interface (GUI). LabVIEW is a graphical programming language. It has a powerful function library and an easy-to-use multithreaded programming and graphic user interface (GUI) design. The availability of drivers, debugging, and other features make it an ideal software for instrument-oriented programming (75).

The developed software is flexible allowing easy changes or additions of the hardware. The RS232 serial interface is the communication standard for most of the used laboratory equipment (Microfocus X-ray source and motors).

3.1. The Main Program

The main program was created using the 2015 version of LabVIEW. An installer is also created to be executed in computers without LabVIEW already installed or with older version of the same program. The software can be used on both 32 bits or 64 bits Windows environment.

Figure 31 shows the front panel of the Main Program while Figure 32 depicts a synthesized code of the Block Diagram which consisted in three subroutines, two for the motors and one for the acquisition sequence respectively. The front panel has a menu divided into four parts: 'Phi/Theta', 'X-Y-Rotator', 'Acquisition' and 'File Parameters' for the complete control of the μ Tomo apparatus.

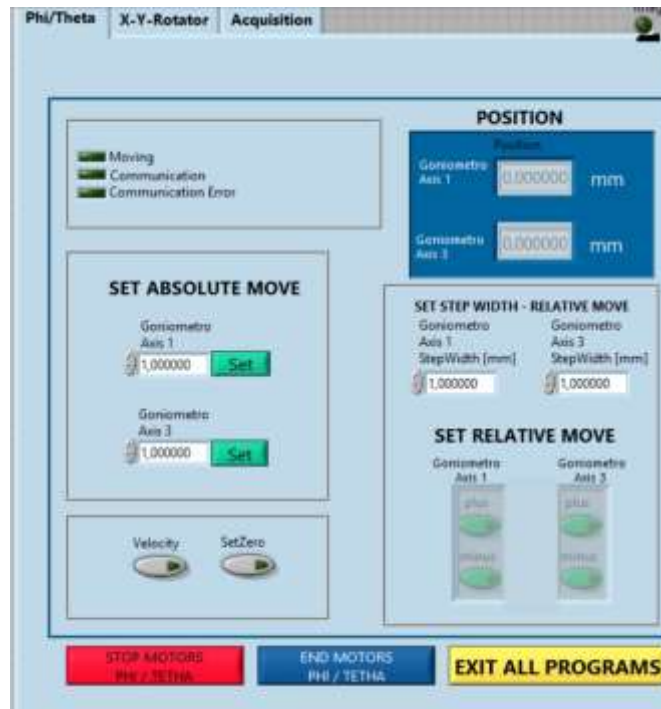


Figure 31: Front Panel

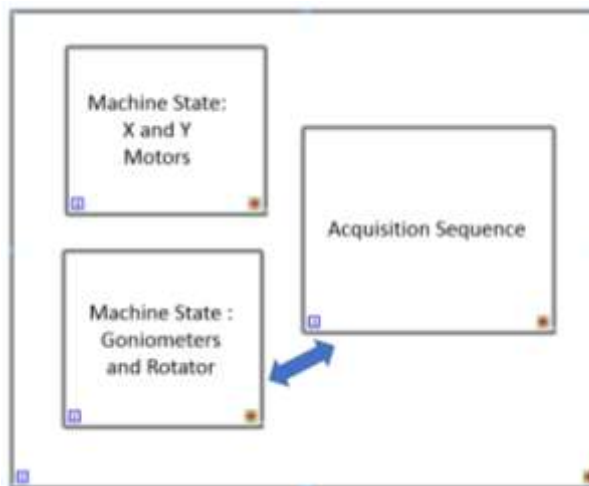


Figure 32: Block Diagram

3.1.1. Control Motors

The motor control programming was carried out taking as a reference the software TestProgram.vi of the Mechanische Instrument Optische System (Micos) (76).

The main modifications made to the program are listed below:

3.2.1.1. Creation of independent menu for 2 axes (Phi/Theta)

Figures 33-35 show the code for Phi/Theta control for axis-1 and axis-3 respectively. This menu permits the Corvus controller to work for stepper motors:

Phi: Axis 1: WT-90, 2SM, MLS

Theta: Axis 3: WT-90, 2SM, MLS

The menu allows to verify the communication status, eventual errors, the performed movements and to set the velocity and acceleration.

Furthermore, the following operation were implemented:

- Set the absolute movement for the two axes using an independent absolute step width for each axis such as shown in the diagrams in Figures 33 and 34:

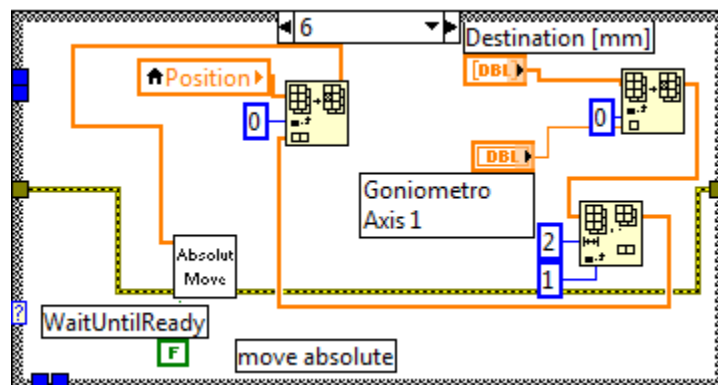


Figure 33: Absolute movement - Axis 1

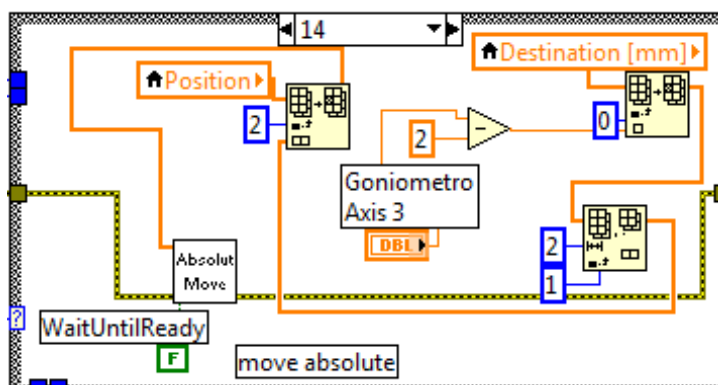


Figure 34: Absolute movement - Axis 3

- Set relative movement only for two axes, using independent relative step width for each axis, (see Figure 35).

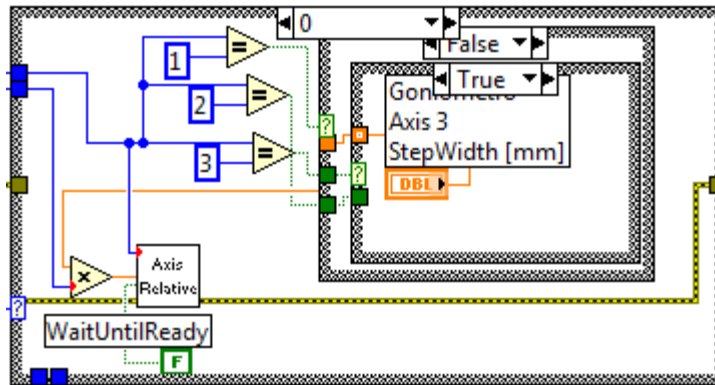


Figure 35: Relative movement

- Control the state of stop or end for the motors.
- Permit visualization of the position in real time for the two axes.
Update the position of each axis every 50 ms

3.2.1.2. Creation of menu for rotation and X and Y movements

The menu depicted in Figure 36 is relative to the Corvus controller (control of the stepper motor relative to the axis rotator: PRS-110, 2SM, MLS) and of the Hydra controller (control of the stepper motor relative to the Y-axis - LS-270 - and X-axis - LS-180).

The front panel divided into two parts, the upper part refers to X-axis and Y-axis while the lower part is relative to the rotator. The programming is based on the Demo.exe program (78) (79) and permits setting the absolute and relative movements for the X-axis and Y-axis in the microtomography system by means of Ethernet and/or RS-232 communication. The characteristics of this menu are:

- Position: present position, returned from the controller for each axis.
- Relative movement: negative or positive direction.
- Absolute movement: the parameter is the target position starting at the present position.
- Stop: Stops motion of the axis
- Initializing of motors for each axis.
- Reset to zero the value of the position
- Initial Calibration: for alignment of sample using ncal and nrm buttons.

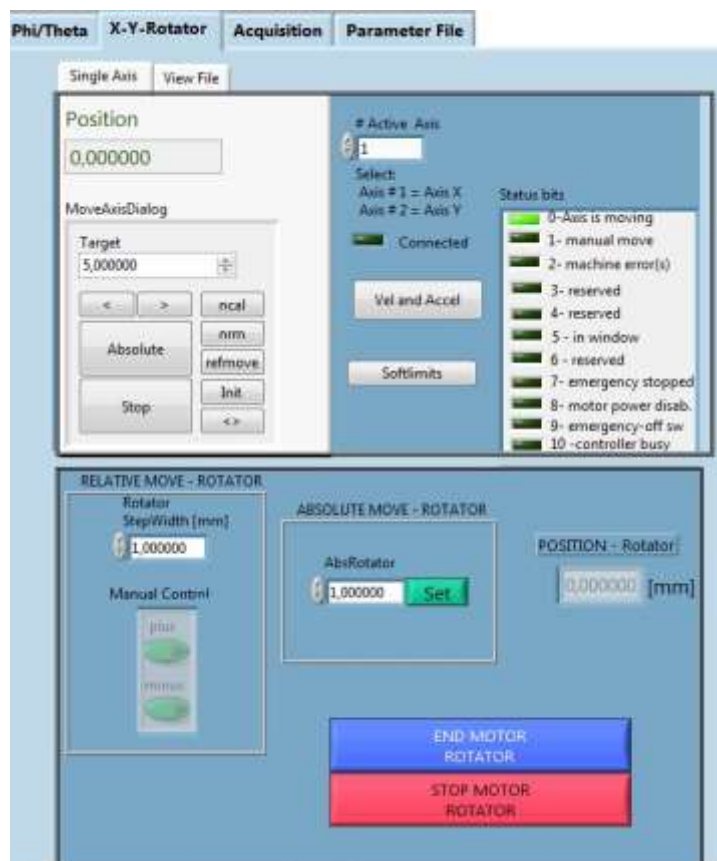


Figure 36: Control rotation, x and y movements

Figure 37 shows the 'view-file' tab, permitting opening and uploading the configuration file with txt extension. The actual configuration is also reported: the status bits permit the principal activities of the hydra controller to be displayed. If the motor power is disabled,

it is possible to use the "Init" button for enabling the power; this procedure is necessary to initialize the controller. A series of Boolean variables are displayed to show the status of the apparatus. As an example, in the next figure, the label "Axis is moving" is ON because a relative or absolute movement is under way.

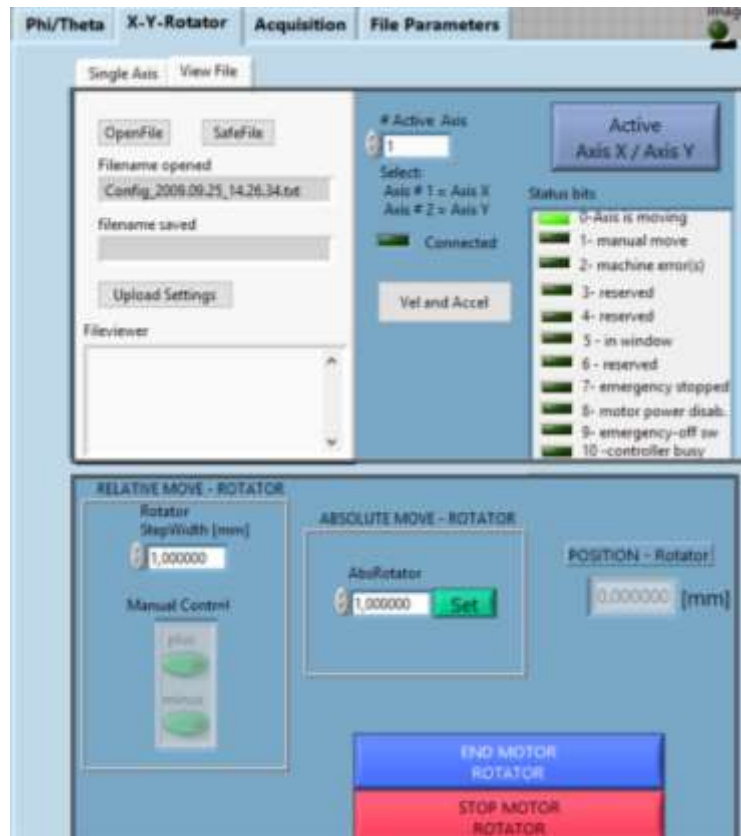


Figure 37: Hydra – View file

An error handling procedure is also coded: while the 'machine errors' virtual led is off then bit 4 is OFF, but the condition for the error may not be removed (emergency stop is active). In all these cases, the bit 8 is active and shows an enlighten virtual led. If the emergency condition is removed, then it is necessary to press the button 'Init' to activate the power stage of the controller and no reset must be sent to the hydra controller (79). Among other modifications made to the program we have the setup the absolute

movement for one axis, using an independent absolute step width for each axis. (see Figure 38):

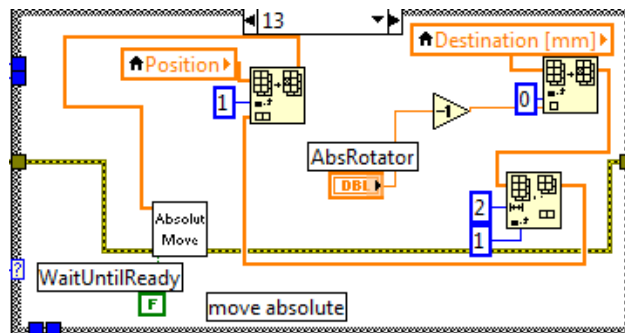


Figure 38: Absolute movement for rotator

3.1.2. TCP/IP Acquisition

Figure 39 indicates the front panel of TCP/IP acquisition. Its menu allows:

- Inserting of the number of images to be collected (up to 9999)
- An image counter which shows the current number of the acquired images.
- Giving a prefix for each image filename; dark, flat and projection are set automatically
- Stop the acquisition by using the button "Exit All Programs".
- Set and read the exposure time..

Figure 40 shows a typical parameter file that can be updated by the user to insert the acquisition parameters prior to scanning. The program saves the parameter file automatically in the same folder of the acquired images.

Figure 41 indicates the block diagram for the acquisition procedure. As a preliminary step, the input signal calibration is needed, allowing the control of the acquisition parameters of each image in accord with the movement of the rotator.

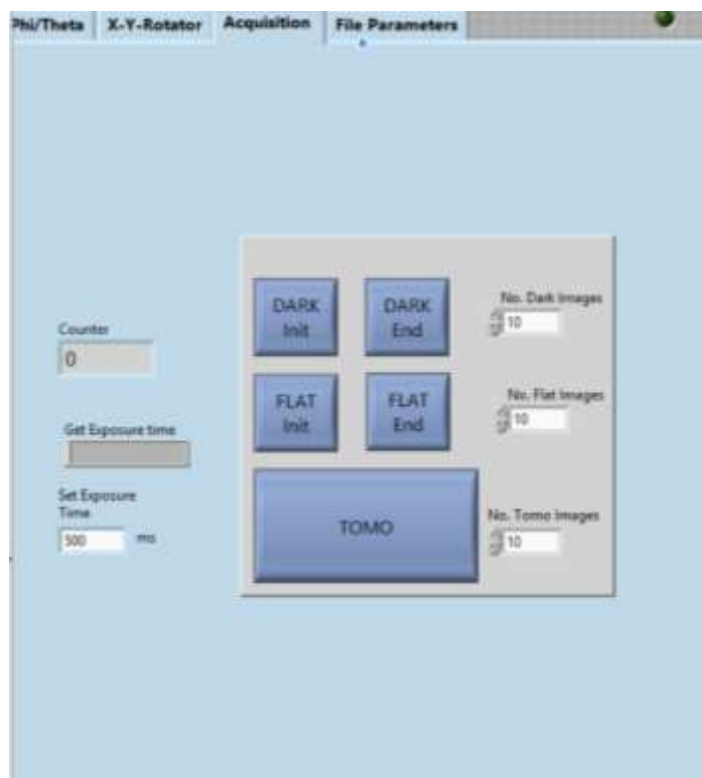


Figure 39: Front Panel - TCP/IP Acquisition

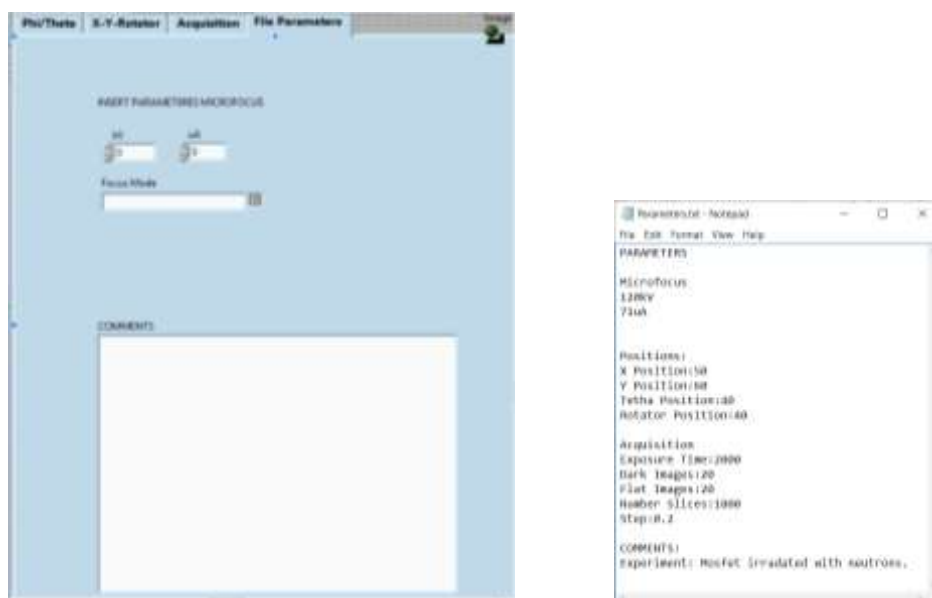


Figure 40: File Parameters

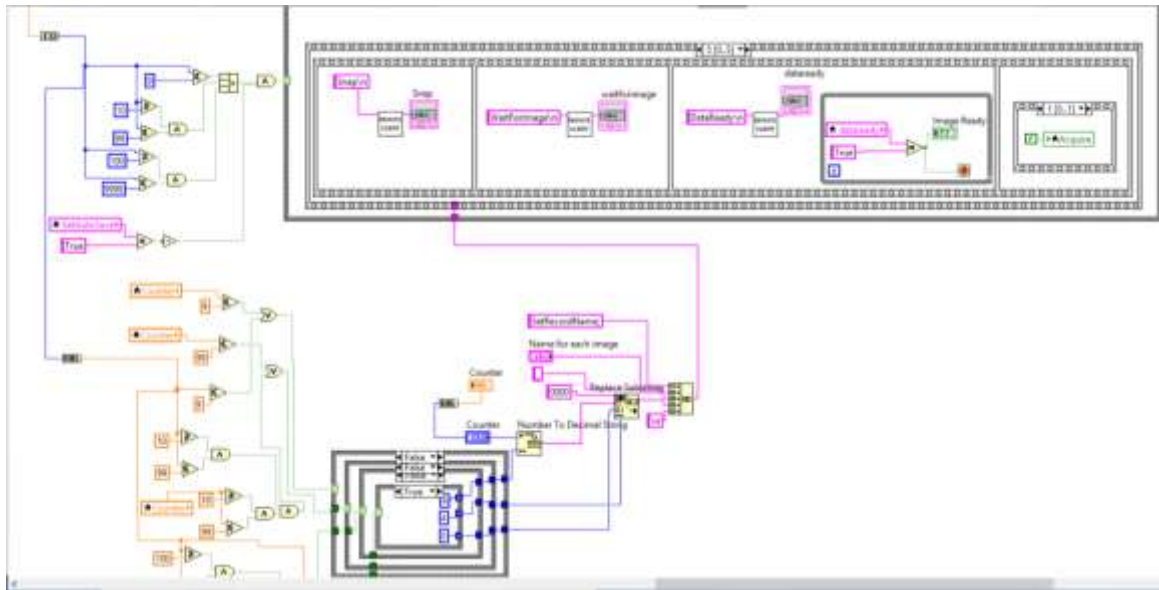


Figure 41: Block diagram – Acquisition

3.1.3. Subprograms Link

The remote acquisition procedure consists on the setting of the motors positions according to the size of the sample for a suitable acquisition. Successively the acquisition module is linked to the rotator control module. The signal "Image Ready" indicates when an image is acquired (see Figure 42).

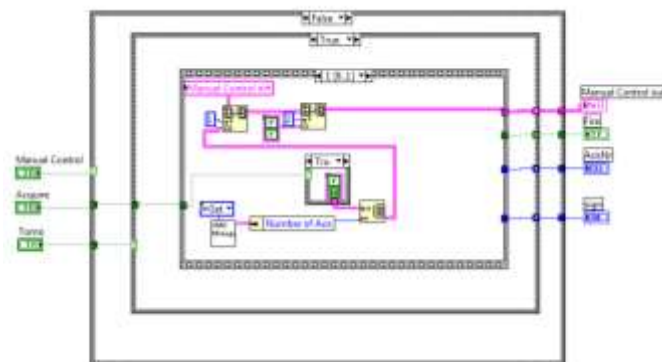


Figure 42: Block diagram. Link between Subprograms and Main Program

3.2. Upgraded to EPICS I/O Server

EPICS is a set of Open Source software tools, libraries and applications developed collaboratively and used worldwide to create distributed soft real-time control systems for scientific instruments (80).

EPICS was chosen as the software environment for the control of the STAR infrastructure and, thus, there is a need to let the whole μ Tomo acquisition process be controlled by a proper linkage between this software and Labview.

The linking of the Epics Server with the LabVIEW environment consisted in creating a LabVIEW Project containing both the necessary VIs (virtual instruments) and PVs (Process Variables) (see Figure 45). LabVIEW module allows the user to read, initialize or monitor the state of the networks variables (see Figure 46) by using DSC (Data-logging and Supervisory Control). The developed Epics client GUI, by controlling these variables, makes the μ Tomo images acquisition possible. The Epics server manages the channel access to network variables and allows it to be read by an Epics client. A Distributed System Manager allows monitoring the Epics Process Variables.

Figures 43 and 44 show the front panel and block diagram of the Epics Server.

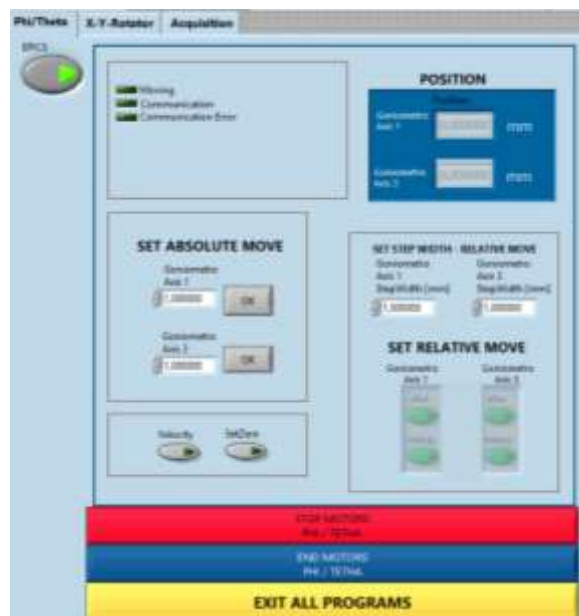


Figure 43: Front Panel – Epics Server

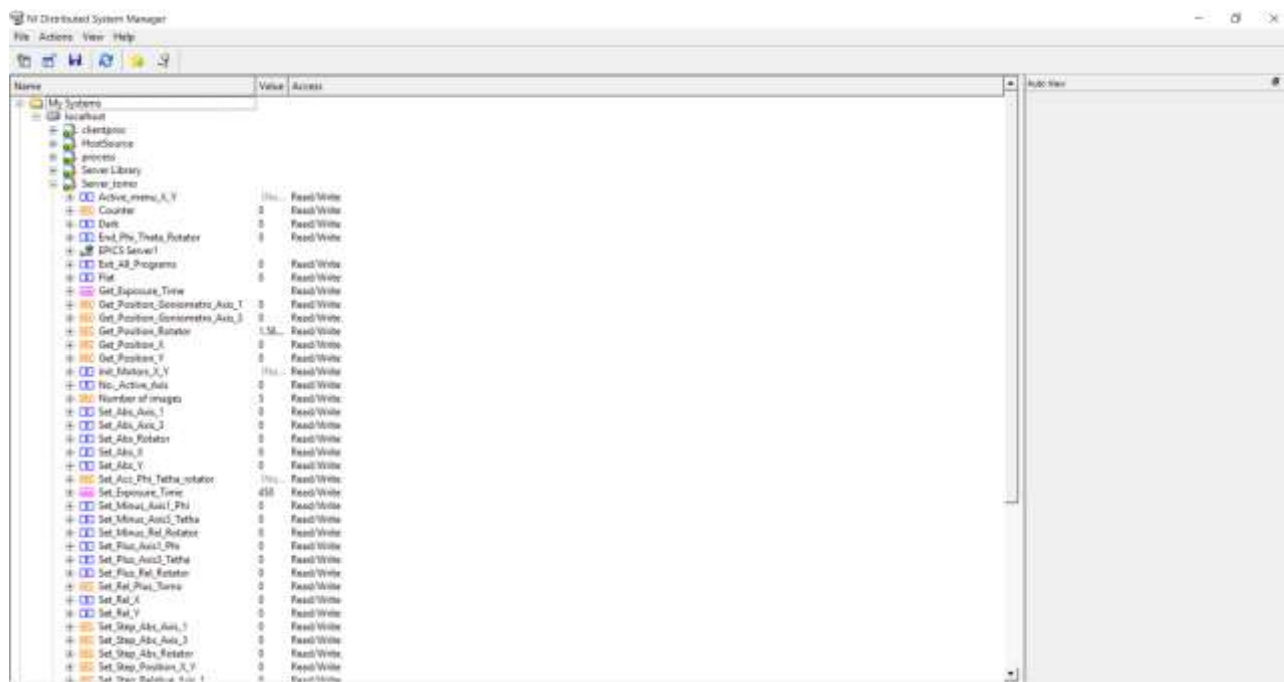


Figure 46: Monitoring Epics Process Variables with Distributed System Manager

3.3. Alternative Software for image acquisition – SYRMEP beamline @ Elettra

During a period spent at Elettra Sincrotrone (Trieste), a similar software was developed for image acquisition by remote control on TCP/IP at the SYRMEP beamline. Figure 47 shows the code on LabVIEW for the “detector control” and the “rotator control”.

The sCMOS detector connected to the server is controlled on the TCP/IP of the client. As a starting point, it is necessary to configure the communication parameters, by starting the server and verifying the communication.

For the rotator, it is necessary to configure the serial communication parameters of the C-863 Mercury Controller connected to the rotator. Figure 47 indicates the blocks of acquisition: range of images for select the number of images for acquire, generator of names for each image and communication of commands for transmission and reception. The rotator is verified its rotating, when the control the response to the specific command

'ONT?'. Also, in this case, the initial settings for image acquisition should provide the number of images before acquisition.

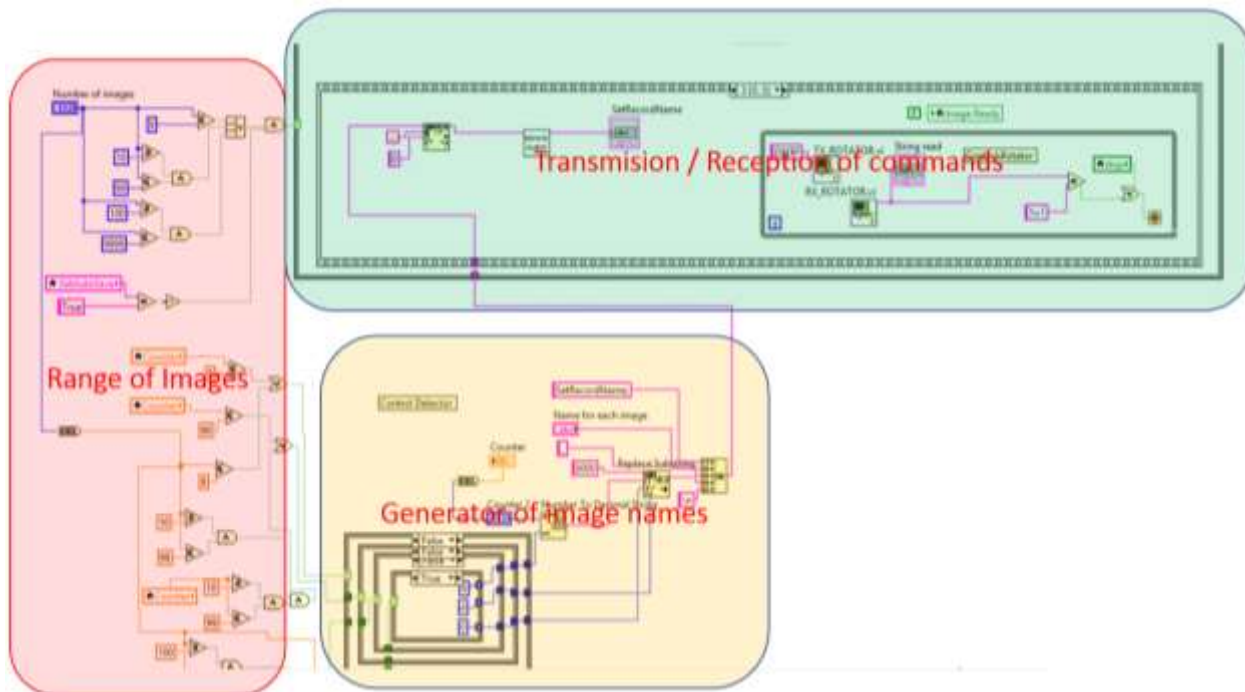


Figure 47: Alternative Software for acquisition image

3.4. Development of Graphic User Interface (GUI) in Python Language - ID17 beamline @ ESRF

A Graphic User Interface (GUI) was developed in Python Language for ID17 beamline in ESRF (Grenoble – France). It was designed for online image reconstruction during experiments. Autonomous handling of reconstruction software and the specific routines were developed for the specific users.

The main goal of the GUI is to provide a user-friendly multi-technique platform that can be used to handle the data obtained with different phase-contrast techniques like Propagation-based imaging (PBI).

PBI requires that the detector is positioned at a chosen distance from the sample (81).

The code was structured into different classes and methods. PyQt, a Python graphic tool, brings together the Qt C++ cross-platform application framework and the cross-platform interpreted by the Python language (82). The PyQt library is used for the GUI. PyQt is a set of Python v2 and v3 multiplatform bindings. Figures 48 and 49 illustrated the templates:

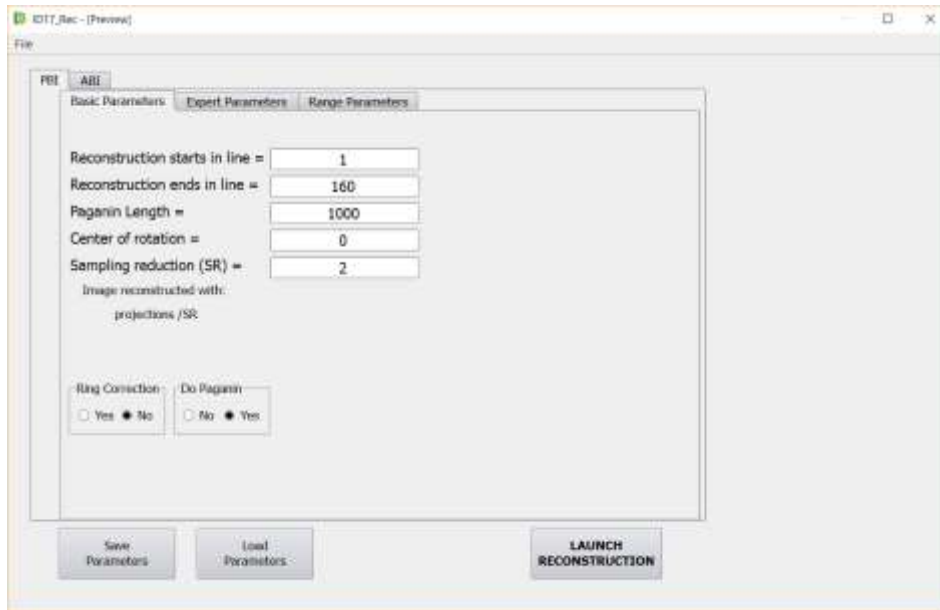


Figure 48: Template of Basic Parameters

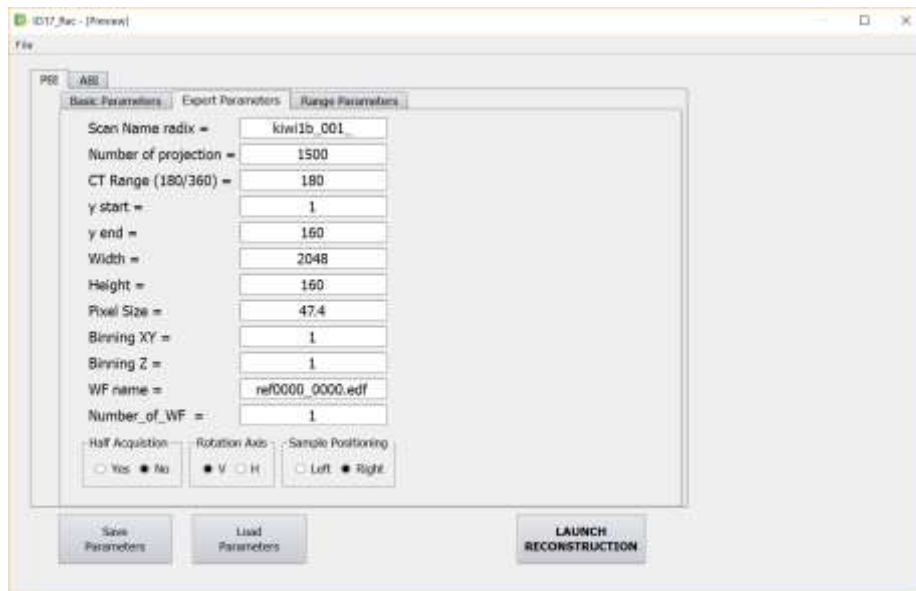


Figure 49: Template of Expert Parameters

The template program is linked to the functions grouped into classes in the python code, according to the python code made by Alberto Mittone, scientist of ID17 beamline staff. The template generates a text file, according to the instructions manual of ID17 (83) For details, see the Annex 1.



Figure 50: Template of Range Parameters

The main parameter that are controlled by the ID17 GUI are:

COR range (Center of rotation)

This parameter allows linking to the script to reconstruct a single slice of the volume concerned using different centres of rotation in the range. The CT files are saved in the COR folder. The folder is created automatically (see Figure 50).

Delta-Beta range

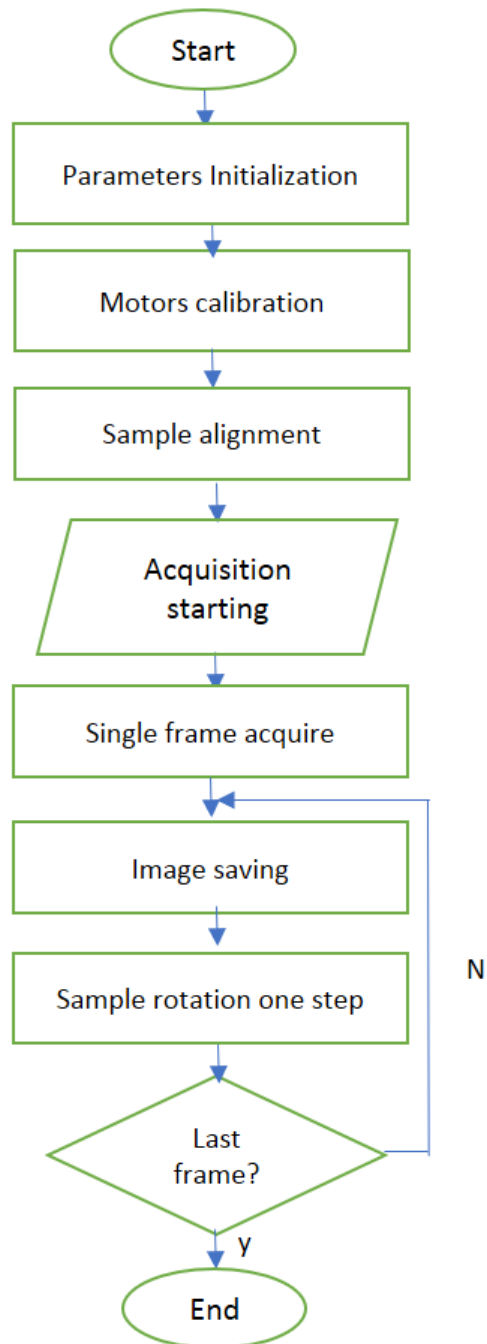
This parameter allows linking to the script to reconstruct a single slice of the volume concerned using a different specific parameter (Paganin number) in the range. The CT files are saved in the PAG folder. The folder is created automatically (see Figure 50).

Software operation mode

The GUI allows the following operations:

- “Save Parameters” Boolean controls the writing of the user and basic parameters used for reconstruction in a text file.
- “Load Parameters” Boolean controls the updating of the user and basic parameters reconstruction from a text file.
- The possibility of performing reconstructions automatically using a range of parameters (i.e. different centres of rotation and different values of delta/beta values using a single distance for the non-iterative phase retrieval algorithm described by David Paganin) (84). Phase retrieval enables us to obtain quantitative information about the sample from phase-contrast images (85).

3.5. Flowchart



Chapter IV

RESULTS AND DISCUSSION

4. Results and Discussion

4.1. Experiment 1: Non-destructive Measurements of Single Events Induced on Power MOSFETs by Terrestrial Neutrons

X-ray microtomography has been employed for non-destructive measurements on Power MOSFETs with the aim to investigate the damage due to "Single Events Effects (SEEs)" induced by high energy neutrons in accelerated tests. The technique allowed to investigate the spatial structure of the neutron induced damages. The results show that the technique and the methodologies employed to investigate SEEs in electronic devices could represent a suitable non-destructive investigation tool both for the post-failure analysis and for the individuation of constructive defects due to the industrial process.

4.1.1. Introduction

Electronic devices are employed in several applications and they are subjected to effects of the environment in which they work. In some of these applications (space, aircraft or ground), these components are subjected to the Natural Radiation Environment (NRE), composed of heavy ions, protons or neutrons (86). The interaction of these particles with the devices causes damages that could change the devices features or could destroy them. Power MOSFETs, largely employed in avionics, automotive and energy production and transformation, are sensitive to the interaction of high-energy terrestrial neutrons. The interaction of a "single" neutron with the device could cause the so-called Single Event Effects (SEEs).

Single Event Burnout (SEB) and Single Event Gate Rupture (SEGR) are destructive SEEs that affect Power MOSFETs during their work (87) (88) (89) (90) (91). Literature furnishes models of SEB and SEGR that describe how the interaction of a single high energy neutron could cause the device destruction (92) (93) (See Figure 51).

Up to now, investigations on the structure of the SEEs have been performed by means of destructive tests. X-ray microtomography with flat-panel matrix detectors and X-ray micro-focused source is a non-destructive technique able to provide advanced 3D-images.

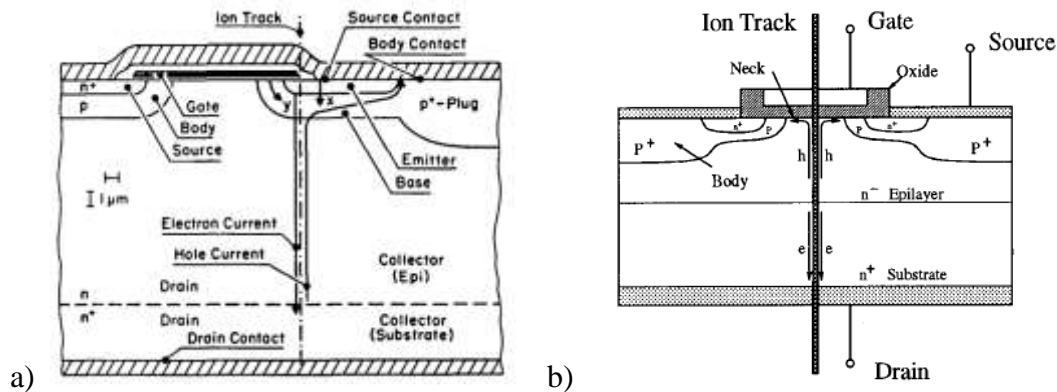


Figure 51: a) Model for SEB (92); b) and for SEGR (93).

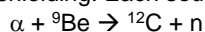
The microtomography technique requires appropriate tomographic methods, scanning geometries, photon energies and resolutions (94) (95), and it allows obtaining information on the internal structure of the sample and to investigate and characterise several features of interest. Taking that into consideration and with reference to the models of SEB and SEGR discussed above, a non-destructive investigation on Power MOSFETs went to a burnout event during accelerated tests with high-energy neutron has been performed. Methods and results are reported below.

4.1.2. Materials and methods

4.2.2.1. Materials

For the investigation two sets of Power MOSFETs (N-channel STP20N95K5, STMicroelectronics) have been investigated. The first set of 7 devices underwent to an accelerated test in the Neutron Irradiator facility of the DEIM department of the University of Palermo. The neutron irradiator consists of 4 ^{241}Am -Be sources that provide neutron in the energy range from thermal up to about 12 MeV¹. The purpose of the experiment is to verify the

¹ Accelerated tests were performed in the Am-Be facility of DEIIMM-University of Palermo. Such facility is made up 4 Am-Be sources, located on the bottom of water pool, in order to obtain an adequate level of radiation shielding. Each source can supply neutrons by the following reaction:



with alpha particles resulting from the natural decay of Am. The “native” spectrum has an energy range between few KeV and 12 MeV with a flux peak around 5 MeV. These sources are placed at the corners of a 20-cm square. At the center of this square there is a vertical tube used as a sample holder with an inner diameter of 25 mm, a length of 1 m and a water tight closure at the lower end. Therefore, neutrons emitted by the sources must cross a thickness of about 14 cm of water before

device reliability over a time period, equivalent to 20 years of terrestrial neutrons exposure. The devices have been irradiated with Gate and Source at ground and Drain at growing voltage. The voltage has been enhanced progressively until the burnout has occurred (96). The second set of 8 fresh devices has been investigated to obtain comparative results (See Figure 52).

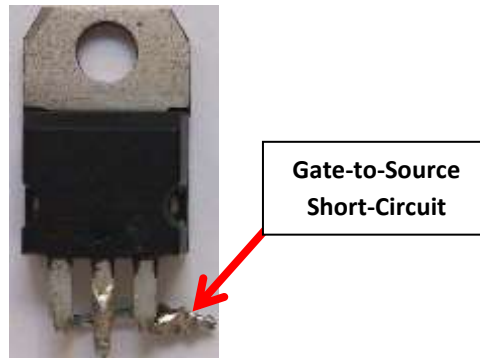


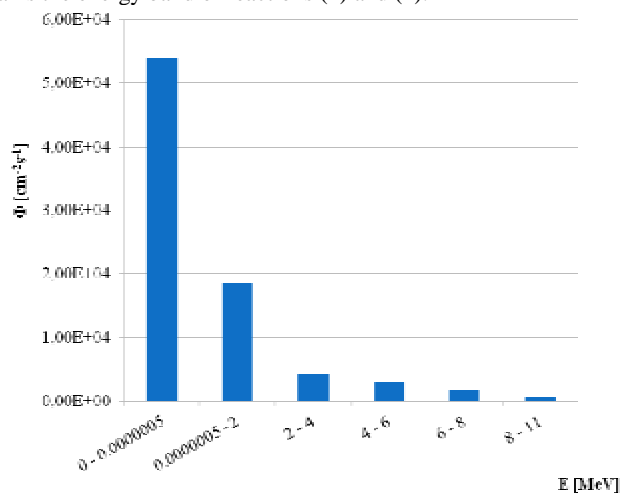
Figure 52: Detail of neutron irradiate Power MOSFET

4.2.2.2. Methods

4.1.2.2.1. Scanning electron microscopy

Preliminary to the microtomographic scans performed at the previously described μ Tomo station, the MOSFET device was investigated by means of a Scanning Electron Microscopy

reaching the sample holder compartment, which is invested by 4 directions to ensure a uniformity of irradiance that was estimated to be better than 3% in the experimental volume where the devices are placed. In fig. is depicted the simulated energy spectrum, which contains the energy band of reactions (1) and (2).



(SEM) equipped with an X-ray fluorescence detector to determine the dimensions and the typical composition of the used materials (97). A sample preparation was necessary in order to de-capsulate the external package of Power MOSFET employing a heat source to remove the plastic enclosure and, thereafter, a diluted hydrochloric acid (60%) solution to remove the metallic base.

The acquisition of micrographic images was obtained by a 15 keV electron beam in High Vacuum conditions. This allowed us to determine the elements present at the interfaces of the power MOSFET device, and to obtain topographical features, morphology and phase distribution (98). Figure 53 shows the SEM image the interfacial feature located between Si wafer and the heatsink. In Figure 53(a), a cross indicates the point of interest where the X-ray emission spectrum shown in (b) was acquired. The spectrum allows to determine the chemical composition of the probed area that, in this case, resulted to be almost pure Pb. This element is used as an adhesive layer between the heatsink and the Si wafer. Figure 54 shows the SEM image of the metal heatsink whose composition was identified by analysis of the X-ray emission spectrum induced in the point (+) and resulted principally composed by Ni. Similarly, an analysis was performed on the Si wafer (Figure 55) and on the external package (Figure 56). The latter resulted to be principally composite of C.

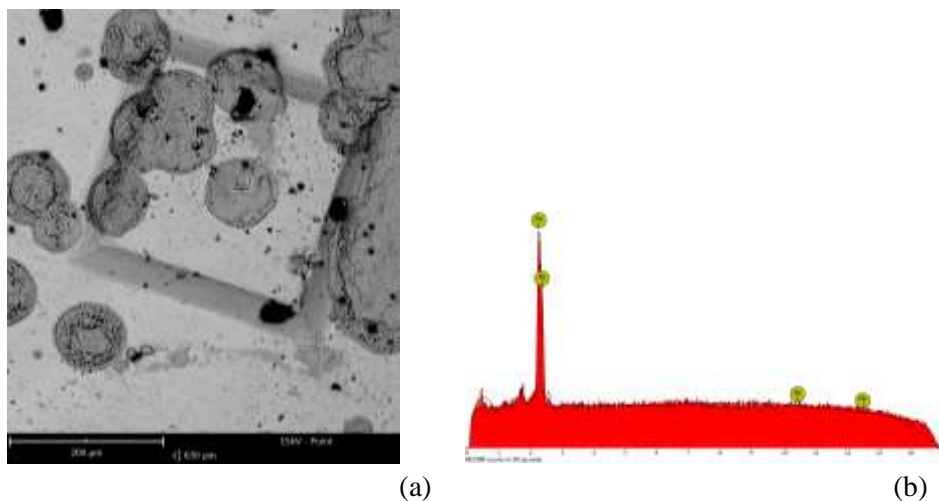
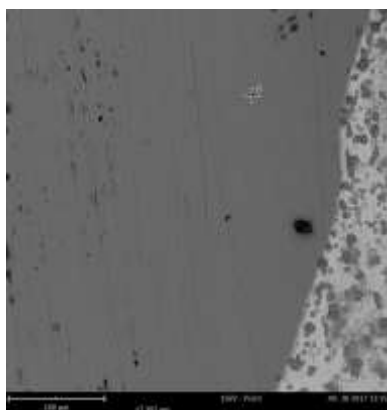
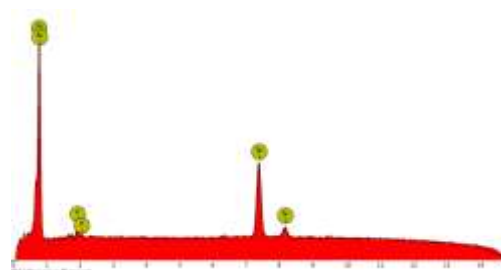


Figure 53: SEM single device – Power MOSFET

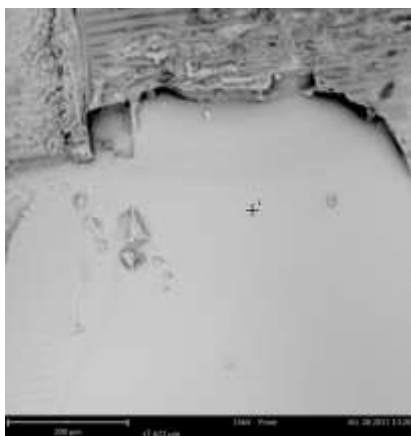


(a)



(b)

Figure 54: SEM of metal heatsink

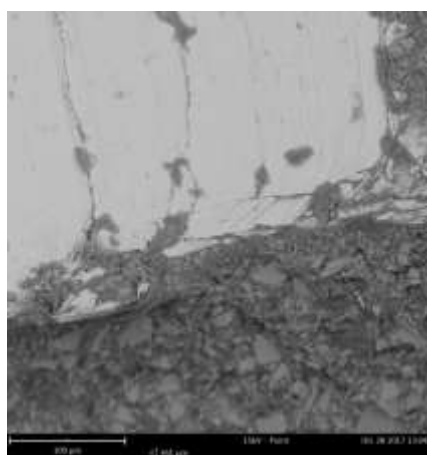


(a)

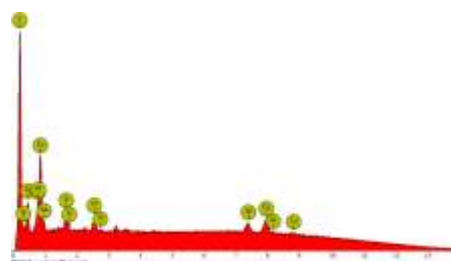


(b)

Figure 55: SEM of Si substrate



(a)



(b)

Figure 56: SEM of external package

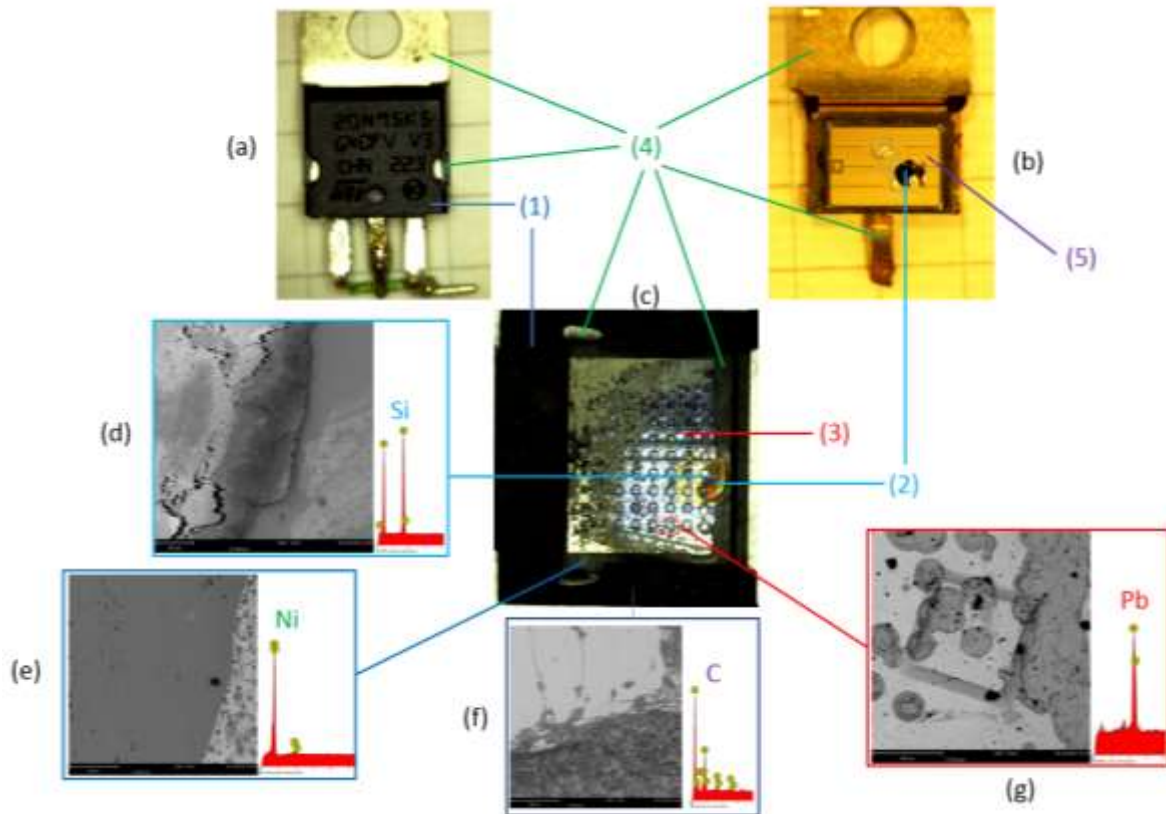


Figure 57: Overall schematic representation of the SEM analysis

Figure 57 resumes the SEM analysis results: The Power MOSFET (a) after the removal of the polymeric cap is reported in (b) where the structure of the gate and source electrodes is evident. On the opposite side, the 9x8 matrix of the hollows in the Si wafer (c) appears after the Ni backplate chemical removal. The (d-g) images show the SEM close-ups of the different components whose chemical analysis was obtained by EDS analysis in such a way that the parts were identified: polymeric external package (1), silicon wafer (2), Pb solder layer (3), Ni metallic drain electrode and heat-sink (4) and source/gate metallic contacts (5).

4.1.2.2.2. Microtomography

The destructive analysis techniques such as physical cross sectioning and chemical decapsulation may induce damage or remove the evidence of a defect or damage site. The 3D X-ray micro computed tomography provides a powerful non-invasive alternative solution for failure analysis (99).

Prior to microtomographic data acquisition, it is necessary to align the source, the specimen and the detector. This consists of placing the specimen within the FOV (field of view) making individual acquisition at 0 and 180 degrees and verifying the correct rotation of the specimen about its vertical axis. In addition, the user should set the magnification of the system considering the focal spot, the pixel size and the detector area. Furthermore, the beam energy was chosen for obtaining the best contrast.

Each Power MOSFET was placed in a suitable sample holder and, by considering the sample dimensions as well as those of the area of interest (internal package), a magnification 6 was determined and small spot size operation mode was set. The X-ray source parameters (current, focus, voltage) and the exposure time were successively set to get at least a 15 percent of photon transmission in the area of interest.

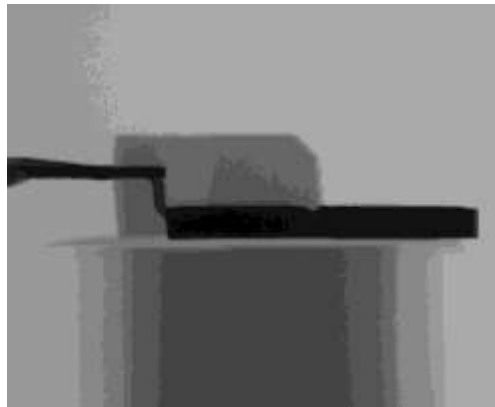
A further step is the motors calibration and the setting of the data storage. Finally, the acquisition procedure includes the acquisition of the dark- and flat-images both previous and after the sample scanning.

The 2D reconstruction was obtained by using the NRecon software (free-ware version). The standard reconstruction parameters were: 'smoothing factor' = 4, 'beam hardening correction' = 10 % and 'ring artefact reduction' = 10.

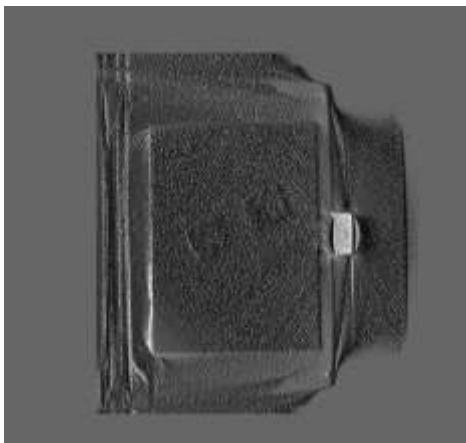
Two alternative axes of rotation were considered to get the best resolution and contrast:

Horizontal sample: The sample was placed laying on the heatsink, the source parameters were $V=150\text{kV}$, $I=66\mu\text{A}$, $t_{\text{exp}}=1200\text{ ms}$, 0.1° rotation step (3600 images acquisition), magnification = 6. The reconstructed image of the MOSFET shows a very poor contrast due to the thickness

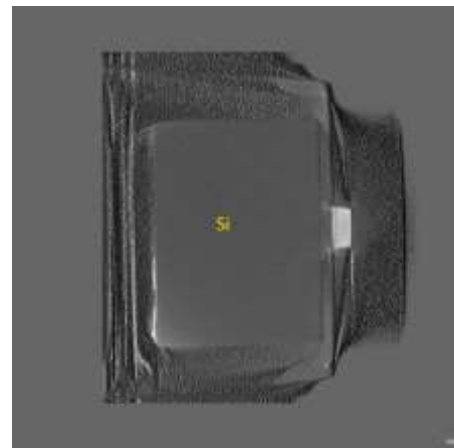
of the absorbent materials. Figure 58 shows the 3D reconstruction of the Power MOSFET in these conditions: (a) X-ray radiography showing the projection of sample on the detector; (b) virtual horizontal cut where the details of Si-wafer external clamping to the external package are discernible; (c) horizontal cut through the Si-layer showing a flat section that does not give any evidence of details or defect.



(a)



(b)



(c)

Figure 58: 3D Power MOSFET result of horizontal position in the scan on the sample holder

Vertical sample: The scan was performed by placing the sample in vertical position, i.e. with the rotational axis parallel to the heatsink. Acquisition parameters were $V=150\text{kV}$, $I=66\mu\text{A}$,

$t_{exp}=1500$ ms, 0.2° rotation step (1800 steps), magnification=7. The reconstructed images show finer details if compared to the “Horizontal scan” due to the lower extent of the absorbent materials to be crossed (the polymeric package and the Ni heatsink plate). This allows to show the internal details of interest into Si substrate. Figure 59 depicts the radiographic projection, which shows the position of sample while Figure 60 shows the package internal structure in terms of orthogonal views.

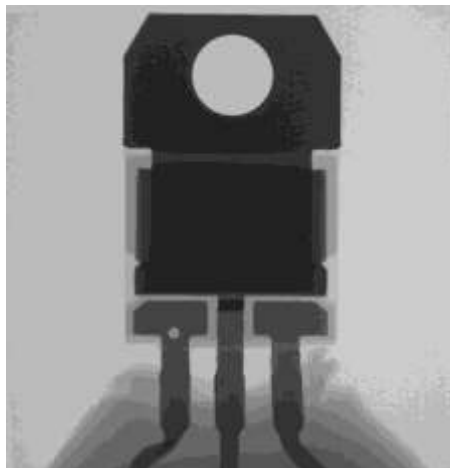


Figure 59: Vertical scan – Power MOSFET

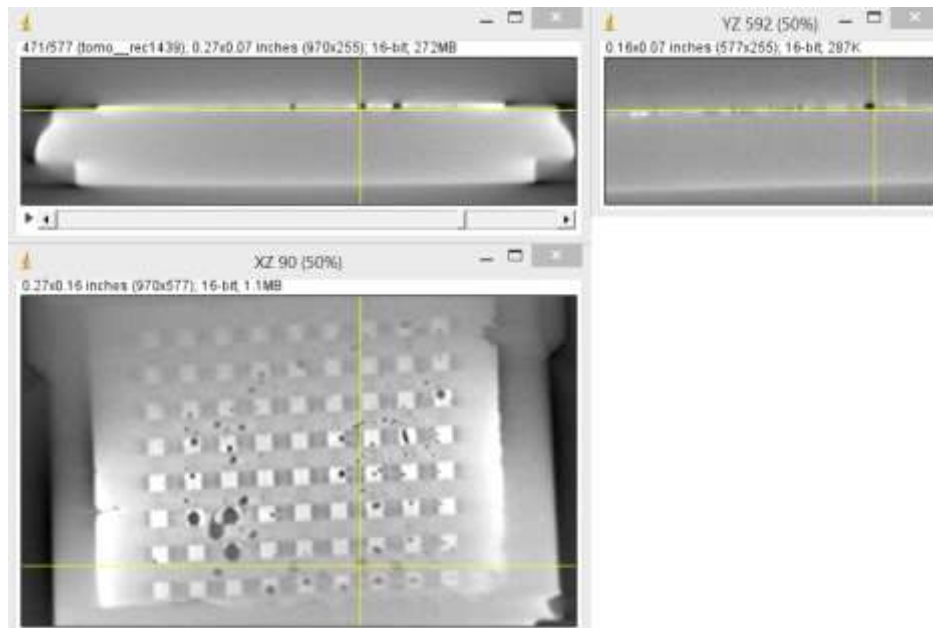


Figure 60: Orthogonal cut of the reconstructed MOSFET 3D image by means of a “Vertical scan”.

As the details gained adopting the “Vertical scan” geometry was higher, we performed the following acquisition with this configuration. The generic acquisition parameters for the μ -CT experiments reported in the next pages are: $V=140$ kV, $I=71$ μ A, $t_{\text{exp}}=2000$ ms, 0.2° rotation step (1800 steps), magnification=6 with an effective pixel size equal to 8.33 μ m.

The horizontal cut through the interfacial region between Si and Ni heatsink, allowed to determine the distribution of the Pb adhesive layer (see Figure 60). This is shaped in a 9(h) x 8(v) matrix of square platelets with a 340 μ m side and 115 μ m thickness. Each platelet is placed below a MOSFET unit in the device allowing both a high thermal and electrical conduction. In the interstitial sites, a thinner layer of Pb is present whose thickness is varying between 10 to 20 μ m.

4.2.2.3. MOSFET structure and SEE

Figure 61(a) depicts the structure of Power MOSFET N-channel STP20N95K5 with MDmesh K5 technology according to the technical datasheets and the theoretical models and in agreement with our μ -CT results. As already noted, the μ -CT permitted to put into evidence the dimensions of lead solder tab and bulk of silicon, however the μ -CT gives no evidence of the different dopant regions inside the silicon bulk as well of the gate and source features. On the Figure 61(b), right panel, we show a vertical cut along the region of interest described on the left panel where a SEE took place (compare the left image with the region enclosed in a dotted rectangle). The drain Ni backplate (layer 1) is located below a Pb solder (layer 2). The silicon epitaxial surface, region 4, is placed between the external polymeric package (5) and the drain metal backplate. Evidence of a SEE is given by the protrusion in a dashed circle (3) into the silicon layer.

In the following, we report the analysis of different samples showing the first (SEB) or second case (SEGR) of SEE as compared with pristine samples.

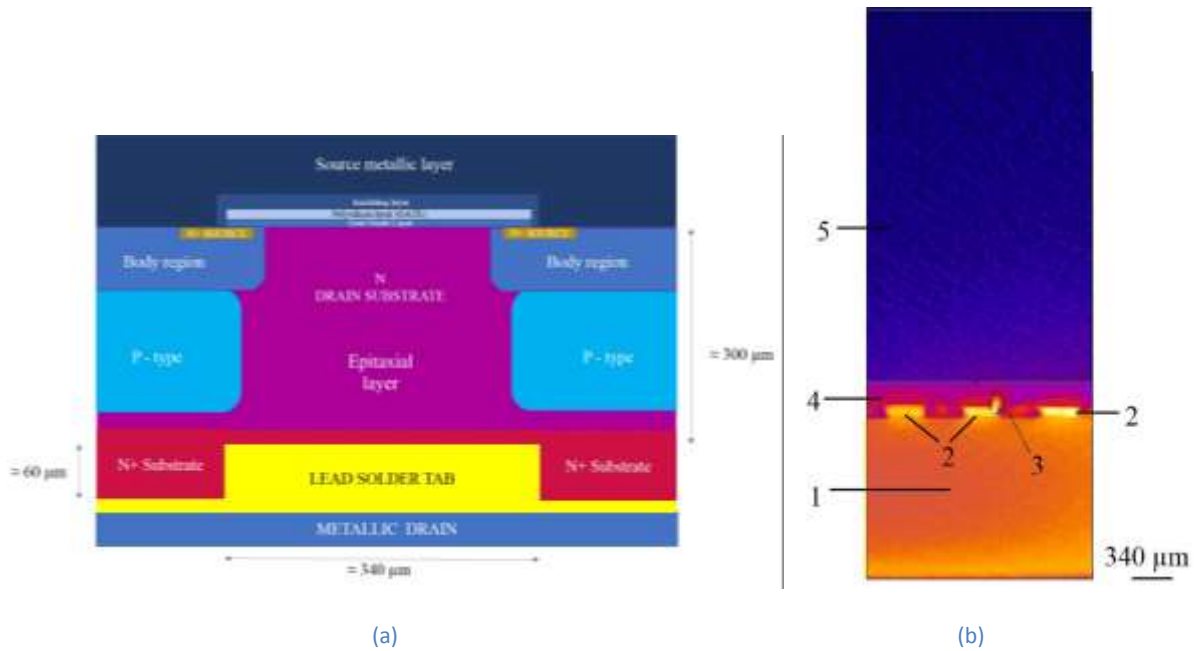


Figure 61: MDmesh Power MOSFET Structure

4.2.2.4. Pristine MOSFET results

The following data are collected from 8 different power MOSFET before the neutron irradiation procedure. All the sampled MOSFETs show similar structures: a common defect in the Pb layer where a series of voids are trapped and some highly adsorbing particles (probably Pb or Cu) placed into the packing.

MOSFET No. 1

The internal structure of the first sample could be recovered by a volume cut of the reconstructed 3D image. Are reported in Figure 62, the layered structure of the MOSFET #1 is recovered.

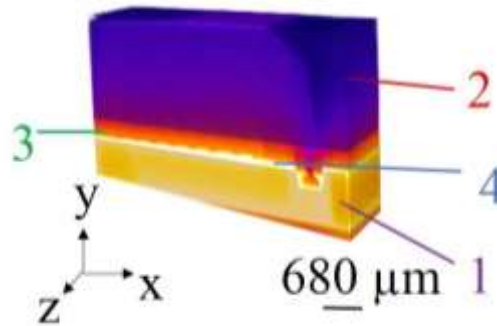


Figure 62: Power MOSFET volume rendering: metallic drain (1), external package (2), silicon layer (3) and lead solder layer (4).

Apart from the presence of voids at in the Pb layer, already evidenced in Figure 63, there are no other evident defects.

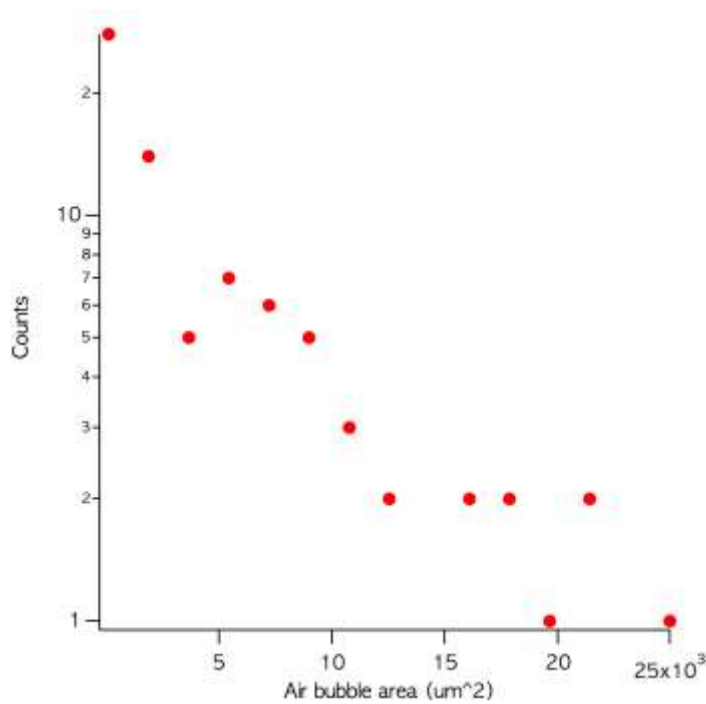


Figure 63: Histogram of the voids area in the Pb layer for the sample MOSFET #1.

The voids have a typical dimension ranging from few μm to 150 μm. While the typical total area occupied by them is between 1% and 2% of the Pb layer. It is important to note that larger

voids are trapped by the square tab hollow and thus they limit the heat and current transport from the Si layer to the Ni backplate in correspondence with the single devices hosted.

MOSFET No. 2

Figure 64 shows the orthogonal views and 3D rendering of the second sample. Also, in this case, it is possible to locate a series of voids at the Pb interface.

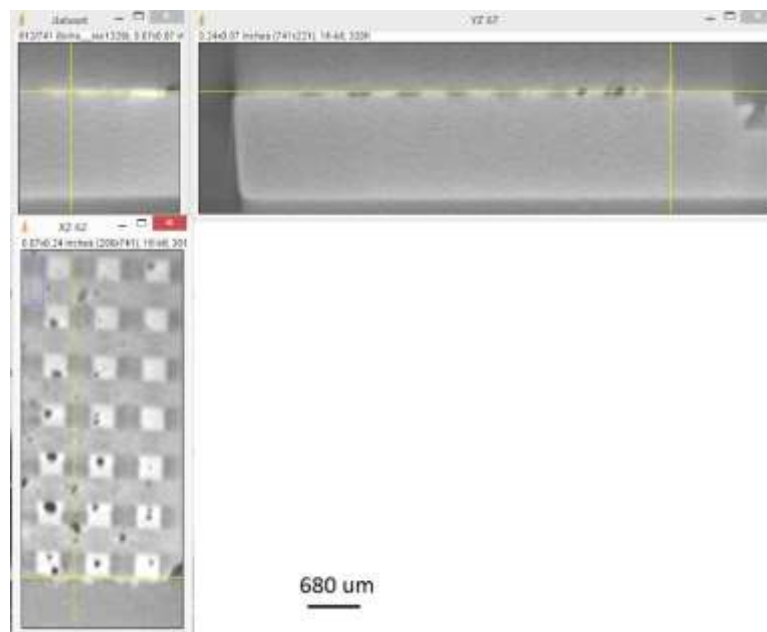


Figure 64: Zoom - Orthogonal View

MOSFET No. 3

Figures 65 - 68 show orthogonal cuts and 3D rendering of the ROI in MOSFET #3 showing a defect placed at the bottom edge of the package. Figure 68 depicts the position of the imaged defect (length 1: 34 μm ; length 2: 13 μm).

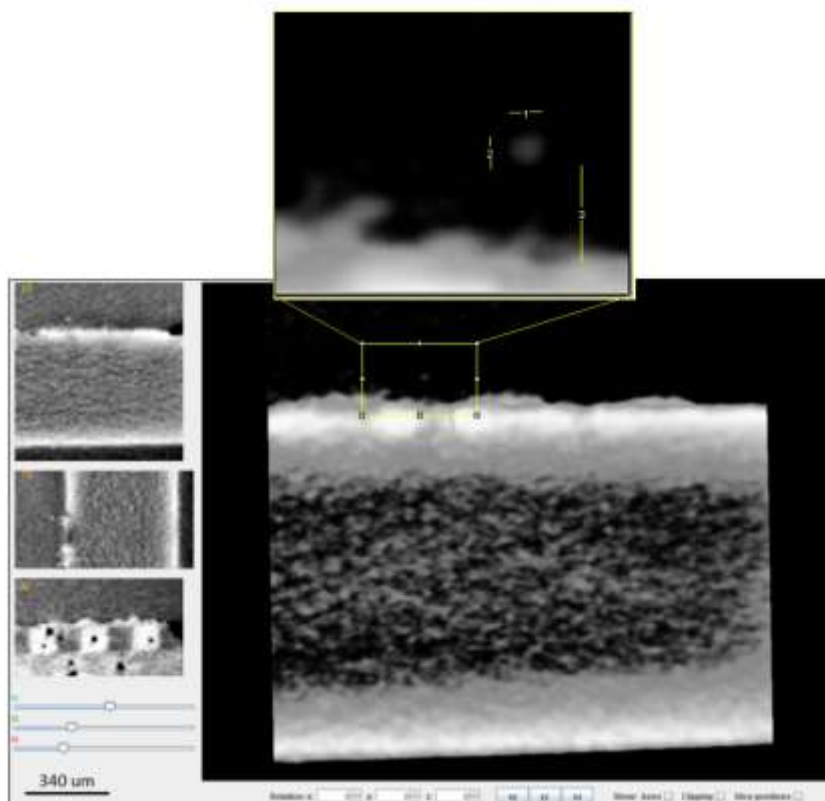


Figure 65: Zoom - Orthogonal View and 3D of ROI of interest

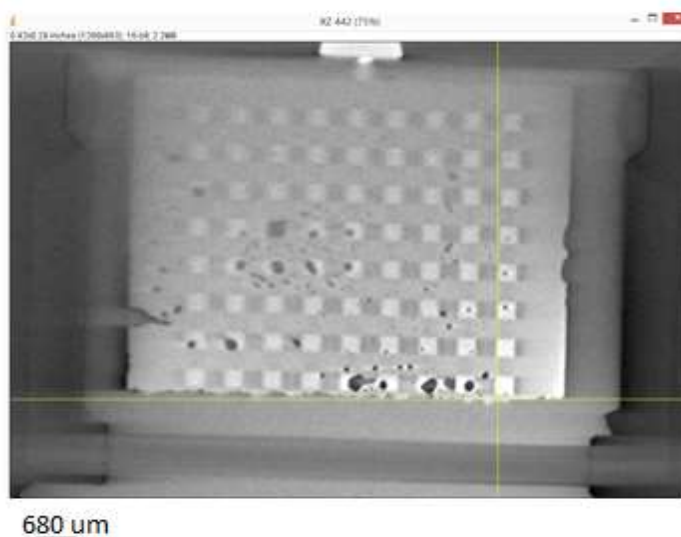


Figure 66: MOSFET #3 - XZ plane cut along the Pb layer

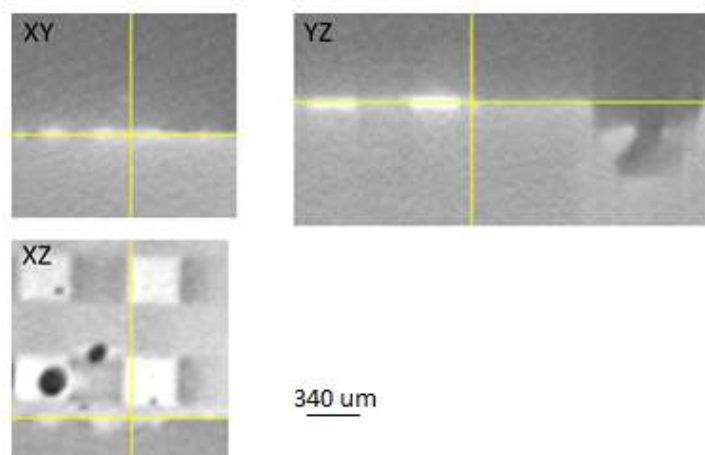


Figure 67: Zoom on the ROI (Orthogonal View)

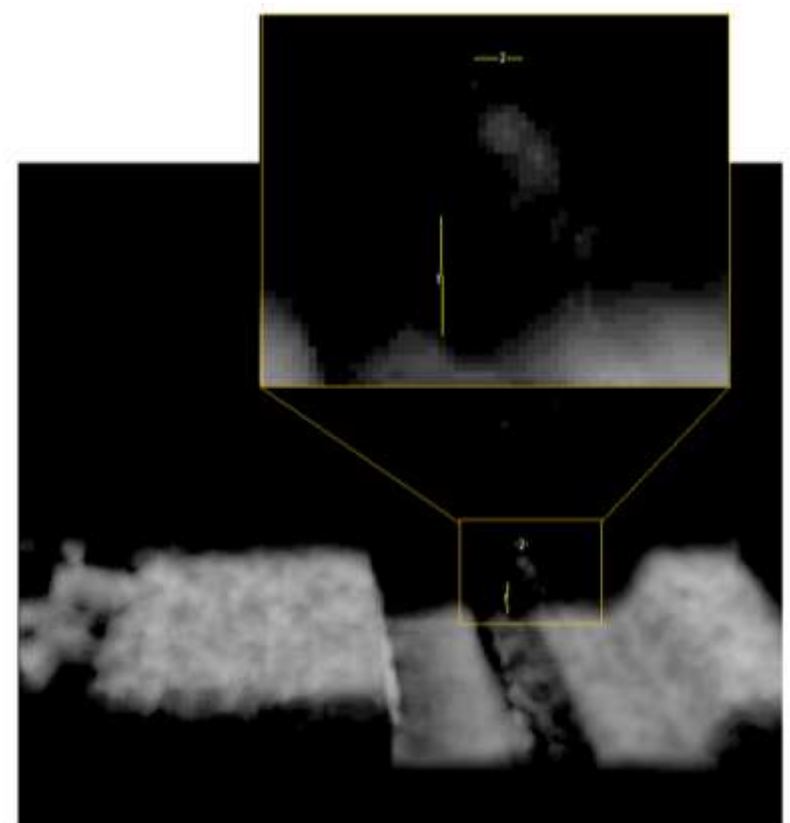


Figure 68: ROI Rendering 3D – Side view

MOSFET No. 4

In MOSFET #4 we found a defect into the package (see Figure 69) and a couple of defects placed close to the Si layer top (see Figures 70 - 72). In this second case, already noted for MOSFET #2, the defects are placed on the border of the Si layer.

Defect 1

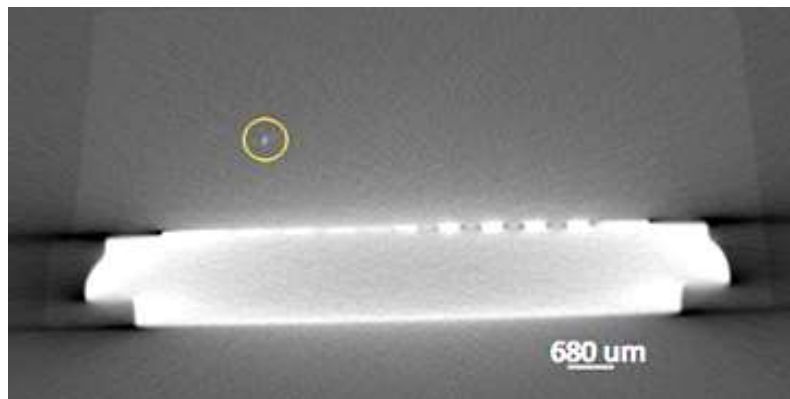


Figure 69: 2D Projection

Defect 2



Figure 70: 2D Projection

Defect 3

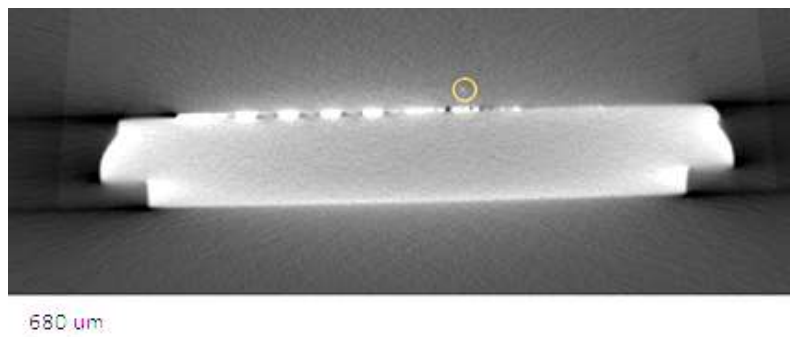


Figure 71: 2D Projection

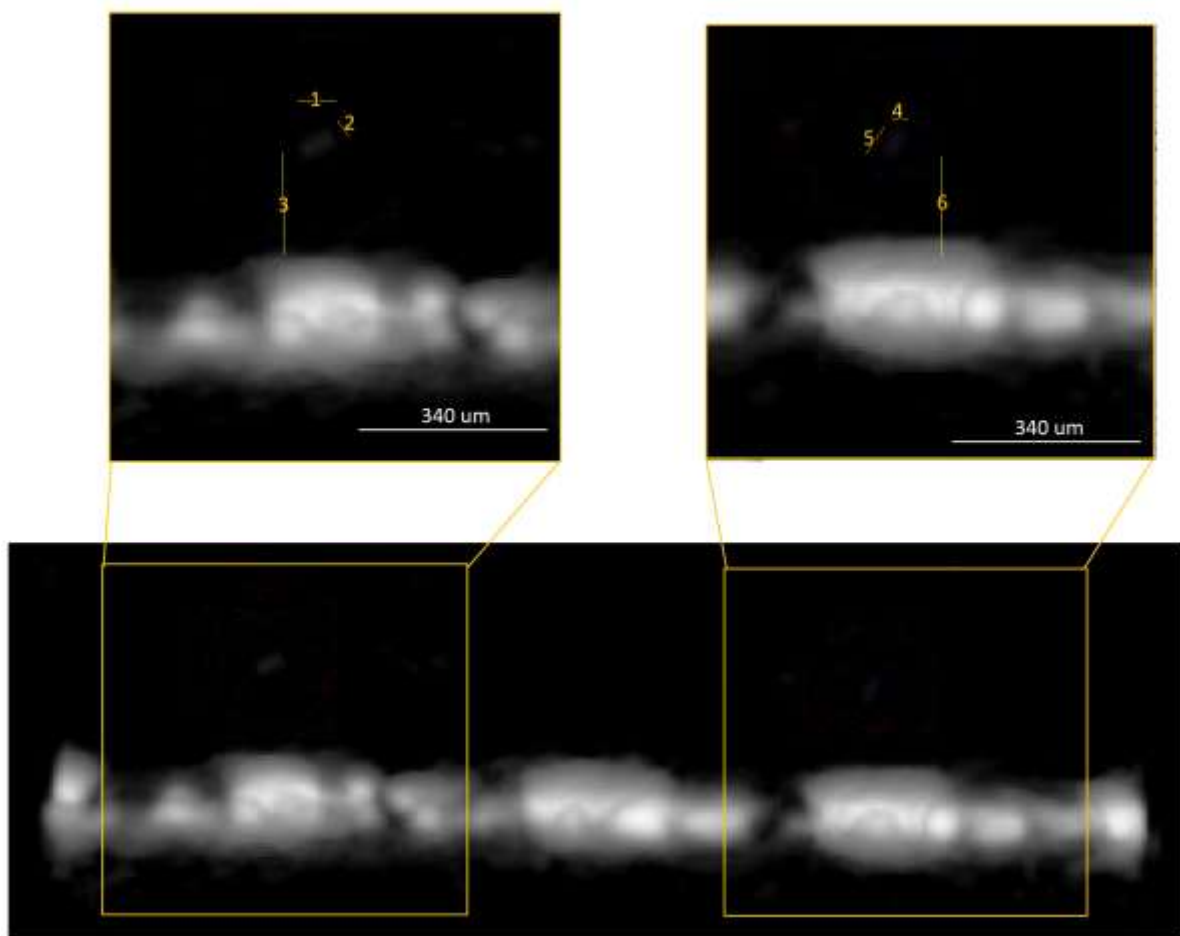


Figure 72: Side View and zoom view to 150% length 1: 71 μm , length 2: 33 μm , length 3: 187 μm , length 4: 27 μm , length 5: 60 μm , and length 6: 187 μm .

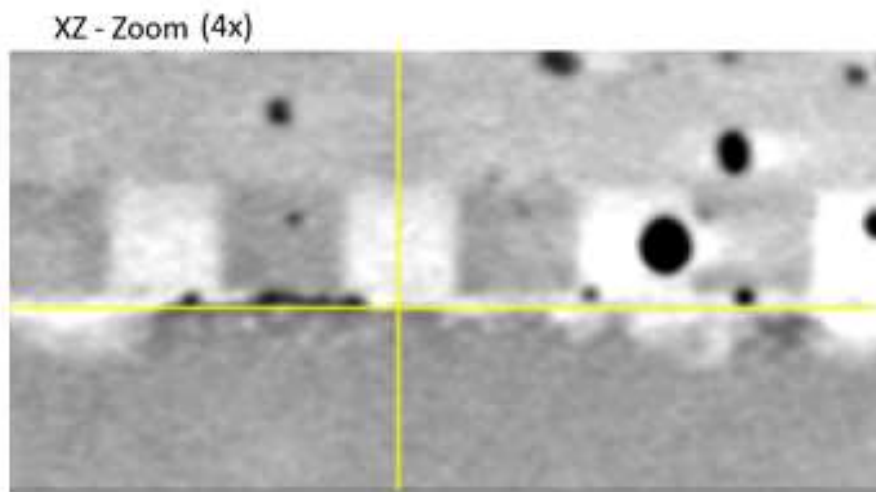
MOSFET No. 5

The defect is located out the border of the device in the lower right zone (See Figure 73 and 74). Figure 75 depicts the dimensions of defect into Si, length 1: 61 μm , length 2: 52 μm and length 3: 83 μm



680 μm

Figure 73: 2D Projection



340 μm

Figure 74: ROI Rendering 3D – Top view

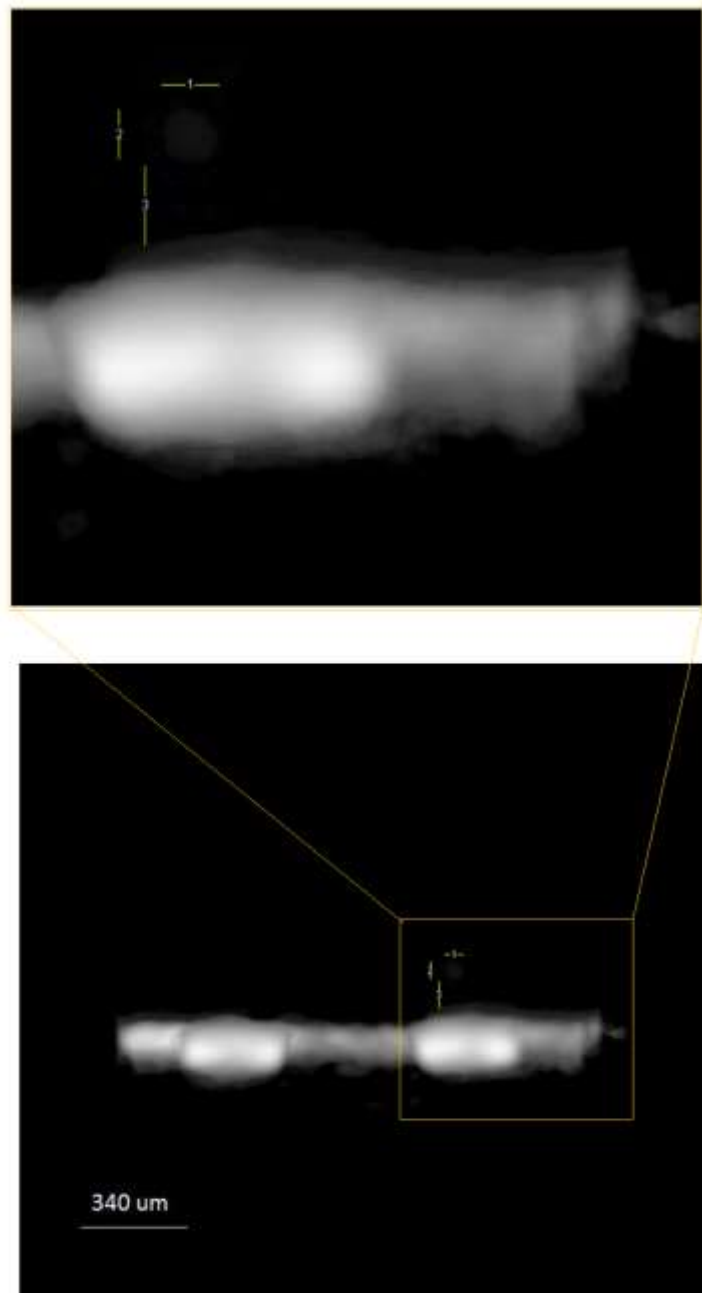


Figure 75: 3D - Side View and 300% 3D Zoom

MOSFET No. 6

This Power MOSFET does not show any detectable defect.

MOSFET No. 7

A defect like those pinned in the MOSFETS #2 and #4 is present also in this device. This defect is located out of the border of the silicon layer in the lower right zone (See Figures 76-79).

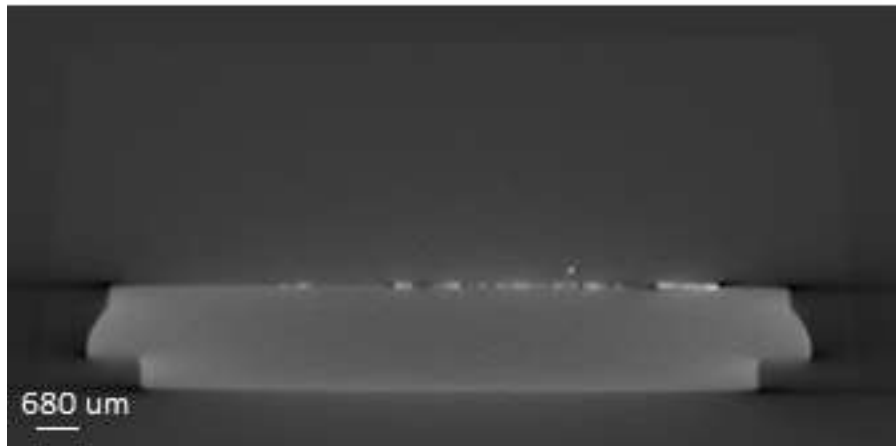
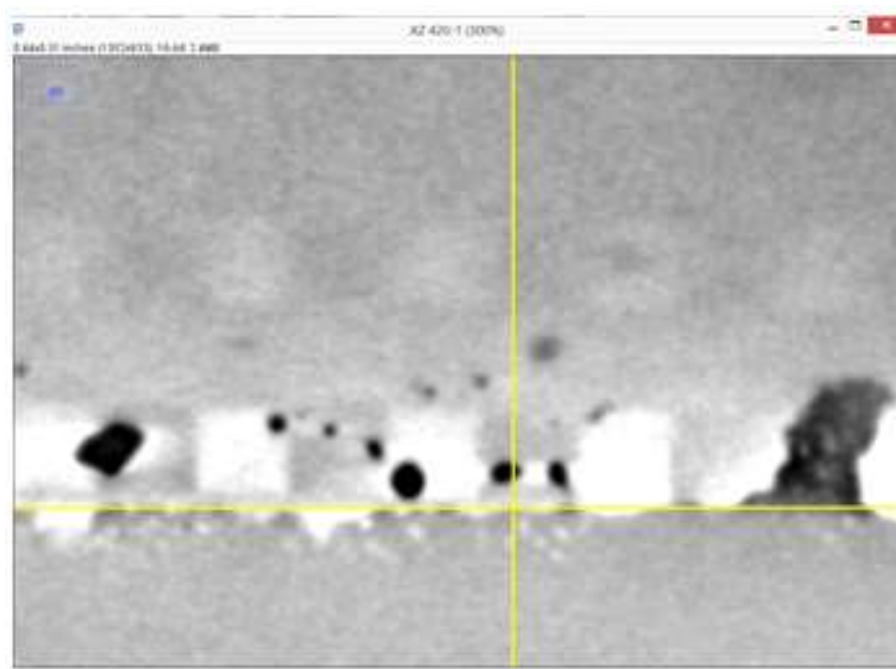


Figure 76: 2D Projection



340 μm

Figure 77: Zoom XZ view

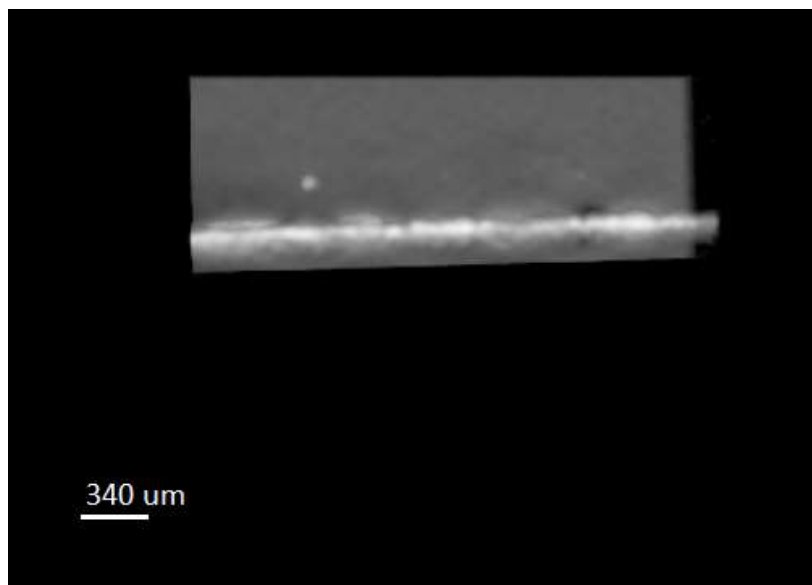


Figure 78: 3D – Side -view

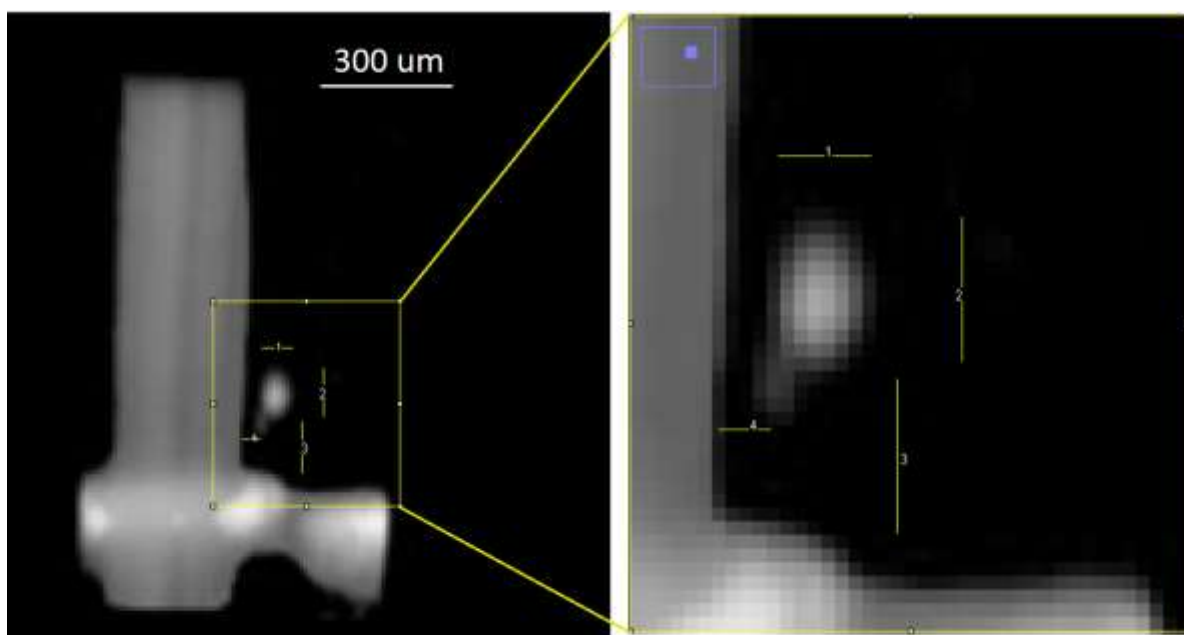


Figure 79: 3D - Side view and 1200% zoom view. length 1: 70 μm, length 2: 108 μm, length 3: 116 μm and length 4: 39 μm

MOSFET No. 8

This Power MOFET does not show any detectable defect.

4.2.2.5. n-irradiated MOSFET results - Case 1: Single-Event Burnout (SEB)

In this section we will show the micro-CT results on the n-irradiated sample which developed a Single Event Effect. According to the position of the defect, the SEE was ascribed to a Single Event Burnout (SEB). As a matter of fact, the following samples show the presence of defects placed on the border of the single MOSFET device hosted by the Si wafer. In this position, according to the MOSFET datasheet, the detected defects are placed in between the drain electrode and the source where the SEB takes place according to above reported model. The defects are evidenced by the presence of Pb volumes whose height ranged from few μm tens to the whole silicon wafer thickness. The analysis is simplified by the fact that the intensity Pb absorption signal is higher of the remaining elements allowing an easy segmentation of its signal.

MOSFET No. 1

A peculiar defect was recorded on this device as it was not classified as those reported in the previous section, i.e. those resulted from the production process. In the following μCT vertical cut, the Pb layer is clearly discernible on top of the Ni backplate. In correspondence of the second tab from the right, a protrusion towards the Si layer is present (See Figure 80).



Figure 80: 2D μCT cut of MOSFET #1 after n-irradiation

By having a closer look to this feature (see the top view in the next segmented reconstruction of the Pb layer), we can recognise that a Pb depletion zone is present on its foot (See Figure 81).

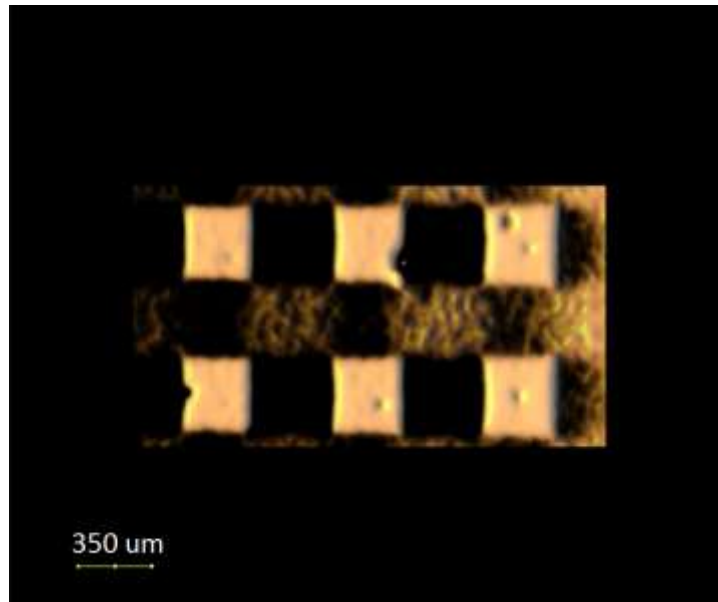


Figure 81: ROI Rendering 3D – Top view

A further magnification of the single tab allows measuring the dimension of the Pb protrusion that resulted 115 μm high and 60 μm wide (See Figure 82).

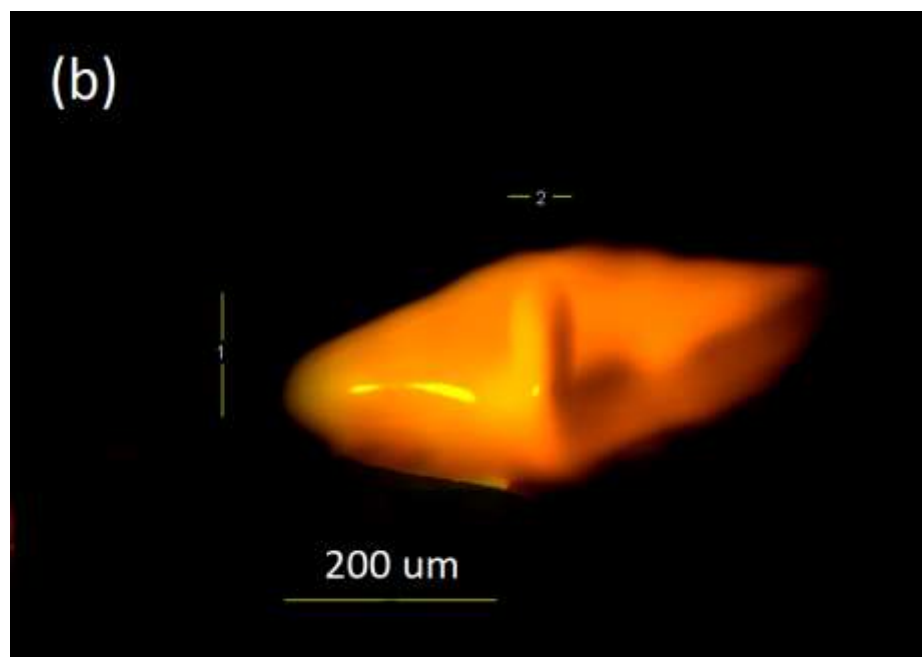
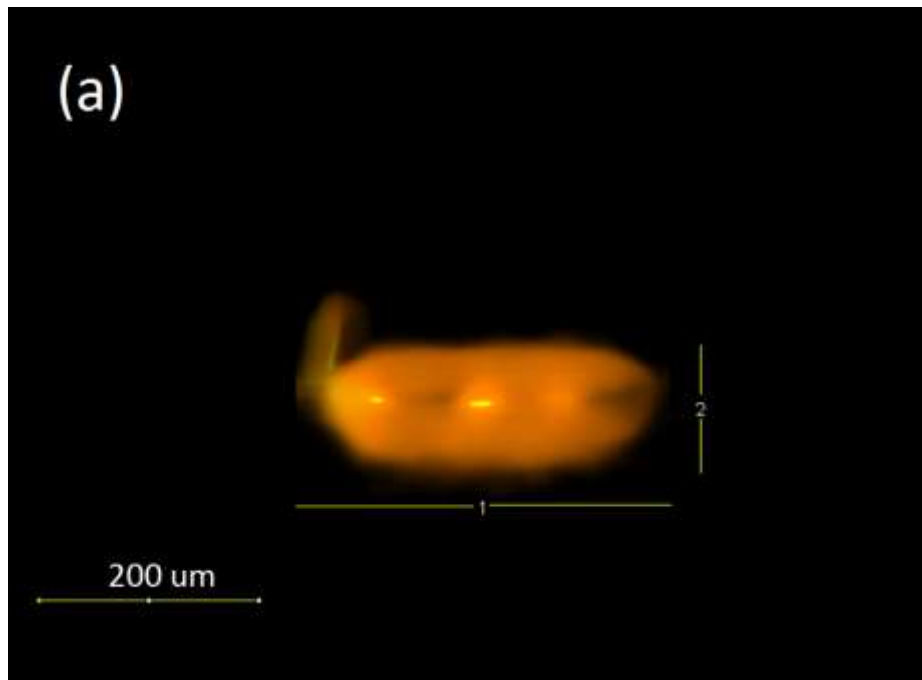


Figure 82: 3D Rendering: (a) side view (length 1: 340 μm and length 2: 114 μm) (b) Perspective view (length 1: 117 μm and length 2: 60 μm). The picture is obtained by a segmentation process extracting the Pb signal.

MOSFET No. 2

A defect like that reported for MOSFET #1 is present in this case. A Pb protrusion is present showing a Pb drop placed above the Si layer (at 300 μm from the solder layer). The following figures report the details of the defect detection (See Figures 83-85).

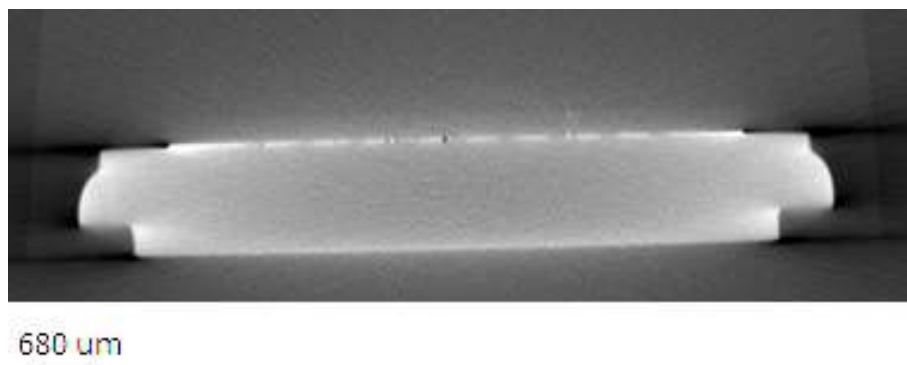


Figure 83: 2D μCT cut of MOSFET #2 after n-irradiation

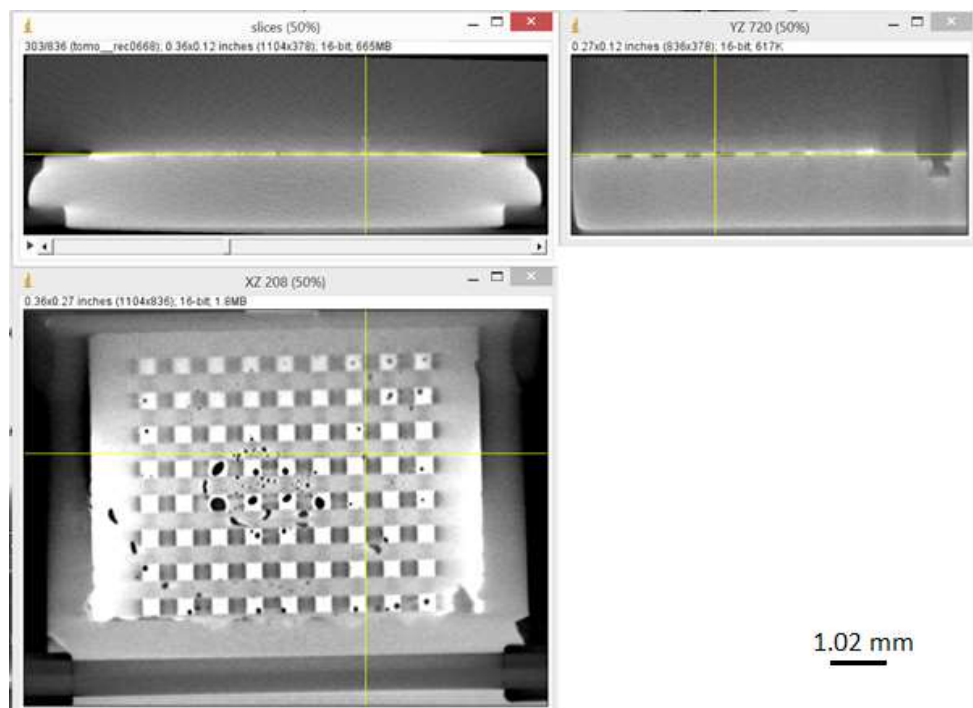


Figure 84: Orthogonal View and located of damage single device MOSFET #2

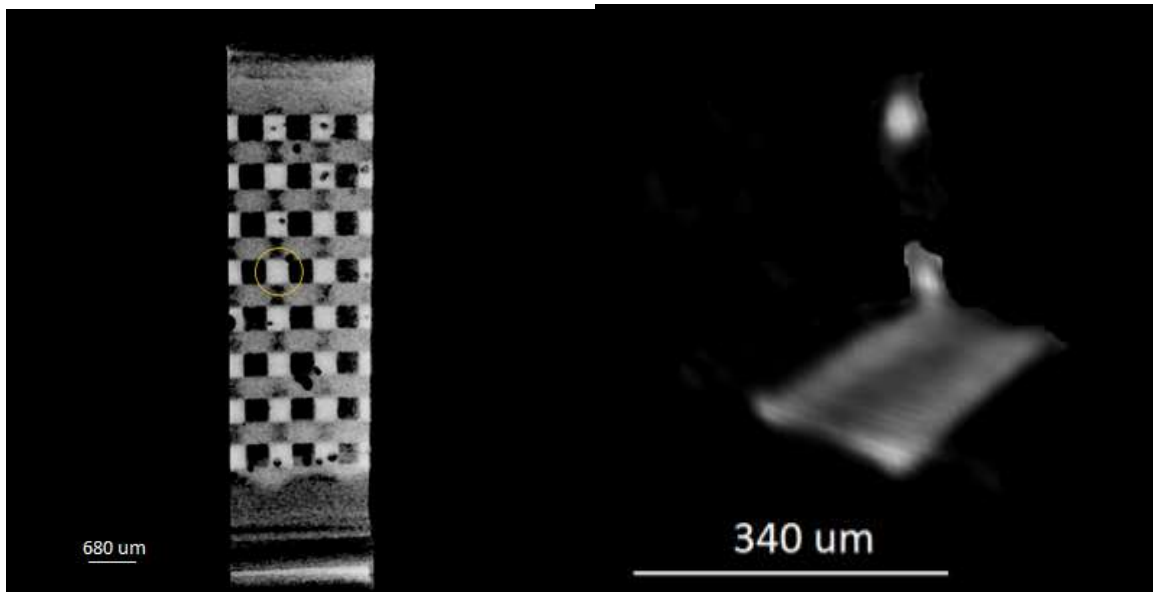


Figure 85: (a) ROI Rendering 3D – Top view; (b) Perspective view (The picture is obtained by a segmentation process extracting the Pb signal.)

Also, in this case, it was possible to determine the dimension of the Pb defect showing a thinner diameter of the feature (see Figure 86).

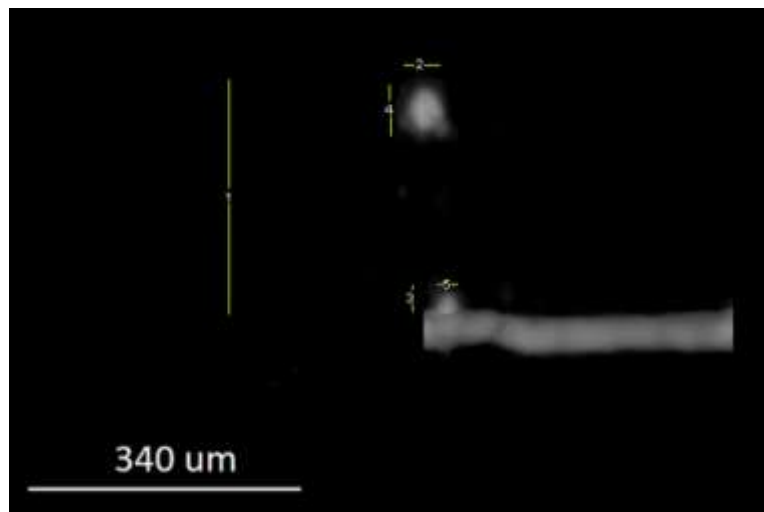


Figure 86: ROI Rendering 3D – Side view (length 1: 292 μm , length 2: 44 μm , length 3: 32 μm , length 4: 62 μm and length 5: 24 μm .)

MOSFET No. 3

The defect reported in the following images has a dendritic form as it starts from the Pb solder layer and develops toward the source electrode (See Figures 87-88).

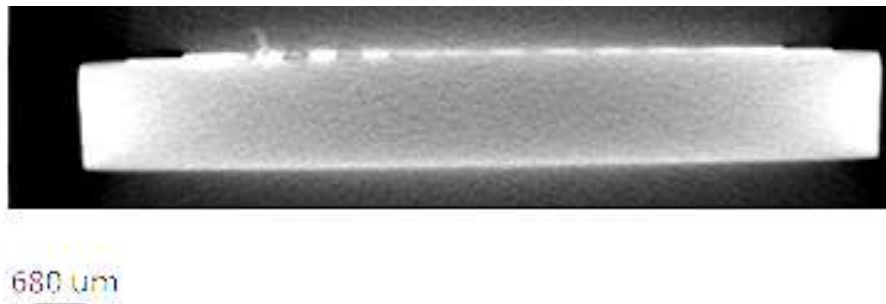


Figure 87: 2D μ CT cut of MOSFET #3 after n-irradiation

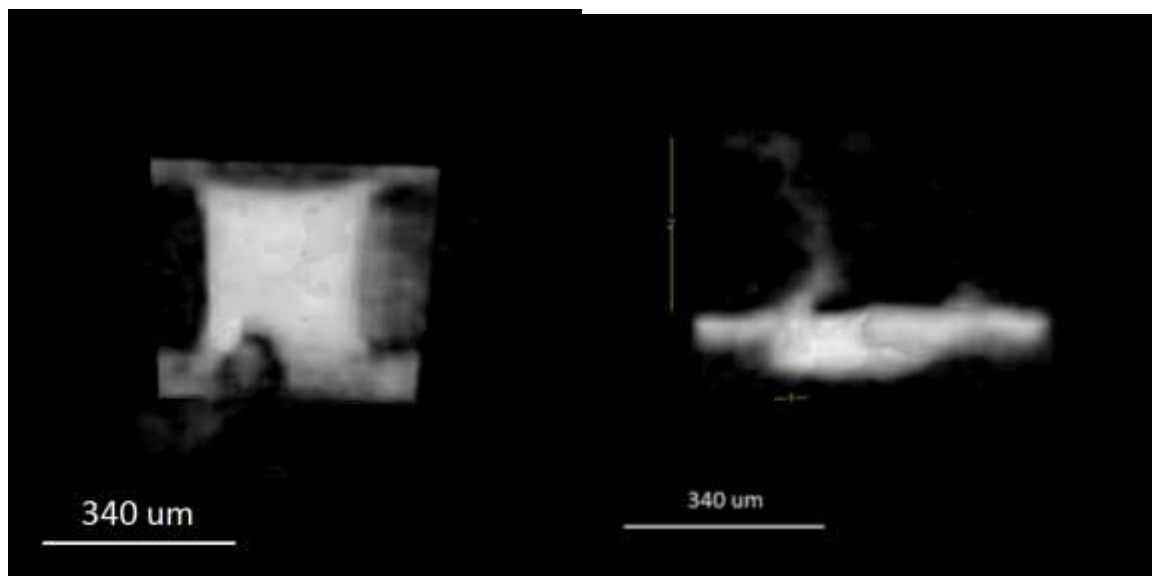
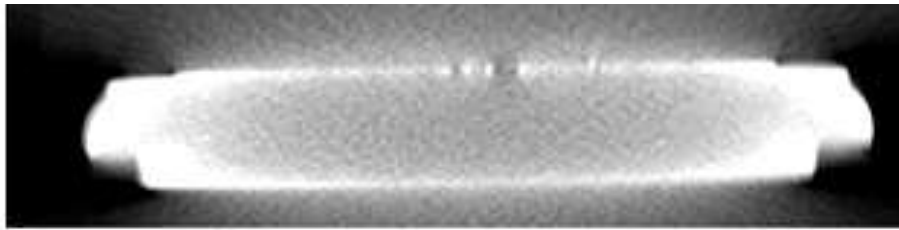


Figure 88: 3D Single Device ROI – Top view and Side view

MOSFET No. 4

The MOSFET #4 shows a n-induced defect in a peculiar position. As clearly recorded by the following pictures, the defect is bridging the source electrode and the drain one in between two single devices (See Figures 89 - 91).



680 μm

Figure 89: 2D μCT cut of MOSFET #4 after n-irradiation

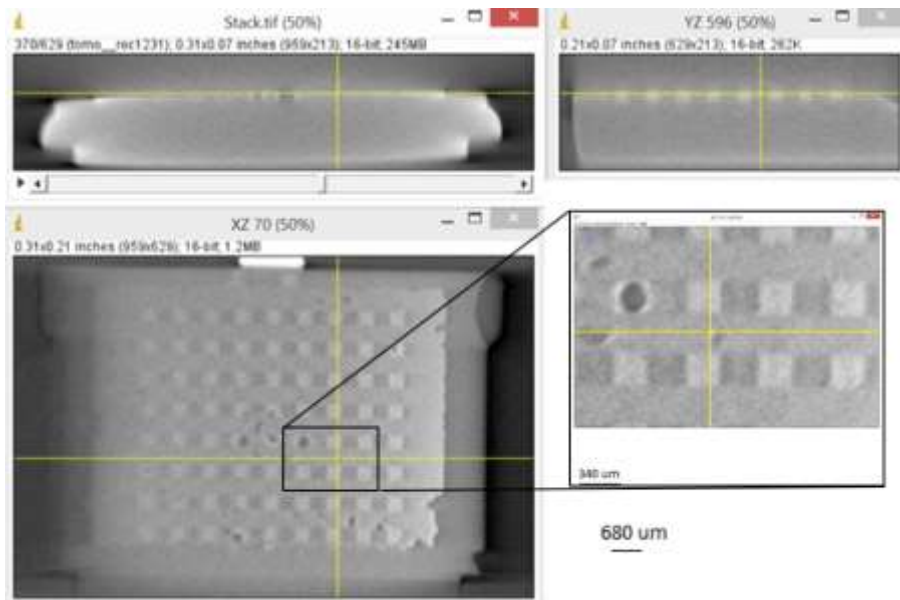


Figure 90: Orthogonal View across the ROI where the defects is in MOSFET#4 – The inset shows a zoom of ROI in XZ plane

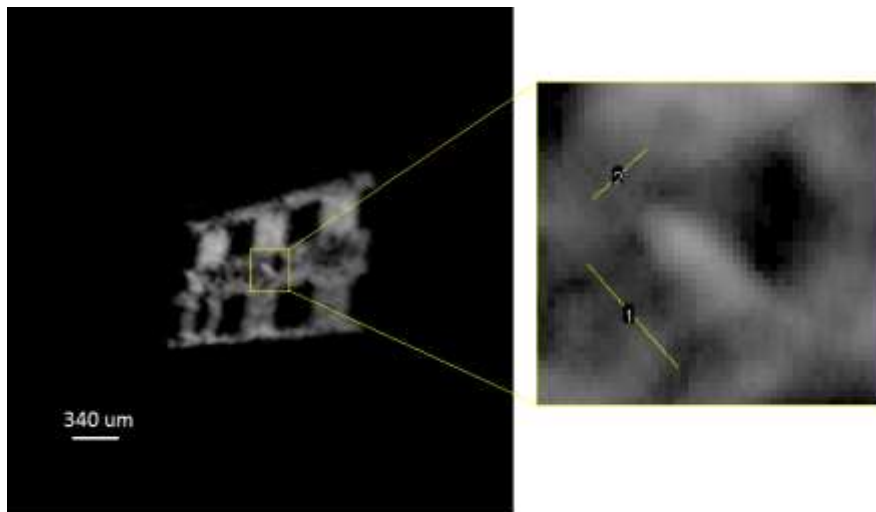


Figure 91: MOSFET #4 - 3D Rendering of the ROI: Perspective view. Length 1: 133 μm - length 2: 69 μm .

MOSFET No. 5

The neutron induced defects in MOSFET #5 have the typical behaviour already registered for samples #1 and #2 (see Images 92 - 94).

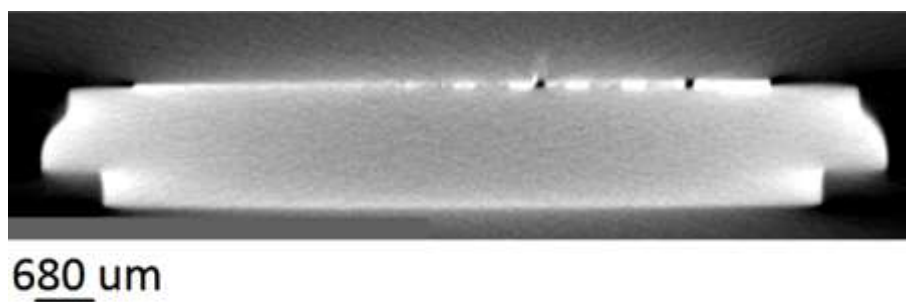
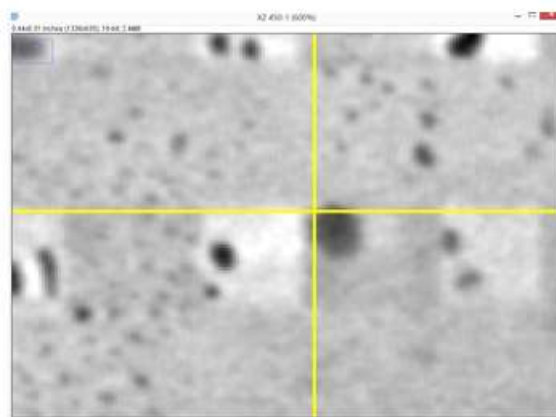


Figure 92: 2D μCT cut of MOSFET #5 after n-irradiation



340 μm

Figure 93: n-irradiated MOSFET #5 - Zoom XZ view of the ROI

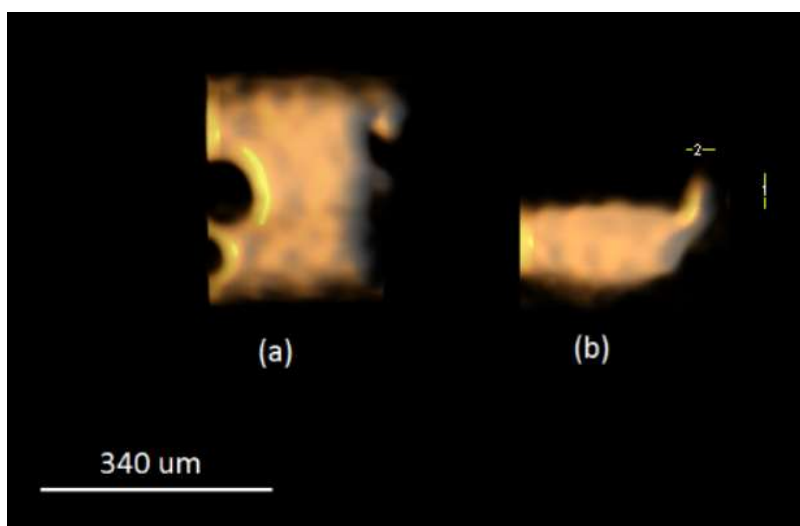


Figure 94: n-irradiated MOSFET #5 - 3D (a) Top view (b) Side view. Length 1= 51 μm – length 2= 39 μm . The picture is obtained by a segmentation process extracting the Pb signal.

4.2.2.6. n-irradiated MOSFET results - Case 2: Single-Event Gate Rupture

A second class of defects was recorded in 3 sampled power MOSFET. Here the SEE resulted in the formation of a Pb protrusion at the centre of the single device i.e. in the region connecting the gate electrode to the drain one. Thus, they are associated to the Single-Event Gate Rupture

(SEGR) occurrence. All the reported samples show a depletion of the Pb content at the base of the new formation.

MOSFET No. 6

MOSFET #6 after n-irradiation showed a defect centred on a Pb tab in correspondence with a single device. The following images report a close-up of it where it is evident both the extension of the damaged zone and its main features (see Figures 95 – 97).

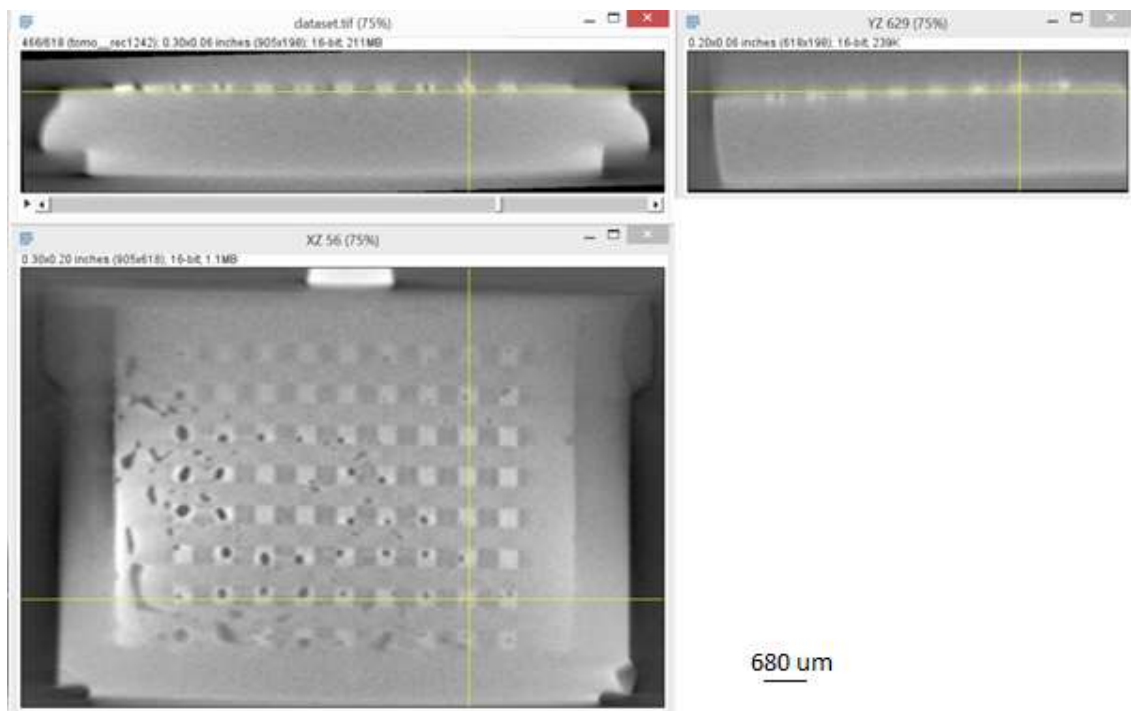


Figure 95: Orthogonal cuts of the 3D μ CT reconstruction. The planes intersect on the defected region.

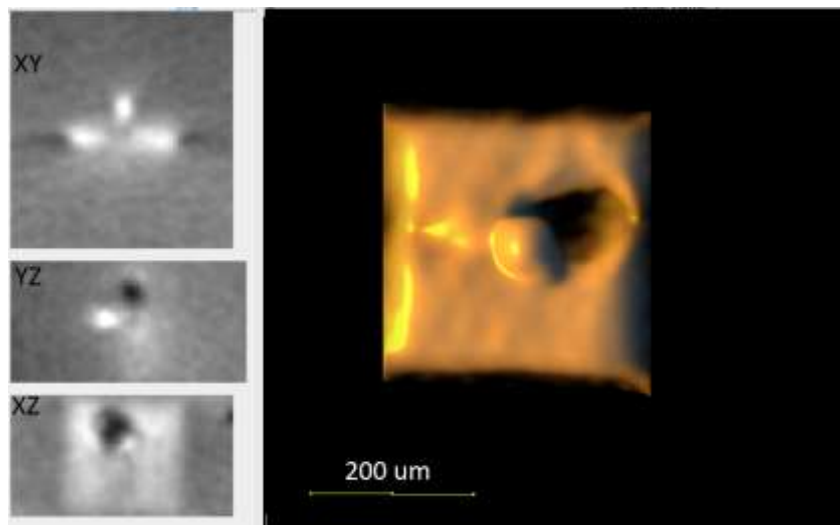


Figure 96: Zoom on the ROI- Orthogonal View and 3D of the Pb tab associated to a single device. The right picture is obtained by a segmentation process extracting the Pb signal.

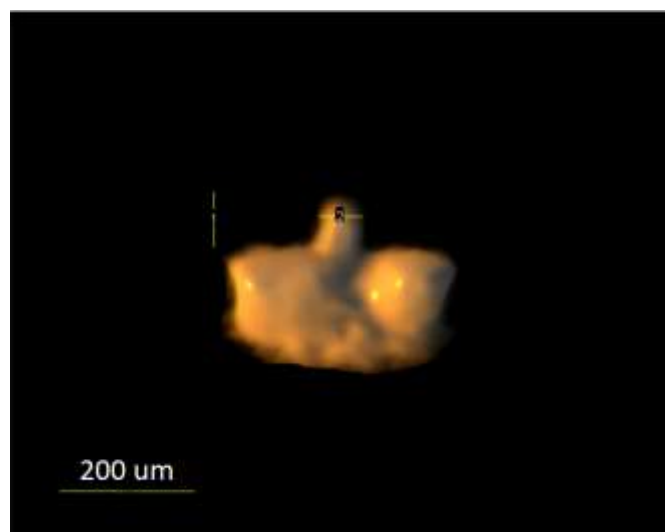


Figure 97: ROI 3D Rendering– Side view. Length 1: 83 μm - length 2: 62 μm . The picture is obtained by a segmentation process extracting the Pb signal.

MOSFET No. 7

A third example of SEGR event is evidenced by the following μCT images relative to MOSFET #7. The Pb signal reveals the presence of this element in a region between the gate electrode

and the drain. In correspondence, it is evident a depletion region in the Pb tab below the single device (see Figures 98 – 100).

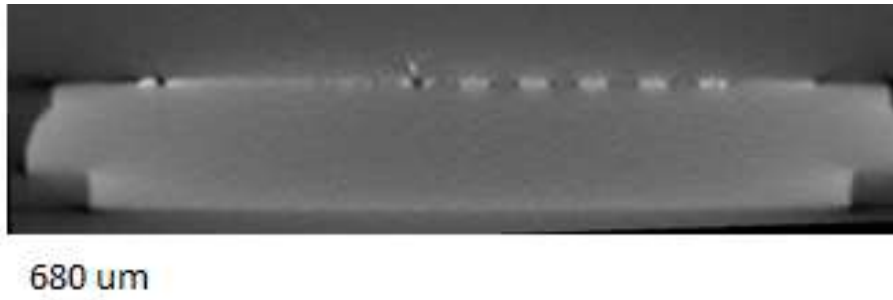


Figure 98: 2D μ CT cut of MOSFET #7 after n-irradiation

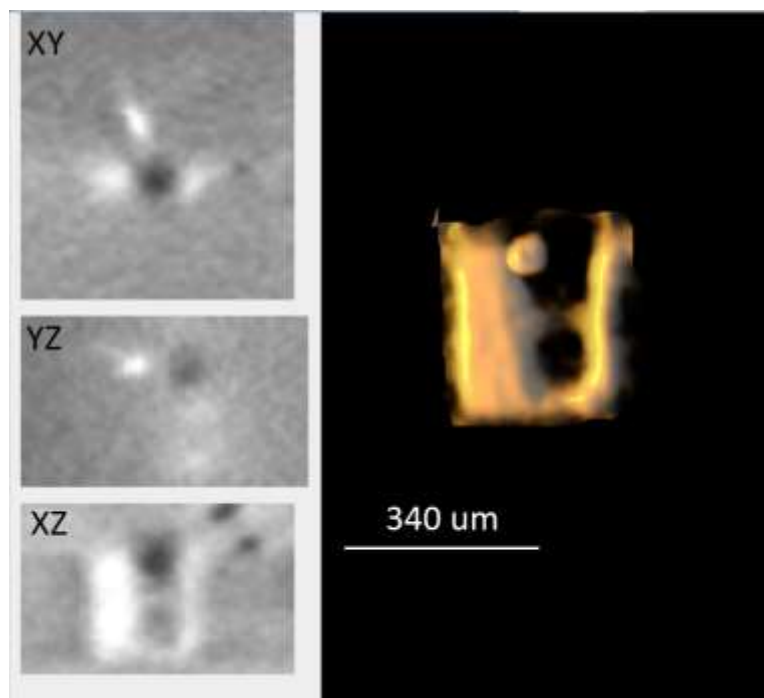


Figure 99: n-irradiated MOSFET #7 Zoom on the ROI - Orthogonal View and 3D of single device

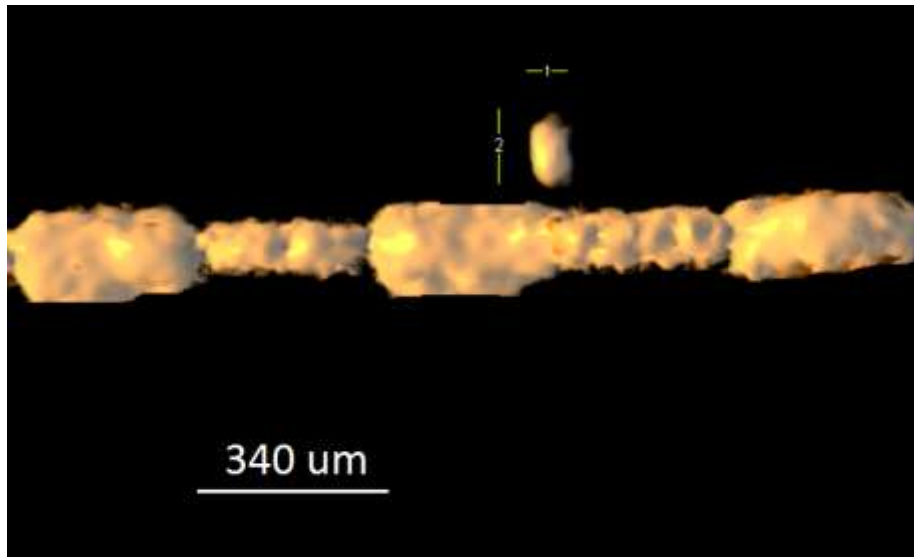


Figure 100: ROI Rendering 3D – Side view. Length 1: 54 μm – length 2: 135 μm .

4.2.2.7. SEE comparative study

The internal structure of a power MOSFET is recovered by means of μCT volume reconstruction. By using the vertical scan mode and with a magnification ranging between 6 and 7, we were able to depict the layered device with an optimal lateral resolution of 8 μm . In spite to the presence of elements with very different X-ray absorption coefficients (C, Si, Ni, Pb, ...) all the components were imaged (See Figure 101).

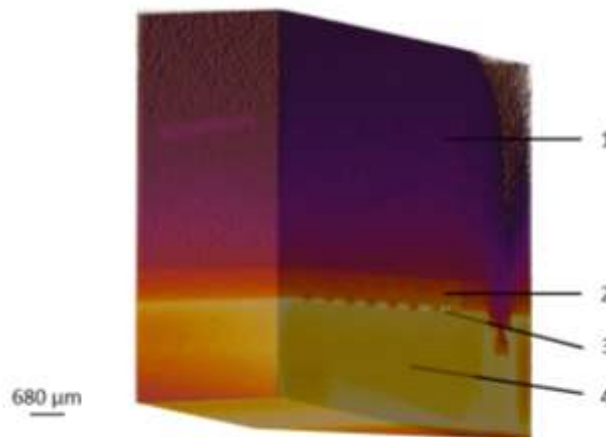


Figure 101: Typical reconstructed volume slab of the Power MOSFET evidencing the external package 1, the silicon layer 2, the Pb solder layer 3 and Ni metallic drain electrode 4.

As a first result, the presence of different defects in the pristine MOSFETs is evidenced by the μ CT inspection:

- a) air is trapped in the Pb solder layer with a preferential location in the Si hollows. The voids are probably consequence of the procedure of soldering the Si layer with the Ni back-plate;
- b) some Pb traces are found in different places aside and above the Si layer.

Concerning the neutron-irradiated samples the interpretation of the elaborated images is straightforward: the single-event effects result in the melting of a Si region involving the production of intense parasitic currents in a localized area. The effect, recorded between the drain electrode and the source one (SEB) or the gate one (SEGR), leaves a Si pore with a typical cylindrical structure. Furthermore, it includes the melting of the Pb layer in correspondence of the SEE which is then drawn to the Si pore making it evident in μ CT volume reconstruction images. The typical dimension of the new feature is 50 μ m in diameter and up to 300 μ m in height. The removal of the Pb from the solder layer is marked by a local depletion of this material giving rise to the formation of new void.

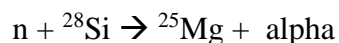
The procedure adopted to reveal the distribution of the Pb inside at the MOSFET device involved a sequence of routines of the ImageJ software. As a first step, the spatial segmentation of the region of interest in the image stack was performed. Subsequently, a contrast enhancement was necessary to increase the visual sensitivity to small X-ray adsorption differences. As a further filter, the FTT band-pass procedure was applied defining the spatial frequency domain in which the sample variations were expected. As an example, the slow varying structures (above 320 μ m - 40 pixels) were removed as well as the high spatial frequencies (below 20 μ m - 3 pixels) putting into evidence the features associated to the Pb layer. Finally, we applied a segmentation procedure by selecting a grey level range to be reconstructed in a 3D image. This allowed to pick-up the volume portion where the material of interest is placed by selecting the X-ray absorption values to which it is associated.

4.1.3. Discussion

We performed the analysis on 15 Power MOSFETs (7 with neutron damage and 8 fresh devices) by finding out the appropriate geometry and acquisition parameters for μ -CT with the aim to evidence SEEs occurred after the neutron irradiation procedure.

The single 2D reconstructed slices have been inadequate to determine SEEs traces and filtering, segmentation, and 3D rendering have been applied to put them into evidence. The methodology we developed and applied allowed us to find out the devices structures with a good correspondence with those proposed by the SEB (92) and SEGR models (93).

As already outlined, the microtomographic investigation corroborates the hypothesis that micro destructive SEEs on N-channel STP20N95K5 Power MOSFETs occur when a fast neutron interact with silicon nuclei producing secondary ionizing particles which produce high density of electron-hole pairs along their track in the silicon. collected at p-n bipolar junction when parasitic BJT turns ON and produce parasitic current able to lead the SEEs. More into details (100), neutron radiation damages in MOSFET devices are related to the generation of electron-hole pairs into semiconductor. Fast neutrons (their energy must be larger than a threshold value) induce target nuclear reactions giving rise to fragments as light particles (proton, alpha or deuterium) and heavier recoil nuclei that can generate a strong ionization process. Considering the most abundant silicon isotope in nature, i.e. ^{28}Si , the following two reactions may happen:



A further neutron-induced effect concerns the transfer a little amount of the neutron energy by displacing atoms from their reticular positions. The result of this non-ionizing process is the production of cluster of microscopic defects, which represents a disturbance of the lattice periodicity. Another point of view for this situation is the formation of energy levels into the band-gap, which may induce macroscopic effects, especially for cumulative dose. The single nuclear reaction cross section varies with the neutron energy as depicted for two of them in the following figure.

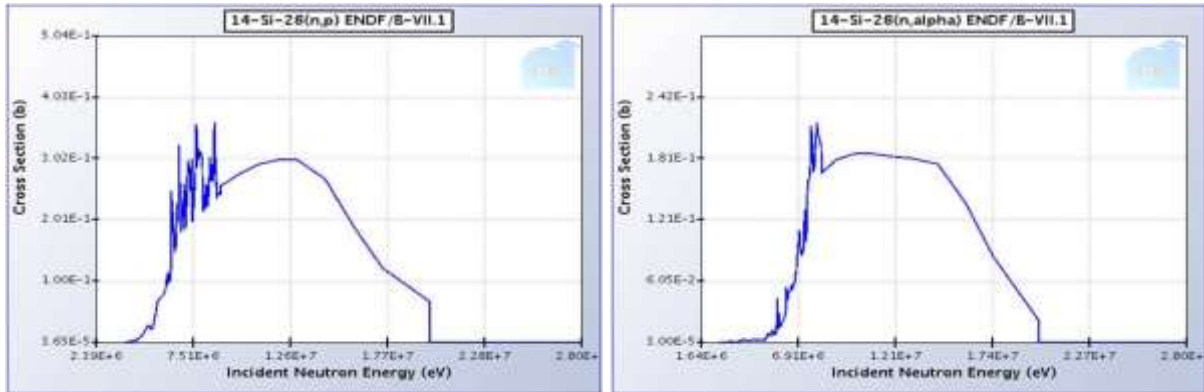


Figure 102: Cross section for $^{28}\text{Si}(n,p)^{28}\text{Al}$ reaction (left) and for $^{28}\text{Si}(n,\alpha)^{25}\text{Mg}$ reaction (right - from ENDF/B-VII.1 database)

In order to depict the SEB mechanism, we should note that the MOSFET structure contains a parasitic n-p-n bipolar BJT transistor whose emitter, base, and collector regions correspond to source, body, and drain regions of the MOSFET, respectively. In normal operation of the power MOSFET, this parasitic BJT is always turned off. If, for any reason, a lateral current flow in the body (base) below the source (emitter) region, the base-emitter junction can become forward-biased and the parasitic BJT can turn on causing a simultaneous high current and high voltage that induce a breakdown, hence a thermal meltdown. In our case, as a fast neutron traverses the device, electron-hole pairs are generated along its trajectory creating an ionized plasma filament that supports a short-lived current source which, in turn, drives the parasitic BJT locally turning on one cell of the MOSFET structure.

We unveil that when a SEB occurs, the meltdown produces a cylindrical pore in the source-to-drain direction and extends to the solder layer (87-91). The liquid Pb is then pulled in the pore by capillary forces leading to the production of a 50 μm -wide wire (the protrusion noted in the μCT reconstructions) that puts the MOSFET in short circuit in the region where the source electrode faces the drain one. As a result of this, a depletion of the Pb content in the solder layer is evidences.

A similar mechanism (96) is involved in the SEGR event where the involved region is related to the MOSFET gate one.

In freshly produced devices, where SEB and SEGR structures are not present, it was possible to investigate constructive defects.

The investigation performed on Power MOSFETs with the aim to study the SEEs demonstrates the power of the microtomography technique in this field of application. Non-destructive techniques as the X-ray micro-tomography described above allow to investigate structure of a sample without the necessity to use chemical or mechanical procedures. This work demonstrate that μ -CT demonstrates could be employed in industrial applications as the post failure analysis and the characterisation of the constructive process. Therefore, the information obtained with this technique represent a good guide to design innovative devices, more reliable regarding the environmental effects and to improve the industrial process and the construction quality of the devices.

4.2. Additional Experiments

4.2.1. Experiment 2: μ -CT Phase contrast and phase retrieval on organic matter

This experiment aimed to test the newly implemented filtered back-projection procedure of the SYRMEP Tomo Project (STP), a LabView-based tool developed for the users of the SYRMEP beamline of the Elettra Synchrotron to perform the digital image processing required for parallel beam propagation-based phase contrast CT experiments (101) (See Figure 103).

This aim was pursued by a study case where the internal structure of an onion bulb was investigated trying to find out the suitable parameters allowing to maximise the separation of its parts. The complete analysis involved the segmentation of the acquired data to put into evidence the bulb internal structure by differentiating them by means of the phase variation. The STP software uses the phase retrieval technique in PB-CT compared to a conventional CT, with the maximum achievable gain in the order of $0.3\delta/\beta$. This can lead to improved image quality and/or reduction of the X-ray dose delivered to patients in medical imaging (102).

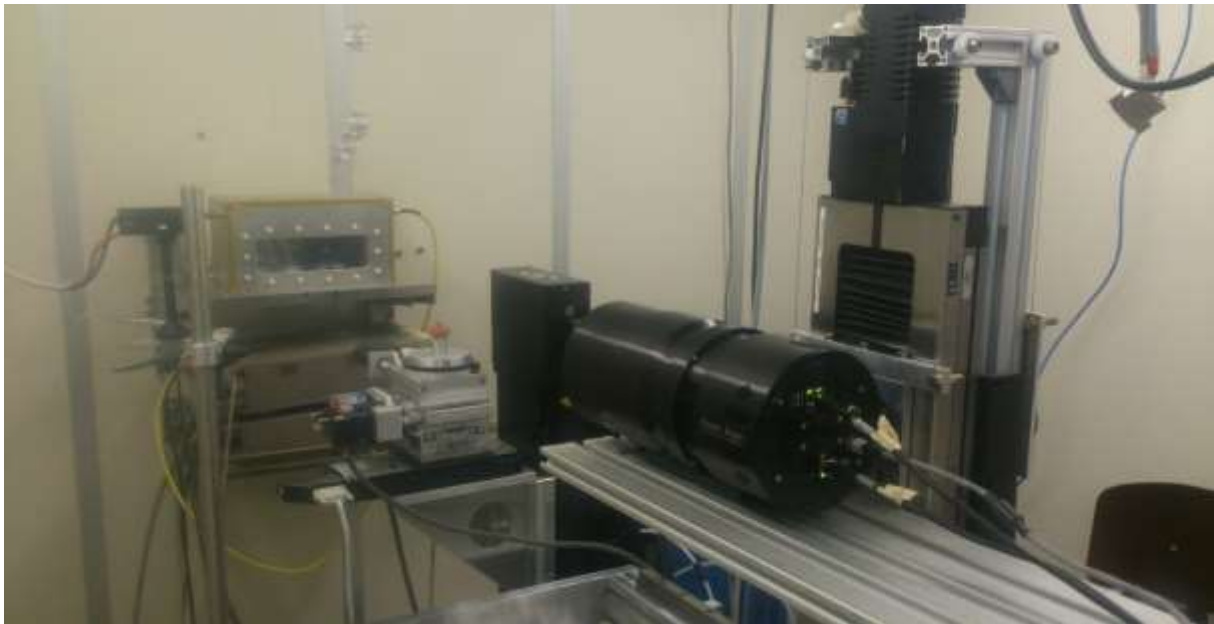


Figure 103: Setup of onion specimen

Parameters of μ CT:

| | |
|------------------------------|------------------|
| CT geometry: | Parallel beam |
| Time acquisition: | 750 ms |
| Energy: | 24 Kev |
| Current: | 3.5 mA |
| Pixel size: | 32.8 μ m |
| Distance sample to detector: | 30 cm |
| Number of projections: | 1201 projections |
| Number dark images: | 40 |
| Number flat images: | 40 |
| Step: | 0.15° |

Table 8: Parameters of μ CT

Results:

After the data acquisition procedure, we selected a 2011x140 \rightarrow 66 x 4.6 mm region of interest cropping the normalized radiographic image (see Figure 104).



Figure 104: Cropping normalized projection

The pre-processing consisted of setting the following parameters in STP software:

- Flat field determination for each radiographic image using the initial and final dark filed images.
- Rivers ring removal filters with a width of 15 pixels.

The phase retrieval was performed by means of the Paganin Algorithm (103) by setting the suitable δ / β values.

As part of the images pre-processing next image report the sinogram and the profile of a single line. The parabolic form is due to the degradation of gray values from the right and left sides to the center of the stack (see Figure 105).

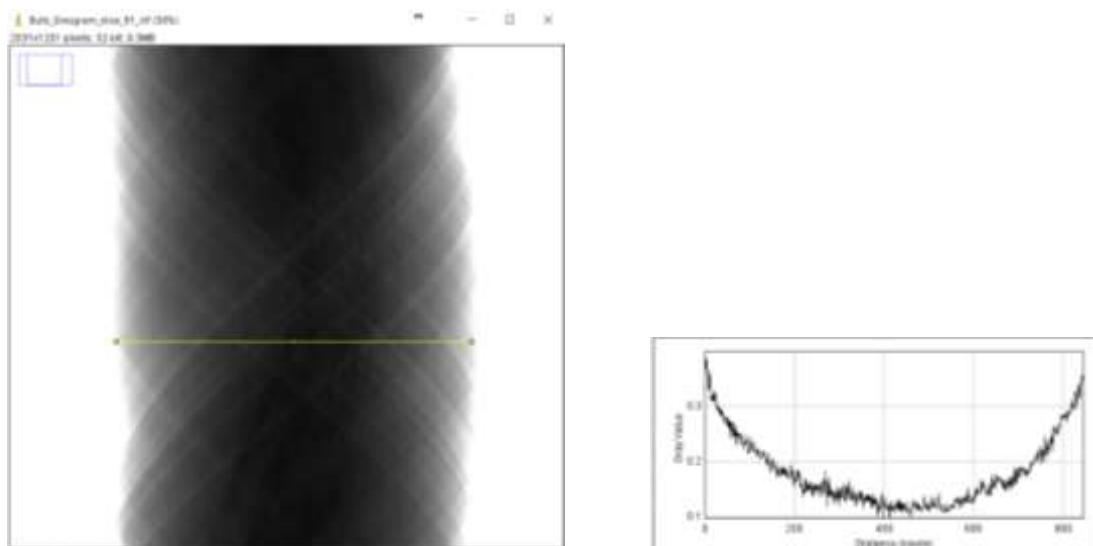


Figure 105: Sinogram of the Onion Bulb, Projection 91. Left: Sinogram. Right: Profile

Following the inspection of the sinograms, a 2D image reconstruction was performed without the phase retrieval algorithm. The parameters used were:

- Center of rotation: 9.
- Filter back projection was the algorithm used for reconstruction.
- Owing to size sample greater than the width of the beam, it was necessary to use half acquisition with an angle of 3.1416 rad.
- A circle mask was used which reduces the size of the normal matrix, for calculation of the diagonalized matrix and improvement of the resolution obtainable from the given data (104).

The following Figure 106 shows the bulb without phase retrieval, it does not show details due to the lack of contrast.

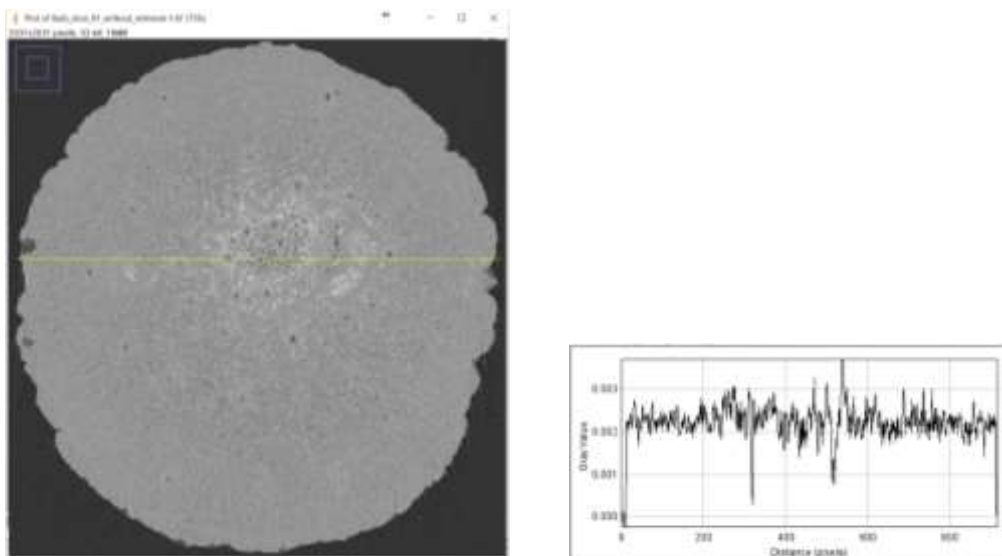


Figure 106: Slice 91 reconstruction without phase retrieval
Left: image without phase retrieval. Right: profile plot

The Figures 107 and 108 show the images of slice 91 with the phase retrieval procedure and its profile plot. The latter has a bell shape due to the setting of the phase retrieval without over

padding. We can directly appreciate a striking enhancement of the contrast-noise ratio (105). As parameters for the Paganin algorithm, we used $\delta/\beta = 1000$, with $\delta = 10^{-7}$ and $\beta = 10^{-10}$. The main component (gray values between dark and white) does not look homogeneous, but further segmentation is very hard due to the small range of variability in the intensity values.

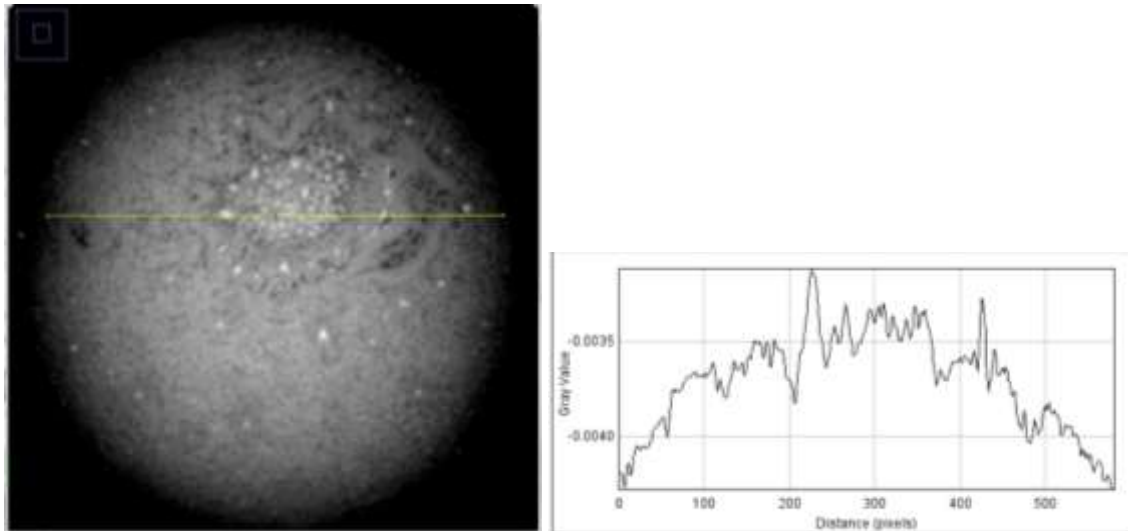


Figure 107: Slice 91 reconstruction with phase retrieval
Left: Image with phase retrieval. Right: profile plot

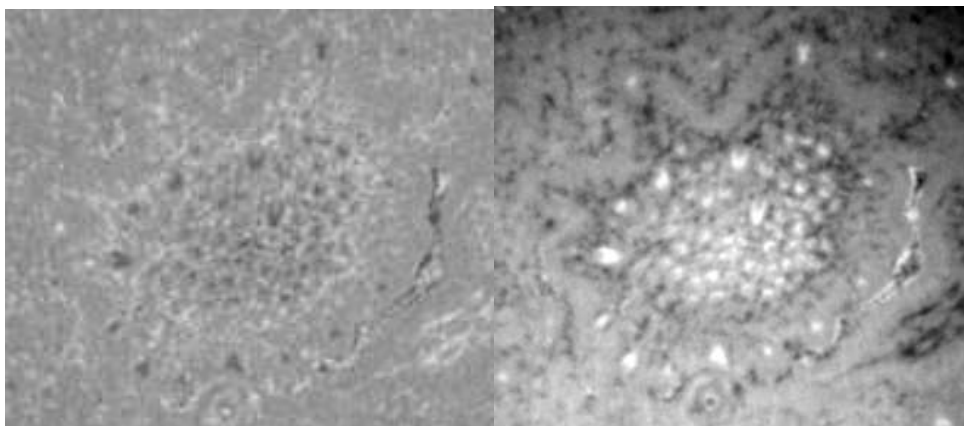


Figure 108: Comparison of the central part of slice 91 reconstructed images. Left: without phase retrieval. Right: with phase retrieval

The phase-retrieval procedure slightly reduces noise generated by the reconstruction procedure, creates a smooth edge-enhancement effect and allows an optimal greys distribution to be

separated to facilitate segmentation. A further procedure we adopted was the median filtering of the slices to reduce the noise. Thus, the 3D rendering was obtained after the segmentation procedure on filtered slices.

The study of the histogram hints to split the phase image in three different regions: 1) the darker one that looks like porosity; 2) the brighter one that has lower attenuation; 3) the main component that occupies more than 90% of the total volume. By focussing on the brighter regions, we can recover a 3D image of filaments present in the onion bulb (see Figure 109).

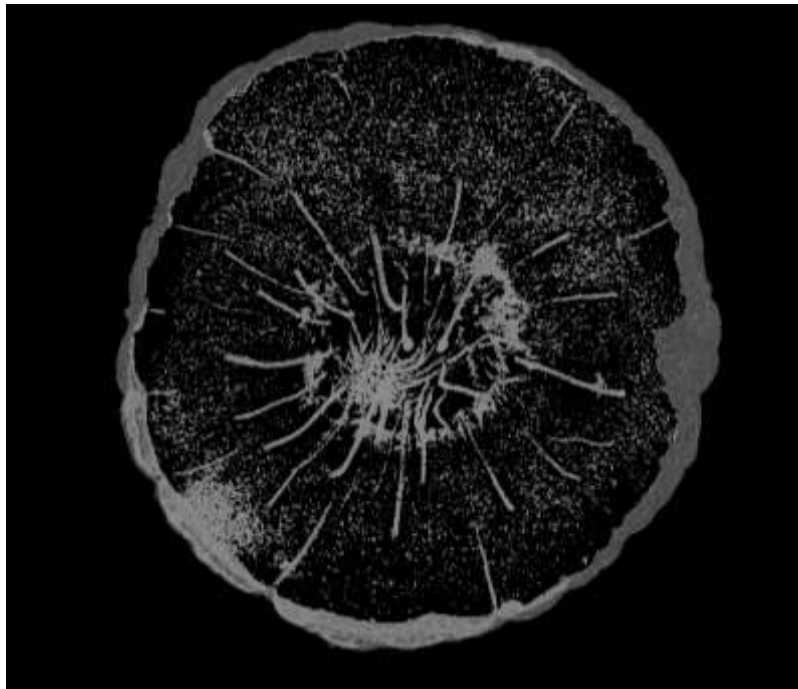


Figure 109: 3D Rendering - Filaments

The STP software at the Line SYRMEP in Elettra Synchrotron has been successfully tested. This is demonstrated by the results of the reconstruction process using filtered back projection of an onion bulb and the subsequent segmentation in its different components using a simple thresholding procedure. A 3D reconstruction was performed putting into evidence the bulb filaments.

4.2.2. Experiment 3: μ -CT Contrast analysis using a phantom

The aim of this work, performed at ID17 – ESRF, is to calculate the linear attenuation coefficients with their energy variation in a phantom that contains materials with properties similar to biological samples (Routine Preclinical CT Calibration Phantom from Smart Scientific Solutions B.V.) and to compare them with the reference data from the NIST. Furthermore, we aimed to compare the CNR plot with those expected from the theory for contrast transfer function after applying Paganin algorithm for phase retrieval.

In particular, our specific objectives were 1) determine the accuracy of the data processed with the Paganin algorithm and get quantitative results at different photon energies; 2) Check the changes the contrast transfer function in function of the energy, keeping the sample/detector at a fixed distance; 3) Develop and test a Graphical User Interface (GUI) written in Python language.

The Routine Preclinical CT Calibration Phantom (106) consist of known tissue-mimicking material (107) that are ideally suited for preclinical CT number calibration or for further multiple energy research when using a dedicated image-guided micro-IR (micro-irradiators) or preclinical in vivo CBCT devices. This routine phantom consists of a validation and calibration phantom as an independent test to determine and assess the accuracy and precision of DE-CT (dual energy – computed tomography) material decomposition algorithms (108).

4.2.2.1. Procedure

The experiment consists in to calculate the in the phantom the linear attenuation coefficients, the energy variation, and applying algorithm Paganin, to compare with the data from the NIST. Then, compare the CNR plot with those expected from the theory for contrast transfer function. The following figure shows the phantom placed on the computed tomographic stage during the acquisition, the distance between the detector and the stage was 2.5 m (See Figure 110).

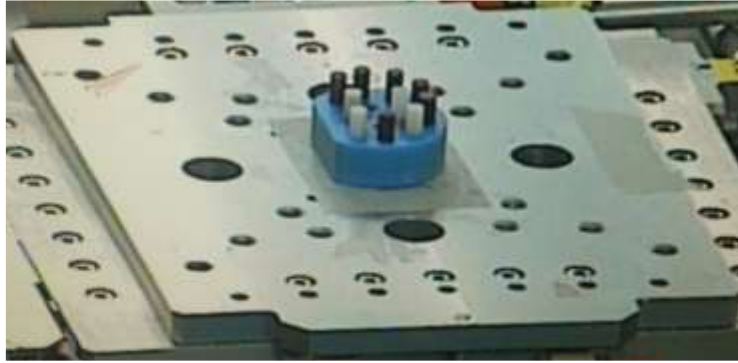


Figure 110: Phantom placed on the Computed Tomographic stage during the acquisition.

After preparing and aligning the sample stage, the ID17 wiggler was set for each selected energy and some filters were manually introduced to keep the same incoming flux on the object and to reduce the heat load on the optical elements. The Table 9 shows the used experimental parameters.

The first operation was to determine the exact centre of rotation for each μ -CT dataset. For this purpose, the GUI interface ID17_Rec was used, and a series of reconstructions performed automatically using different centres of rotation. As a second step, the optimal ratio δ/β (85) to perform the phase-retrieval was chosen again using another automatic method present in the reconstruction software.

The basic parameters of the reconstruction procedure are reported in the Table 10.

Figure 111 illustrates a reconstructed slice at photon energy equal to 30 keV where the regions of interest are numbered for each material according to the table on the right.

| Experimental parameters | | |
|-------------------------|------------------------|---------------------|
| Energy (keV) | Wigglers (mm) | Filters (mm) |
| 25 | W 150: 65 W 125: 55 | 0.8 C + 0.5 Al |
| 30 | W 150: 55 W 125: 65 | 0.8 C + 0.5 Al |
| 40 | W 150: 55 W 125: 45 | 0.8 C + 1 Al |
| 50 | W 150: 55 W 125: 45 | 0.8 C + 1 Al |
| 60 | W 150: 55 W 125: 45 | 0.8 C + 1 Al + 1 Cu |
| 70 | W 150: 55 W 125: 45 | 0.8 C + 1 Al + 1 Cu |
| 80 | W 150: 55 W 125: 45 | 0.8 C + 1 Al + 1 Cu |
| 90 | W 150: 55 W 125: 45 | 0.8 C + 1 Al + 1 Cu |

Table 9: Contrast Factor Phantom. C: Carbon, Al: Aluminium, Cu: copper.

| | | | |
|---------------------------------|------|------------------------|---------------------|
| Reconstruction starts in line = | 700 | Scan Name radix = | Contrast_Phantom_30 |
| Reconstruction ends in line = | 1400 | Number of projection = | 4000 |
| Paganin Length = | 100 | CT Range (180/360) = | 360 |
| Center of rotation = | 2524 | y start = | 1 |
| Sampling reduction (SR) = | 1 | y end = | 2160 |
| Image reconstructed with: | | Width = | 2560 |
| projections /SR | | Height = | 2160 |
| | | Pixel Size = | 3.05 |
| | | Binning XY = | 1 |
| | | Binning Z = | 1 |
| | | WF name = | ref0000_0000.mff |
| | | Number of WF = | 100 |

Table 10: Basic parameters of the reconstruction

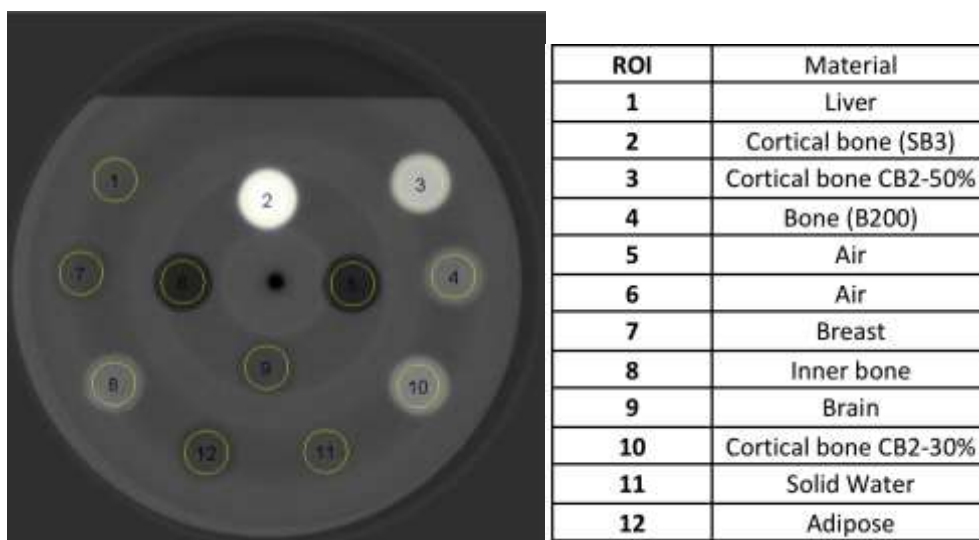


Figure 111: Slice 1000 reconstructed. Depiction of CT calibration phantom; μ CT scan at 30 keV.

Evaluation of linear attenuation coefficient.

The values of Table 11 were used for calculation, ‘Material’ is a type of material, ‘location’ is the location in the ROI phantom, ‘density’ and the elemental composition by relative weight respectively.

| Material | Location | Density | H | C | N | O | P | Cl | Ca |
|-----------------------|----------|---------|-------|-------|------|-------|------|------|-------|
| “Solid Water” | 11 | 1.02 | 8 | 67.29 | 2.39 | 19.87 | 0 | 0.14 | 2.31 |
| Adipose | 12 | 0.95 | 9.06 | 72.29 | 2.25 | 16.27 | 0 | 0.13 | 0 |
| Brain | 9 | 1.05 | 10.83 | 72.54 | 1.69 | 14.86 | 0 | 0.08 | 0 |
| Liver | 1 | 1.1 | 8.06 | 67.01 | 2.47 | 20.01 | 0 | 0.14 | 2.31 |
| Bone (B200) | 4 | 1.15 | 6.65 | 55.51 | 1.98 | 23.64 | 3.24 | 0.11 | 8.87 |
| Inner bone | 8 | 1.13 | 6.67 | 55.65 | 1.96 | 23.52 | 3.23 | 0.11 | 8.86 |
| Breast | 7 | 0.98 | 8.59 | 70.1 | 2.33 | 17.9 | 0 | 0.13 | 0.95 |
| Cortical bone CB2-30% | 10 | 1.33 | 6.68 | 53.47 | 2.12 | 25.61 | 0 | 0.11 | 12.01 |
| Cortical bone CB2-50% | 3 | 1.56 | 4.77 | 41.61 | 1.52 | 32 | 0 | 0.08 | 20.02 |
| Cortical bone (SB3) | 2 | 1.82 | 3.41 | 31.41 | 1.84 | 36.5 | 0 | 0.04 | 26.8 |

Table 11: Phantom material composition data

The linear attenuation coefficient describes the fraction of a beam of X-rays absorbed or scattered per unit thickness of the absorber (109). The theoretical values of the mass attenuation coefficient were calculated using eq. 16 (110) and the EPDL97 cross-section database (111):

$$\frac{\mu}{\rho_{mix}} = \sum_i w_i \left(\frac{\mu}{\rho}\right)_i \quad \text{Eq. 16}$$

With:

$\frac{\mu}{\rho_{mix}}$: mass attenuation coefficient of the composed material

w_i : is the fraction by weight of the its atomic constituent

$(\mu/\rho)_i$: mass attenuation coefficient of the single element at given energy.

The evaluated linear attenuation coefficients were calculated for product:

$$\text{linear attenuation coefficients} = \rho \sum_i w_i \left(\frac{\mu}{\rho}\right)_i \quad \text{Eq. 17}$$

with ρ the density of the material.

The experimental linear attenuation values were obtained from the μ CT scans at different energies and reported in the following table.

| Energy (keV) | Solid Water | Adipose | Brain | Liver | Bone (B200) | Inner bone | Breast | Cortical bone CB2-30% | Cortical bone CB2-50% | Cortical bone (SB3) |
|--------------|-------------|---------|-------|-------|-------------|------------|--------|-----------------------|-----------------------|---------------------|
| 25 | 0,527 | 0,342 | 0,374 | 0,569 | 1,181 | 1,159 | 0,416 | 1,535 | 2,624 | 3,873 |
| 30 | 0,391 | 0,276 | 0,304 | 0,423 | 0,791 | 0,777 | 0,322 | 1,018 | 1,686 | 2,452 |
| 40 | 0,274 | 0,219 | 0,243 | 0,296 | 0,442 | 0,434 | 0,241 | 0,568 | 0,869 | 1,214 |
| 50 | 0,228 | 0,195 | 0,218 | 0,247 | 0,330 | 0,324 | 0,209 | 0,404 | 0,575 | 0,771 |
| 60 | 0,207 | 0,182 | 0,204 | 0,223 | 0,276 | 0,271 | 0,192 | 0,334 | 0,452 | 0,588 |
| 70 | 0,192 | 0,173 | 0,194 | 0,207 | 0,242 | 0,238 | 0,181 | 0,288 | 0,373 | 0,470 |
| 80 | 0,183 | 0,167 | 0,187 | 0,197 | 0,222 | 0,218 | 0,171 | 0,262 | 0,329 | 0,405 |
| 90 | 0,174 | 0,160 | 0,180 | 0,188 | 0,207 | 0,203 | 0,166 | 0,244 | 0,300 | 0,365 |

Table 12: Experimental linear attenuation coefficients for the Phantom materials.

Finally, the following table shows the percentage difference between theoretical and experimental values. The variation with respect to the expected values is in the +/- 10% range. In particular, the cortical bone (SB3) shows the maximum positive error at 25% while the experimental values are always lower than the theoretical ones for brain (with a maximum error of -9,21% at 50 keV). For this reason, these quantitative values cannot be used to distinguish between materials with a similar optical characteristic like soft tissues based only on the quantitative information obtained from the reconstruction.

| % DIFFERENCE OF THEORIC VALUES AND EXPERIMENTAL VALUES | | | | | | | | | | |
|--|-------------|---------|-------|-------|-------------|------------|--------|-----------------------|-----------------------|---------------------|
| Energy (keV) | Solid Water | Adipose | Brain | Liver | Bone (B200) | Inner bone | Breast | Cortical bone CB2-30% | Cortical bone CB2-50% | Cortical bone (SB3) |
| 25 | 1.00 | 1.59 | -5.27 | 4.93 | 1.48 | 1.70 | 2.29 | -0.02 | 4.34 | 9.05 |
| 30 | 2.79 | 2.36 | -7.79 | 0.19 | 0.26 | -2.02 | -4.55 | -1.76 | -0.80 | -1.01 |
| 40 | 3.36 | 3.87 | -9.13 | 0.92 | -1.85 | -3.66 | -1.50 | -1.08 | -1.25 | -3.79 |
| 50 | 4.03 | 4.00 | -9.21 | 1.44 | 1.69 | 0.07 | 0.08 | 0.76 | 0.13 | -4.25 |
| 60 | 4.90 | 4.95 | -9.02 | 3.53 | 3.46 | 3.40 | 2.43 | 3.76 | 4.08 | -0.73 |
| 70 | 3.37 | 3.76 | -9.86 | 2.05 | 2.03 | 1.47 | 1.88 | 1.57 | 1.31 | -4.16 |
| 80 | 4.72 | 4.97 | -8.28 | 2.53 | 1.83 | 1.65 | 0.33 | 1.76 | 0.68 | -6.40 |
| 90 | 3.52 | 4.44 | -9.01 | 1.90 | 1.47 | 1.40 | 1.19 | 1.51 | 0.45 | -6.95 |

Table 13. Percentage difference between theoretical and experimental values of the linear attenuation coefficients for the Phantom materials.

CNR Calculation

On exploiting the metric of Contrast-to-Noise Ratio (CNR) (112), we make use of the following definition of CNR (113)

$$CNR = \frac{|S_a - S_b|}{\sqrt{\frac{1}{2}(\sigma_a^2 + \sigma_b^2)}} \quad \text{Eq. 18}$$

where S_a and S_b represent the measured signals, with S_a corresponding to the average value of a ROI in a slice, and S_b corresponding to the average value of the background, instead σ_a and σ_b are the standard deviations of those respective regions which indicate the noise levels.

The CNR was calculated using Eq. 18 for each material of the phantom. Figure 112 show the variation of the CNR values versus the photon energies.

The results indicate that, independently on the probed material, the higher CNR values were attained at photon energy close to 30 keV. The CNR values at this energy are up to 4 times those at high energy (>80 keV). The only exception is the “brain” sample where no gain is recorded.

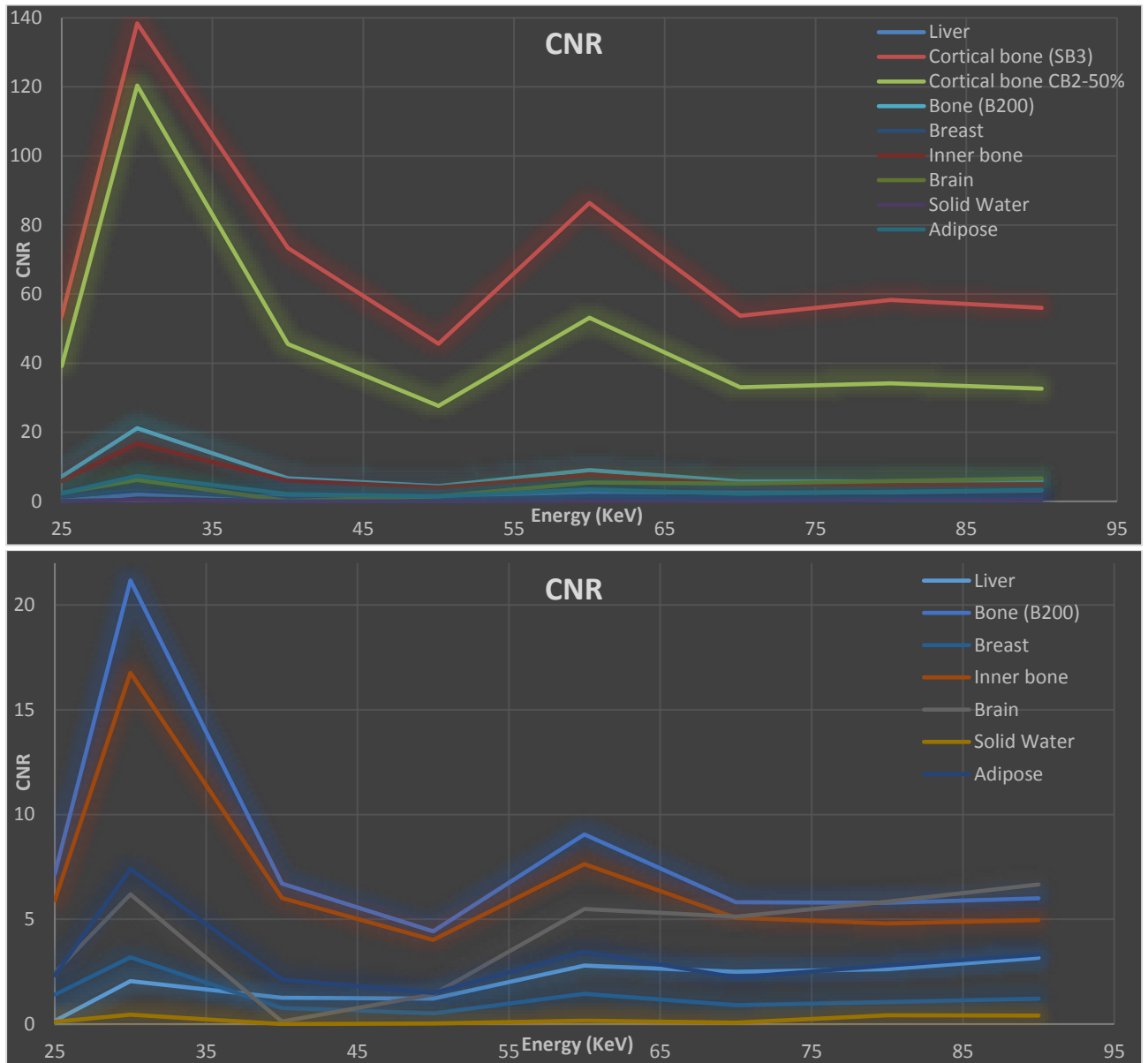


Figure 112: CNR values for phantom materials (above). Zoom on the materials with CNR < 30 (below).

To understand the reported behaviour, we performed a theoretical calculation of partially coherent Contrast Transfer Function (CTF):

$$CTF = 2 * \text{Sin}(\pi * X * D * (f^2))$$

for $\delta \gg \beta$ (purely refractive) and for a finite source size (113) with the following parameters:

| | |
|---|---|
| $\text{pixel} = 0,000006 \text{ [m]}$ | { effective pixel size } |
| $f = 1/\text{pixel} = 166666,667 \text{ [m}^{-1}\text{]}$ | { frequency } |
| $D = 2,5 \text{ [m]}$ | { sample-to-detector distance } |
| $E \text{ (keV)}$ | { energy } |
| $\lambda \text{ [Å]} = 12.4 / E \text{ (keV)}$ | { photon wavelength as a function of energy } |
| $X = \lambda * 10^{-10}$ | { photon wavelength by conversion factor } |

The results are plotted in the following Figure:

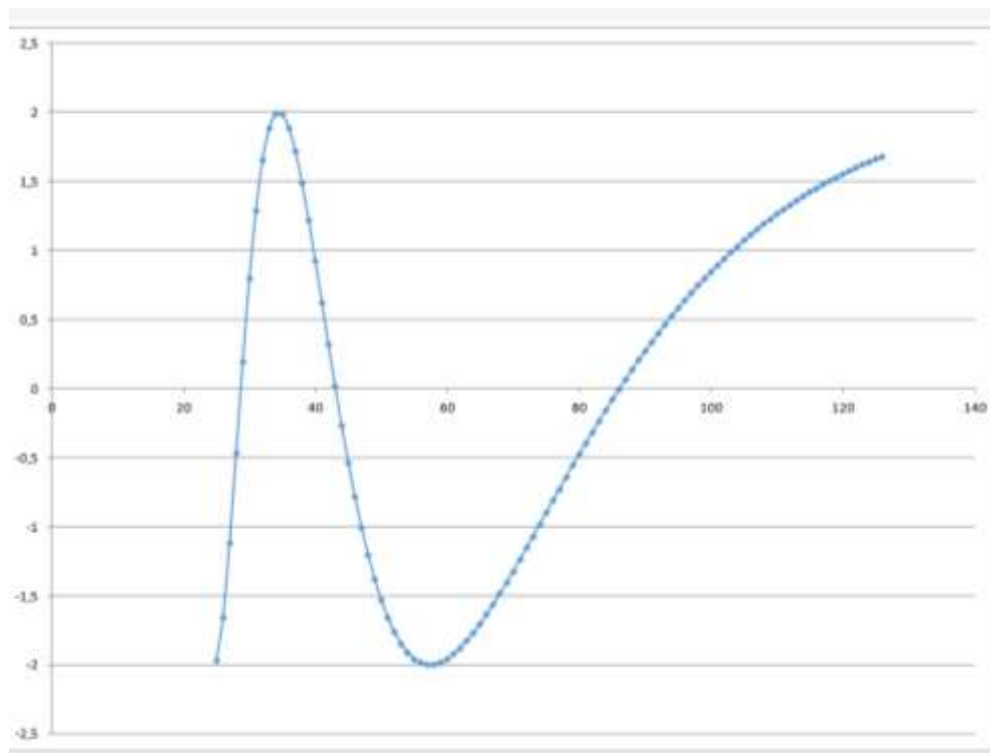


Figure 113: Plot of CTF

CFT considers for the effects of the distortion in the recorded images induced by the apparatus provided that the measurements have been performed with an object-to-detector distance of 2.5 m and the detector pixel size is 6.2 μm .

Comparing the behaviour of the CNR as function of the energy with the theoretical curve of the CTF (114) a similarity is observed. The peak appearing in the CTF graphic at about 30 keV coincides with the first experimental maximum of the CNR plot. Thus, using the previously listed experimental parameters, 30 keV represents the optimal photon energy to maximize the image contrast. The differences between the CNR and CTF curves occurring at higher energies can be explained by keeping in mind that we are dealing with a partially coherent illumination whose performance is degraded additionally by the blurring effects linked to the modular transfer function of the detector.

4.2.3. Experiment 4: μ -CT on a plasticized rat

The general objective of this experiment, performed at ID17 – ESRF, was to develop and test a Graphical User Interface developed in Python language for the acquisition of massive samples. The GUI was then used for the 3D reconstruction of a plasticized rat. Concerning the latter goal, the specific objectives were the 3D rendering of rat brain.

4.2.3.1. Introduction

As already noted, high-resolution X-ray computed tomography (micro-CT) produces detailed three-dimensional images of soft tissue and bone structure. In the case of soft tissue, the highest resolutions are achieved with the help of a contrast agent, which increases the X-ray attenuation of the tissue of interest. For this technique, the need for high X-ray doses to obtain the finest resolution precludes scanning of live specimens (116). The multi-contrast X-ray images of a biological tissue can be obtained with a conventional X-ray image based on attenuation, the differential phase-contrast image based on X-ray refraction, and dark-field image based on X-ray scattering. (117)

The plasticized rat (PlastiRat from Smart Scientific Solution BV) is an extremely useful tool for conducting imaging quality assurance tests as well as for irradiation planning studies, and for educational purposes. The benefit of PlastiRat is that it is biologically inert, being a motionless rigid object that represents the true anatomy of a living rat including all the mineralized components of the bones (108) (See Figure 114).



Figure 114: Plastirat sample on the Computed Tomographic stage.

Parameters of experiment

- Energy: 60 KeV
- FReLoN CCD camera coupled with 1:3.6 optic.
- Effective pixel size $47 \mu\text{m}^2$
- Filter: 2.5 mm Al + 0.8 mm C
- Wigglers: W150 – 55 mm, W125 - 45 mm
- The distance between the sample stage and the detector was 11 m.

Detector

The FReLoN (the acronym stands for Fast-Readout, Low-Noise) is a CCD camera developed by the ESRF Instrument Support Group (see Figure 115).

- Detector maximum resolution: $50 \mu\text{m}$
- Gadolinium scintillator (40 μm thickness)



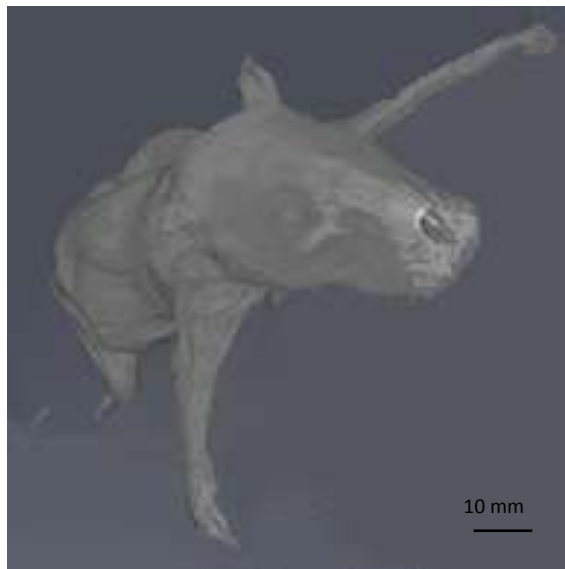
Figure 115: Detector couple with the 1:3.6 optic.

4.2.3.2. Results: 3D Rendering and Segmentation

ImageJ was used for 3D rendering and segmentation. The segmentation assigns a label to each pixel of the image describing to which region or material the pixel belongs (118) .

Figures 116(a) show external tissue, Figures 116(b) - 116(d) depict the skeleton view, Figure 117 shows the transversal view of rat, and Figures 118 - 120 illustrate some different views of 3D brain of a rat for means of segmentation technique “region growing segmentation” (119).

The GUI developed in Python allowed the μ -CT of the rat, while for the elaboration of the 3D images of the external tissue, skeleton, transversal section, and the segmentation of the brain of the rat were made using ImageJ. This work may allow later an anatomical study of the rat or a quantitative analysis of some organ of interest.



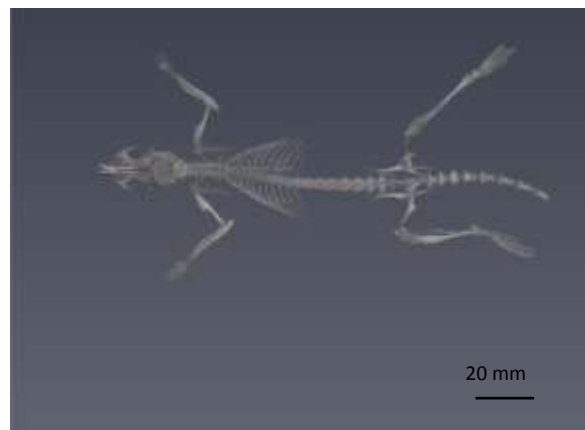
(a)



(b)



(c)



(d)

Figure 116: Segmentation images

(a) Rat external tissue. (b) Skeleton - Top view. (c) Skeleton - Side view (d) Skeleton – Bottom view.



Figure 117: 3D - Transversal view

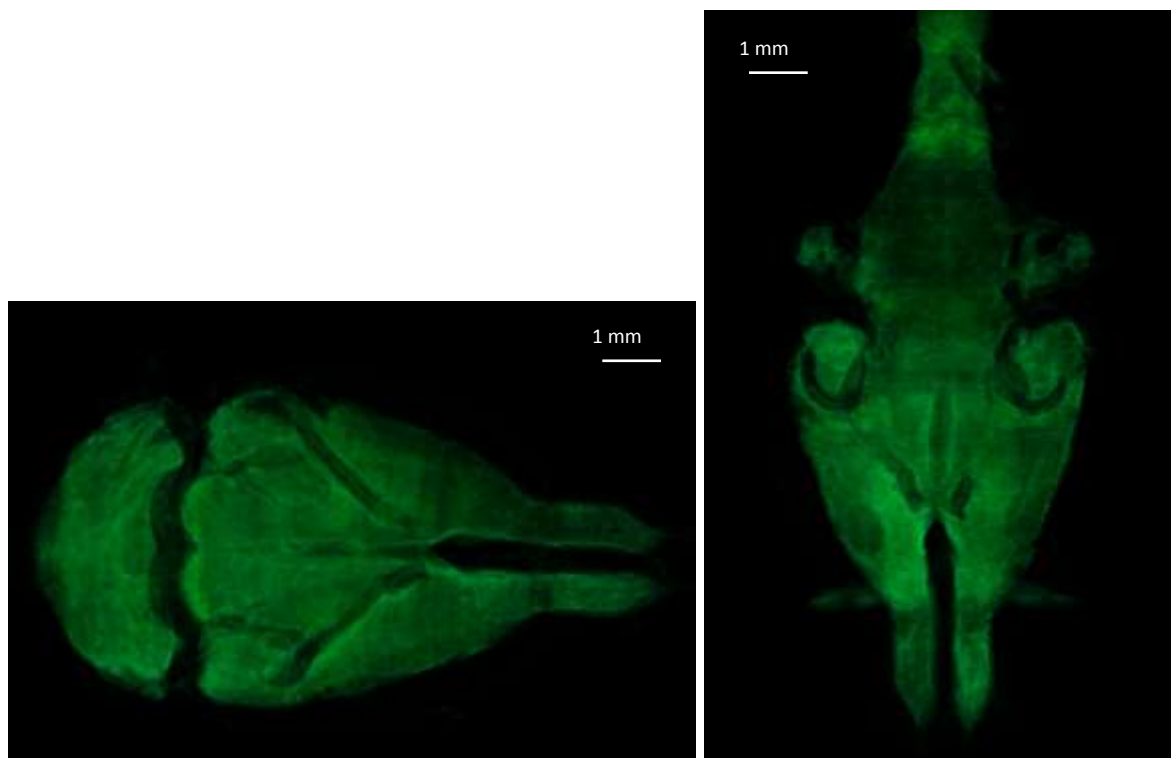


Figure 118: Brain - Top View
Left: Top view. Right: Cross section

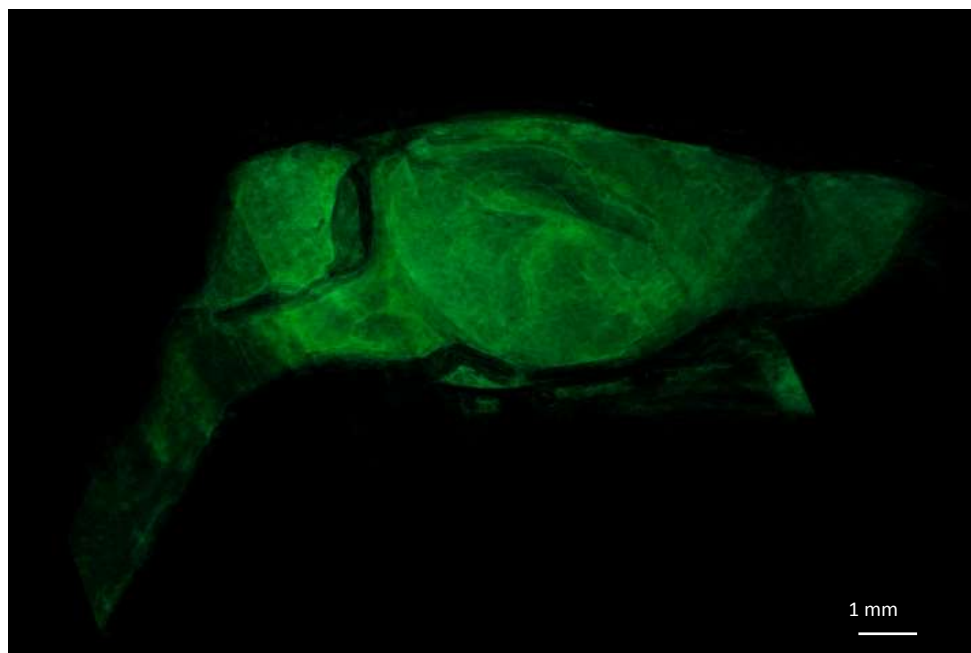


Figure 119: Brain - Side View

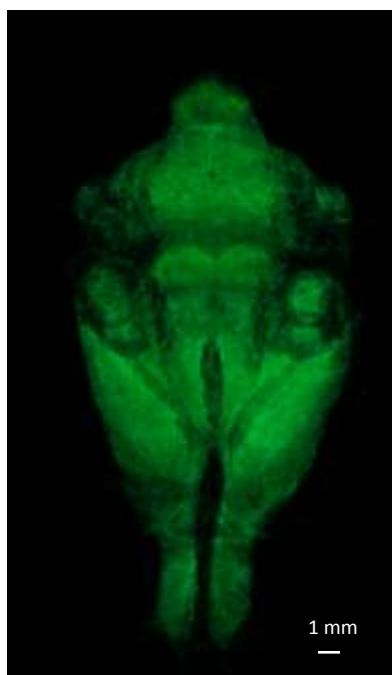


Figure 120: Brain - Bottom View

5. Conclusions

The research work reported in the present dissertation concerns different activities performed on the development and test of X-ray micro-tomographic tools. The main activity was performed at the STAR facility at the University of Calabria, Italy. It involved the software for the μ Tomo experimental station control based on LabView over EPICS platform. The flexibility of the system permits to operate with both X-ray micro-focus conventional source or with a TBS source. The control software was linked to the EPICS platform and permits to exploit all the characteristics of the X-ray source giving the possibility to integrate diverse field of research and science.

The upgrade from a purely LabView server to an integrated LabVIEW/EPICS server was performed using the DSC software and creating network shared variables for reading or writing to/from EPICS client. This solution allows operating the μ Tomo Station into STAR network. The main difference between synchrotron-based system for microtomography (ID-17@ESRF and Symrep@Elettra) and the microtomographic system based on micro-focussed sources (as, temporarily, μ Tomo) is linked to the X-ray source. The synchrotron systems use monochromatic parallel beams with a high flux of photons, while the micro-focus source provide a lower flux of photons and a cone beam geometry.

The adequate focal spot, the source-to-detector distance, and source-to-sample distance are very important for determine the effective pixel size, the scanning time, and reduction of artefacts in the images. The filters are very important to obtain an effective flux of the photons that contribute to form the image.

For the reconstruction process is necessary tuning the acquisition parameters, cropping of the region of interest, selecting to an adequate dynamic range on histogram before of reconstruction. The inconsistencies in the reconstructions can are due to imperfections of the beam, poor performance in the detector, geometry of the system, and sample wobbling during scanning.

The phase-contrast signal needs to be exploited by means of a phase retrieval algorithm. Normally a μ -CT scan looks for the best contrast for diverse methods such as: increasing the distance of the sample to the detector; the distances source-to-detector and sample-to-detector are necessary to optimize the magnification and obtain the best contrast, making a test of image contrast at different energy, the high sensitivity of phase-contrast techniques leads to an increase of the contrast in the image, other important reasons for improving the image contrast is to obtain quantitative information.

As demonstrated by a first application of the developed tools, the microtomography system allowed to fully describe the internal structure of MOSFET devices using a non-destructive technique. The results allowed to give for the first time a detailed description of the Single Event Effects taking place in MOSFET devices when irradiated by a fast neutron flux. Both, Single Event Burnout and Single Event Gate Rupture showed a similar mechanism involving the production of a local meltdown of the silicon wafer in correspondence of the source-to-drain (gate-to-drain) region whose typical dimension are 50 μm in diameter and 300 μm in height. As the segmentation clearly depicted, the event involves the melting of the Pb solder layer and its role in building a short-circuit micrometric wire between the drain and the other electrodes.

The development and test of data acquisition software was also performed at two beamlines are dedicated to μ CT in a Synchrotron infrastructure: the SYRMEP beamline at Elettra, Italy, and ID17 beamline at ESRF, France.

In Trieste, we performed the test of a newly implemented filtered back-projection procedure of the SYRMEP Tomo Project (STP), a LabView-based tool developed for the users to perform the digital image processing required for parallel beam propagation-based phase contrast CT experiments.

In Grenoble, on the other side, the goal was to develop and test a Graphical User Interface in Python language for the acquisition of massive samples. The GUI was then used for the 3D reconstruction of a plasticized rat.

6. Annexes

6.1. Annex 1

Parameter File saving from GUI (ID-17 ESRF)

```

Scan_Name radix = MyFile_00_           #Radix of the file (without extension)
WF_name = ref0000_0000.edf             #Name of one white field file
Number_of_WF in the file = 20          #Number of white fields acquired
Number_of_projections = 2400
CT_Range (180/360) = 180
Sample_Positioning (left/right) = left #In the case of half acquisition
Half_Acquisition (yes/no)? = no
Reconstruction_starts in line = XXX    #CT reconstruction starts in line XXX
Reconstruction_ends in line = XXX      #CT reconstruction end in line XXX
Rotation_Axis (H/V) =                  #H: horizontal, V: vertical rotation axis -> so far
                                         it is not used, so just keep it like that

###DEFINE ROI###
y_start = XXX                           #ROI start
y_end = XXX                              #ROI end
Width = 2048
Height = 160
Pixel_Size = 47.82
Binning XY = 1                          #Binning in the reconstruction plane
Binning Z = 1                           #Binning along the vertical axis
###DEFINE PBI PHASE RETRIEVAL###
Do_Paganin (yes/no)? = yes
Paganin_Length = 1000
Ring_Correction (yes/no) = no          #pyhst ring correction

###MISCELLANEOUS###

```

Only_CT (yes/no) = no #If you want to perform only the CT reconstruction. If yes, the normalized/split projections will be saved in the folder Images/

Make_Sinos = no #It saves the sinograms. It can be used only if "Only_CT = no". The folder created with the sinograms is: Sinos/

TOPUP (yes/no) = no #Normalize considering the current at which the projection is saved. It works only if Only_CT = no, the normalized images are save in the folder Images/

6.2. Annex 2

NRecon: Reconstruction parameters file

```
# Begin of log file #####
[System]
Scanner=SkyScan1172
; A string with at least 11 characters. Typically, the first 7 characters refer to the company,
and the last 4 characters are 4-digits ---
; scanner model (in case of non-digits, it is interpreted as 0). Model number 0-2999: X-ray
systems;
; Model3000-3999: Optical scanner systems
; Please respect the number of letters: hardcoded inside NRecon.
Instrument S/N=2
; info only: serial number of the scanner
[Acquisition]
Optical Axis (line)= 1150
; Important parameter: the central slice in which the x-ray hits the detector
perpendicularly;
Object to Source (mm)=90
```

; Important parameter: distance between image center and the x-ray source. If the distance is $> 10\text{m}$, it is assumed that it is a

; parallel beam scan.

Number of Files=1617

; Info only. Number of projections, dimension and pixel information are actually obtained/confirmed from the TIFF files

Number of Rows=2067

; info only

Number of Columns=2071

; info only

Image Pixel Size (μm)=50

; info only. The pixel size is read from the header of the 16-bit TIFF files.

; Important! For cone-beam geometry: the concept of "virtual detector" is exploited. More specifically, the detector is

; assumed to be centered at the FOV.

; Therefore, the pixel size in the TIFF header should have been scaled accordingly.

; Alternatively, one may use the non-standard key Scaled Image Pixel Size (μm) to indicate pixel size scaled at image center.

Linear pixel value=-1

; Non-standard key. Default: 0, exponential attenuation case; 1: Linear case; -1: inverse linear

Scaled Image Pixel Size (μm)=10

; Non-standard key. When present, it has higher priority than pixel information in TIFF header

Exposure (ms)=100

; info only

Rotation Step (deg)=0.2

; Important parameter

Table Feed (micron)=0.0

; Spiral CT specific: table movement length per rotation step

; Positive: table movement direction coincides with projection vertical direction

Use 360 Rotation=YES

; Important parameter: YES or NO (360 or 180+)

Flat Field Correction=ON

; info only

Rotation Direction=CC

; Important parameter: TRY IT OUT TO SEE IF IT SHOULD BE cc OR cw. Almost all SkyScan scanners have rotation direction CC.

Type of Detector Motion=STEP AND SHOOT

; info only

Scanning Trajectory=ROUND

; info only. Spiral scan is recognized by entry "table feed"

Study Date and Time=Aug 10, 200515:13:11

; info only

End of log file

#####

NRecon: Calibration parameters file

[Global calibration parameters]

Original projection width=2240

Original projection height=2368

Original optical axis=1150

Calibrated focal length=90000.000000

Calibrated source-camera distance=450000.000000

Original pixel size in micron=50.000000

Calibrated camera rotation Theta in degree=0.130000

Calibrated camera in-plane rotation Phi in degree=0.000000

Calibrated camera tilt Psi in degree=0.000000

Calibrated camera shift Eu in micron=0.000000

Calibrated camera shift Ev in micron=0.000000

Original number of views=1800.000000

Original rotation step in degree=0.200000

7. References

1. Mayo, Sheridan C., Andrew W. Stevenson, and Stephen W. Wilkins. "In-line phase-contrast X-ray imaging and tomography for materials science." *Materials* 5.5 (2012): 937-965.
2. Landis, Eric N., and Denis T. Keane. "X-ray microtomography." *Materials characterization* 61.12 (2010): 1305-1316. DOI: [10.1016/j.matchar.2010.09.012](https://doi.org/10.1016/j.matchar.2010.09.012)
3. Davis, Graham Roy, and Ferranti SL Wong. "X-ray microtomography of bones and teeth." *Physiological measurement* 17.3 (1996): 121.
4. Feldkamp, Lee A., et al. "The direct examination of three-dimensional bone architecture in vitro by computed tomography." *Journal of bone and mineral research* 4.1 (1989): 3-11.
5. Winick, Herman. "Fourth generation light sources." *Particle Accelerator Conference, 1997. Proceedings of the 1997*. Vol. 1. IEEE, 1997.
6. Rügsegger, P., B. Koller, and R. Müller. "A microtomographic system for the non-destructive evaluation of bone architecture." *Calcified tissue international* 58.1 (1996): 24-29.
7. Clark, D. P., and C. T. Badea. "Micro-CT of rodents: state-of-the-art and future perspectives." *Medic Physics* 30.6 (2014): 619-634.
8. Ritman, Erik L. "Current status of developments and applications of micro-CT." *Annual review of biomedical engineering* 13 (2011): 531-552. DOI: <https://doi.org/10.1146/annurev-bioeng-071910-124717>
9. Boerckel, Joel D., et al. "Microcomputed tomography: approaches and applications in bioengineering." *Stem cell research & therapy* 5.6 (2014): 144. DOI: <https://doi.org/10.1186/scrt534>
10. Stauber, Martin, and Ralph Müller. "Micro-computed tomography: a method for the non-destructive evaluation of the three-dimensional structure of biological specimens." *Osteoporosis: Methods and Protocols* (2008): 273-292.
11. Lewis, R. A. "Medical phase contrast x-ray imaging: current status and future prospects." *Physics in medicine and biology* 49.16 (2004): 3573. DOI: [10.1088/0031-9155/49/16/005](https://doi.org/10.1088/0031-9155/49/16/005)
12. Fitzgerald, Richard. "Phase-sensitive x-ray imaging." *Phys. Today* 53.7 (2000): 23-26.

13. Mohammadi, Sara. "Bio-medical X-ray imaging with Synchrotron Radiation: study and implementation of algorithms related to phase sensitive techniques." (2013).
14. Kharfi, Faycal. "Mathematics and Physics of Computed Tomography (CT): Demonstrations and Practical Examples." *Imaging and Radioanalytical Techniques in Interdisciplinary Research-Fundamentals and Cutting Edge Applications*. InTech, 2013.
15. Egan, C. K., et al. "3D chemical imaging in the laboratory by hyperspectral X-ray computed tomography." *Scientific reports* 5 (2015): 15979.
16. Soleimani, M., and T. Pengpen. "Introduction: a brief overview of iterative algorithms in X-ray computed tomography." (2015): 20140399.
17. Thibault, Jean-Baptiste. "Iterative image reconstruction for multi-slice x-ray computed tomography." (2006).
18. Banhart, John, ed. *Advanced tomographic methods in materials research and engineering*. Vol. 66. Oxford University Press, 2008.
19. Soleimani, M., and T. Pengpen. "Introduction: a brief overview of iterative algorithms in X-ray computed tomography." (2015): 20140399.
20. Bronnikov, Andrei V. "Phase-contrast CT: fundamental theorem and fast image reconstruction algorithms." *Proc. SPIE*. Vol. 6318. 2006.
21. Zhou, Shu-Ang, and Anders Brahme. "Development of phase-contrast X-ray imaging techniques and potential medical applications." *Physica Medica* 24.3 (2008): 129-148. DOI: [10.1016/j.ejmp.2008.05.006](https://doi.org/10.1016/j.ejmp.2008.05.006)
22. Zhou, Shu-Ang, and Anders Brahme. "Development of phase-contrast X-ray imaging techniques and potential medical applications." *Physica Medica* 24.3 (2008): 129-148.
23. Gureyev, T. E., et al. "Refracting Röntgen's rays: propagation-based x-ray phase contrast for biomedical imaging." *Journal of Applied Physics* 105.10 (2009): 102005.
24. Cai, Weixing. *Feasibility study of phase-contrast cone beam CT imaging systems*. PhD thesis, University of Rochester, 2009.
25. Lussani, Fernando Cesar, et al. "A versatile x-ray microtomography station for biomedical imaging and materials research." *Review of Scientific Instruments* 86.6 (2015): 063705.
26. Hanson, Kenneth M. "Noise and contrast discrimination in computed tomography." *Radiology of the Skull and Brain* 5.1 (1981): 3941-3955.

27. Cnudde, Veerle, and Matthieu Nicolaas Boone. "High-resolution X-ray computed tomography in geosciences: A review of the current technology and applications." *Earth-Science Reviews* 123 (2013): 1-17.
28. Boas, F. Edward, and Dominik Fleischmann. "CT artifacts: causes and reduction techniques." *Imaging Med* 4.2 (2012): 229-240.
29. Schulze, R., et al. "Artefacts in CBCT: a review." *Dentomaxillofacial Radiology* 40.5 (2011): 265-273.
30. Shaw, Chris C., ed. *Cone beam computed tomography*. Taylor & Francis, 2014.
31. Raven, Carsten. "Numerical removal of ring artifacts in microtomography." *Review of scientific instruments* 69.8 (1998): 2978-2980.
32. Y. W. Chen, G. Duan, A. Fujita, K. Hirooka and Y. Ueno, "Ring artifacts reduction in cone-beam CT images based on independent component analysis," *2009 IEEE Instrumentation and Measurement Technology Conference*, Singapore, 2009, pp. 1734-1737. doi: 10.1109/IMTC.2009.5168737
33. Exxim Computing Corporation. Streak artifacts reduction. [En línea] 08 de 06 de 2017. http://www.exxim-cc.com/technology_sar.htm.
34. Davis, G. R., and J. C. Elliott. "Artefacts in X-ray microtomography of materials." *Materials science and technology* 22.9 (2006): 1011-1018.
35. Machin, K., and S. Webb. "Cone-beam X-ray microtomography of small specimens." *Physics in Medicine and Biology* 39.10 (1994): 1639.
36. Turbell, Henrik. *Cone-beam reconstruction using filtered backprojection*. Diss. Linköping University Electronic Press, 2001.
37. Yang, Kai, et al. "A geometric calibration method for cone beam CT systems." *Medical physics* 33.6 (2006): 1695-1706.
38. Chityala, R., et al. "Region of interest (ROI) computed tomography (CT): Comparison with full field of view (FFOV) and truncated CT for a human head phantom." *Proceedings of SPIE--the International Society for Optical Engineering*. Vol. 5745. No. 1. NIH Public Access, 2005.
39. Kim, Jae G., et al. "Inter-plane artifact suppression in tomosynthesis using 3D CT image data." *Biomedical engineering online* 10.1 (2011): 106.

40. <https://www.nde-ed.org/EducationResources/CommunityCollege/Radiography/TechCalibrations/definition.htm>
41. Krimmel, Sven. *Limited view angle tomography for single material objects in non-destructive testing with X-rays*. Diss. München, Technische Universität München, Diss., 2006, 2006.
42. Fahimian, Benjamin P., et al. "Low-dose x-ray phase-contrast and absorption CT using equally sloped tomography." *Physics in medicine and biology* 55.18 (2010): 5383.
43. Bronnikov, Andrei V. "Reconstruction formulas in phase-contrast tomography." *Optics Communications* 171.4 (1999): 239-244.
44. Mayo, S. C., et al. "X-ray phase-contrast microscopy and microtomography." *Optics Express* 11.19 (2003): 2289-2302.
45. J. Vlassenbroeck, Jelle, et al. "Software tools for quantification of X-ray microtomography at the UGCT." *Nuclear Instruments and Methods in Physics Research Section A: Accelerators, Spectrometers, Detectors and Associated Equipment* 580.1 (2007): 442-445.
46. Zhao, Wei, et al. "Investigation of the refractive index distribution in precision compression glass molding by use of 3D tomography." *Measurement Science and Technology* 20.5 (2009): 055109.
47. Abdullah, Jaafar, et al. "GammaScorpion: mobile gamma-ray tomography system for early detection of basal stem rot in oil palm plantations." *Optical Engineering* 52.3 (2013): 036502-036502.
48. Burvall, Anna, et al. "Phase retrieval in X-ray phase-contrast imaging suitable for tomography." *Optics express* 19.11 (2011): 10359-10376.
49. Introduction to X-TRACT. <http://www.ts-imaging.net/WebHelp/X-TRACT/Introduction%20to%20X-TRACT.html>. [En línea]
50. Guo, Yunfeng, Tiange Zhuang, and Jianqi Sun. "An improved phase retrieval algorithm for X-ray in-line phase-contrast imaging." *World Congress on Medical Physics and Biomedical Engineering May 26-31, 2012, Beijing, China*. Springer, Berlin, Heidelberg, 2013.

51. Chen, R. C., L. Rigon, and R. Longo. "Comparison of single distance phase retrieval algorithms by considering different object composition and the effect of statistical and structural noise." *Optics express* 21.6 (2013): 7384-7399.
52. Weitkamp, T., et al. "ANKAphase: software for single-distance phase retrieval from inline X-ray phase-contrast radiographs." *Journal of synchrotron radiation* 18.4 (2011): 617-629.
53. Mirone, Alessandro, et al. "The PyHST2 hybrid distributed code for high speed tomographic reconstruction with iterative reconstruction and a priori knowledge capabilities." *Nuclear Instruments and Methods in Physics Research Section B: Beam Interactions with Materials and Atoms* 324 (2014): 41-48.
54. Elliott, James C., et al. "Computed tomography Part II: The practical use of a single source and detector." *JOM* 46.3 (1994): 11-19
55. Ionita, Ciprian N., et al. "Cone-beam micro-CT system based on LabVIEW software." *Journal of digital imaging* 21.3 (2008): 296-305.
56. Flynn, Michael J., et al. "Microfocus x-ray sources for 3D microtomography." *Nuclear Instruments and Methods in Physics Research Section A: Accelerators, Spectrometers, Detectors and Associated Equipment* 353.1-3 (1994): 312-315.
57. Bernhardt, Ricardo, et al. "Comparison of microfocus-and synchrotron x-ray tomography for the analysis of osteointegration around Ti6Al4V implants." *European Cells and Materials* 7 (2004): 42-51.
58. Coates, Colin, B. Fowler, and Gerhard Holst. "sCMOS-Scientific CMOS technology: a high-per-formance imaging breakthrough." *White paper, Andor Technology, Fairchild Imaging and PCO AG*(2009): 171.
59. Dierick, Manuel, et al. "The use of 2D pixel detectors in micro-and nano-CT applications." *Nuclear Instruments and Methods in Physics Research Section A: Accelerators, Spectrometers, Detectors and Associated Equipment* 591.1 (2008): 255-259.
60. Kim, Jae G., et al. "Inter-plane artifact suppression in tomosynthesis using 3D CT image data." *Biomedical engineering online* 10.1 (2011): 106.
61. Tromba, G., et al. "The SYRMEP Beamline of Elettra: Clinical Mammography and Bio-medical Applications." *AIP Conference Proceedings*. Vol. 1266. No. 1. AIP, 2010.
62. Chen, R-C., et al. "PITRE: software for phase-sensitive X-ray image processing and tomography reconstruction." *Journal of synchrotron radiation* 19.5 (2012): 836-845.

63. <http://www.esrf.eu/UsersAndScience/Experiments/CBS/ID17>. [En línea]
64. Donzelli, Mattia, et al. "Conformal image-guided microbeam radiation therapy at the ESRF biomedical beamline ID17." *Medical physics* 43.6 (2016): 3157-3167.
65. http://photon-science.desy.de/research/studentsteaching/primers/synchrotron_radiation/index_eng.html.
66. <http://www.esrf.eu/UsersAndScience/Experiments/CRG/BM02/optic>.
67. Bacci, Alberto, et al. "Status of the STAR Project." *7th International Particle Accelerator Conference (IPAC'16), Busan, Korea, May 8-13, 2016*. JACOW, Geneva, Switzerland, 2016.
68. Bacci, A., et al. "The STAR Project." *Proc. of IPAC-2014, THPRO013*.
69. <http://www.ni.com/white-paper/3656/en/#toc1>. [En línea] 2016.
70. <https://www.physikinstrumente.com/en/products/rotation-stages/stages-with-worm-gear-drives/wt-90-goniometer-1206700/>.
71. <https://www.physikinstrumente.com/en/products/linear-stages-and-actuators/stages-with-motor-screw-drives/lr-270-linear-stage-1202700/>.
72. <https://www.physikinstrumente.com/en/products/linear-stages-and-actuators/stages-with-motor-screw-drives/lr-180-linear-stage-1202600/>.
73. https://www.digchip.com/datasheets/download_datasheet.php?id=5909955&part-number=C7942SK-05
74. https://www.hamamatsu.com/resources/pdf/etd/L12161-07_TXPR1023E.pdf
75. Wang, Shenghao, et al. *A LabVIEW based user-friendly nano-CT image alignment and 3D reconstruction platform*. No. arXiv: 1401.5197. 2014.
76. Mechanische Instrumente Optische System (Micos). *SMC_VIs*. July 28, 2005.
77. Instrumente Optische System (Micos). *SMC Hydra VI_Documentation*. 21 de 04 de 2009.
78. Mechanische Instrumente Optische System (Micos). *2 Axis – Controller System SMC Hydra CM*. 2015.
79. Hamamatsu. *150 kV MICROFOCUS X-RAY SOURCE L12161-07_Instruction Manual_Ver.2.0.1*. 25 de 11 de 2015.
80. <http://www.aps.anl.gov/epics/index.php>.

81. Diemoz, P. C., A. Bravin, and P. Coan. "Theoretical comparison of three X-ray phase-contrast imaging techniques: propagation-based imaging, analyzer-based imaging and grating interferometry." *Optics express* 20.3 (2012): 2789-2805.
82. <https://riverbankcomputing.com/software/pyqt/intro>.
83. http://wikiserv.esrf.fr/id17/index.php/Interface_software_for_CT_reconstructions.
84. Weitkamp, T., et al. "ANKAphase: software for single-distance phase retrieval from inline X-ray phase-contrast radiographs." *Journal of synchrotron radiation* 18.4 (2011): 617-629.
85. Mayo, S. C., et al. "X-ray phase-contrast microscopy and microtomography." *Optics Express* 11.19 (2003): 2289-2302.
86. A. Luu *et al.*, "SEB characterisation of commercial power MOSFETs with backside laser and heavy ions of different ranges," *2007 9th European Conference on Radiation and Its Effects on Components and Systems*, Deauville, 2007, pp. 1-7.
doi: 10.1109/RADECS.2007.5205543
87. F. Miller *et al.*, "Characterization of Single-Event Burnout in Power MOSFET Using Backside Laser Testing," in *IEEE Transactions on Nuclear Science*, vol. 53, no. 6, pp. 3145-3152, Dec. 2006. doi: 10.1109/TNS.2006.885376
88. Băjenescu, Titu I., and Marius I. Băzu. *Component reliability for electronic systems*. Artech House, 2010.
89. Galloway, Kenneth F. "A brief review of heavy-ion radiation degradation and failure of silicon UMOS power transistors." *Electronics* 3.4 (2014): 582-593.
90. K. Rashed, R. Wilkins, A. Akturk, R. C. Dwivedi and B. B. Gersey, "Terrestrial Neutron Induced Failure in Silicon Carbide Power MOSFETs," *2014 IEEE Radiation Effects Data Workshop (REDW)*, Paris, 2014, pp. 1-4. doi: 10.1109/REDW.2014.7004598
91. Scheick, Leif. *Testing guideline for single event gate rupture (SEGR) of power MOSFETs*. Pasadena, CA: Jet Propulsion Laboratory, National Aeronautics and Space Administration, 2008., 2008.
92. J. H. Hohl and G. H. Johnson, "Features of the triggering mechanism for single event burnout of power MOSFETs," in *IEEE Transactions on Nuclear Science*, vol. 36, no. 6, pp. 2260-2266, Dec 1989. doi: 10.1109/23.45433

93. M. Allenspach, J. R. Brews, I. Mouret, R. D. Schrimpf and K. F. Galloway, "Evaluation of SEGR threshold in power MOSFETs," in *IEEE Transactions on Nuclear Science*, vol. 41, no. 6, pp. 2160-2166, Dec. 1994. doi: 10.1109/23.340557
94. Kastner, Johann, and Christoph Heinzl. "X-ray Computed Tomography for Non-destructive Testing and Materials Characterization." *Integrated Imaging and Vision Techniques for Industrial Inspection*. Springer London, 2015. 227-250.
95. Liu, Zheng, et al. *Integrated Imaging and Vision Techniques for Industrial Inspection*. Springer, 2015.
96. Consentino, G., et al. "Dangerous effects induced on power MOSFETs by terrestrial neutrons: A theoretical study and an empirical approach based on accelerated experimental analysis." *AEIT Annual Conference, 2013*. IEEE, 2013.
97. Holt, David Basil, and David C. Joy, eds. *SEM microcharacterization of semiconductors*. Vol. 12. Academic Press, 2013.
98. Leonard, GW Chandler, S. Seraphin, in *Characterization of Materials*, 2nd ed., John Wiley & Sons, New York 2012, 1–16.
99. Pendleton, Tyler, Luke Hunter, and S. H. Lau. "Non invasive Failure Analysis of Passive Electronic Devices in Wireless Modules using X-ray Micro tomography (MicroCT)." *Thirty-fourth International Symposium for Testing and Failure Analysis*. ASM International, 2008.
100. G. Consentino *et al.*, "Dangerous effects induced on power MOSFETs by terrestrial neutrons: A theoretical study and an empirical approach based on accelerated experimental analysis," *AEIT Annual Conference 2013*, Mondello, 2013, pp. 1-6. doi: 10.1109/AEIT.2013.6666813
101. Brun, Francesco, et al. "Enhanced and flexible software tools for X-ray computed tomography at the Italian synchrotron radiation facility Elettra." *Fundamenta Informaticae* 141.2-3 (2015): 233-243.
102. Gureyev, Timur, et al. "Accuracy and precision of reconstruction of complex refractive index in near-field single-distance propagation-based phase-contrast tomography." *Journal of Applied Physics* 114.14 (2013): 144906.
103.
<http://www.oxfordscholarship.com/view/10.1093/acprof:oso/9780198567288.001.0001/acprof-9780198567288>.

104. https://www.mpimf-heidelberg.mpg.de/emeritusgruppen/biophysik/axial_tomography?employee_id=9276&seite=7.
105. Wu, Xizeng, Hong Liu, and Aimin Yan. "X-ray phase-attenuation duality and phase retrieval." *Optics letters* 30.4 (2005): 379-381.
106. Price, Ronald R., et al. "Quality assurance methods and phantoms for magnetic resonance imaging: report of AAPM nuclear magnetic resonance Task Group No. 1." *Medical physics* 17.2 (1990): 287-295.
107. King, Deirdre M., et al. "Development of a vessel-mimicking material for use in anatomically realistic Doppler flow phantoms." *Ultrasound in medicine & biology* 37.5 (2011): 813-826.
108. Smart Scientific Solutions. [En línea] 2016. http://smartscientificsolutions.com/wp-content/uploads/2016/03/Promotional_Leaflet_PlastiMouse-PlastiRat_2016_doublesided.pdf.
109. NDT Resource Center. [En línea] 27 de 01 de 2017. <https://www.nde-ed.org/EducationResources/CommunityCollege/Radiography/Physics/attenuationCoef.htm>.
110. National Institute of Standards and Technology. [En línea] 27 de 01 de 2017. <https://www.nist.gov/>.
111. Cullen, Dermott E., John H. Hubbell, and Lynn Kissel. "EPDL97: the evaluated photon data library, '97 version." *UCRL-50400* 6.5 (1997): 1-28.
112. Irvine, S., et al. "Simple merging technique for improving resolution in qualitative single image phase contrast tomography." *Optics express* 22.22 (2014): 27257-27269.
113. Mohammadi, Sara, et al. "Quantitative evaluation of a single-distance phase-retrieval method applied on in-line phase-contrast images of a mouse lung." *Journal of synchrotron radiation* 21.4 (2014): 784-789.
114. Gureyev, T. E., et al. "Linear algorithms for phase retrieval in the Fresnel region. 2. Partially coherent illumination." *Optics Communications* 259.2 (2006): 569-580.
115. Granton, Patrick Vincent. "SmART: dosimetry and applications." (2014).
116. <http://www.mouseimaging.ca/technologies/microct.html>. [En línea]
117. Tapfer, A., et al. "In-vivo dark-field and phase-contrast x-ray imaging." *Scientific Reports* 3.Nov 13 (2013).

118. <http://www1.udel.edu/ctcr/sites/udel.edu.ctcr/files/Amira%20Users%20Guide.pdf>
119. <https://sourceforge.net>.
120. Müller, Ralph. "Hierarchical microimaging of bone structure and function." *Nature Reviews Rheumatology* 5.7 (2009): 373-381.
121. Krenkel, Martin. "Cone-beam x-ray phase-contrast tomography for the observation of single cells in whole organs." (2015).
122. Turbell, Henrik. *Cone-beam reconstruction using filtered backprojection*. Diss. Linköping University Electronic Press, 2001.
123. Asl, Mahsa Noori, and Alireza Sadremomtaz. "Analytical image reconstruction methods in emission tomography." *Journal of Biomedical Science and Engineering* 6.01 (2013): 100.
124. Herzen, Julia, et al. "Quantitative phase-contrast tomography of a liquid phantom using a conventional x-ray tube source." *Optics express* 17.12 (2009): 10010-10018.
125. http://photon-science.desy.de/research/studentsteaching/primers/synchrotron_radiation/index_eng.html.
126. <http://www.esrf.eu/UsersAndScience/Experiments/Imaging/ID19/BeamlineDescription/GeneralDescription/Tips>.
127. <http://www.ni.com/white-paper/14144/en/>.
128. Barrett, Julia F., and Nicholas Keat. "Artifacts in CT: recognition and avoidance." *Radiographics* 24.6 (2004): 1679-1691.
129. <http://www.st.com/en/power-transistors/mdmesh-k5-series.html?sc=mdmeshk5&querycriteria=productId=SS1868>.
130. <http://www.st.com/en/power-transistors/stf20n95k5.html>
131. Wilkins, S. W., et al. "On the evolution and relative merits of hard X-ray phase-contrast imaging methods." *Phil. Trans. R. Soc. A372.2010* (2014): 20130021.
132. F. Darracq *et al.*, "Investigation of single event burnout sensitive depth in power MOSFETS," *2009 European Conference on Radiation and Its Effects on Components and Systems*, Bruges, 2009, pp. 106-111. doi: 10.1109/RADECS.2009.5994563